Laser spectroscopy of the antiprotonic helium atom –its energy levels and state lifetimes

反陽子ヘリウム原子のレーザー分光 ～エネルギー準位と準位寿命

Doctoral Dissertation

Department of Physics Graduate School of Science
University of Tokyo

2003

山口英斉
(Yamaguchi Hidetoshi)

December 10, 2003

Abstract

The antiprotonic atom is a three-body exotic system consisting of an antiproton, an electron and a helium nucleus. Its surprising longevity was found and has been studied for more than 10 years. In this work, transition energies and lifetimes of this exotic atom were systematically studied by using the antiproton beam of AD (Antiproton Decelerator) facility at CERN, with an RFQ antiproton decelerator, a narrow-bandwidth laser, Čerenkov counters with fast-response photomultiplier tubes, and cryogenic helium target systems.

Thirteen transition energies were determined with precisions of better than 200 ppb by a laser spectroscopy method, together with the elimination of the shift effect caused by collisions with surrounding atoms.

Fifteen lifetimes (decay rates) of short-lived states were determined from the time distributions of the antiproton-annihilation signals and the resonance widths of the atomic spectral lines. The relation between the magnitude of the decay rates and the transition multipolarity was investigated, and some states were found to have anomalously short lifetimes. The reasons were explained as state-mixing and collisional effects.

The experimental transition energies and lifetimes were compared with latest precise three-body variational calculations, and we succeeded in putting an upper limit (CPT limit) of 10 ppb on the proton-antiproton mass and charge differences.

Contents

Chapter 1

Introduction - Past Experiments, Theories

1.1 Introduction

The antiprotonic atom ($\overline{p}\mathrm{He}^+$) is a three-body exotic atom which consists of an electron, an antiproton and a helium nucleus. This thesis describes the experimental method and results of laser spectroscopy measurements for the energy levels and lifetimes of this exotic atom.

In this introductory chapter, the history of this atom is concisely reviewed (Sec. 1.2), and the energy structure and metastability of the atom are discussed (Sec. 1.3). Then, the principle of our laser spectroscopy method is presented (Sec. 1.4), followed by an explanation of the energy and lifetime measurements at LEAR (Sec. 1.5), with related topics such as the density shift effects (Sec. 1.5.1) and the hyperfine structure of the $\overline{p}\mathrm{He}^+$atom (Sec. 1.5.2). Finally, the latest theoretical calculations, to be compared with the experimental results, are reviewed (Sec. 1.6).

1.2 A Brief History of the Study of Antiprotonic Helium Atom

The history of exotic atom starts from the consideration of the negative muon captured in matter by Fermi and Teller [1]. A few years later, Wightman [2] calculated moderation processes of negative particles including antiprotons in hydrogen molecules. According to his and many subsequent calculations, negative hadrons should have picosecond-order or less lifetime in matter. Later on, a 10^{-10} second-

order lifetime for negative hadrons (pions) stopped in helium had been discussed by Condo [3] as the formation of pionic helium atoms, and the energy levels as well as the Auger decay rates of negative hadronic atoms had been calculated by Russell [4, 5].

In spite of the early predictions by the theorists, negative hadrons in matter had been believed for a long time to be immediately (within 1 ps) absorbed by nuclei. However, it was discovered that negative kaons [6, 7] and negative pions [8] stopped in liquid helium survive longer than 10 ns.

A similar experiment was performed also for antiproton, a negative hadron having infinite lifetime. In 1991, 3% of antiprotons stopped in liquid helium were found to have lifetime of as long as 3 microseconds at KEK [9]. This metastability was explained as the formation of antiprotonic helium atom, ($\overline{p}\mathrm{He}^+$) [10]. Soon after the discovery of the long-lived antiprotons, the stage of the experiment was moved to LEAR (Low Energy Antiproton Ring) at CERN in order to obtain pure and low-energy (21 MeV in kinetic energy, 200 MeV/c in momentum) antiprotons. In 1993, a laser spectroscopy experiment was started and a resonance was discovered successfully [11], and many transitions of the $\overline{p}\mathrm{He}^+$atom were found in the subsequent experiments [12–15]. Quenching effects by hydrogen and oxygen molecules were also studied. Such molecules can destroy the metastability of the $\overline{p}\mathrm{He}^+$atom drastically, which came upon an invention of a new method for resonance search [16, 17]. Three transitions were found by using helium target mixed with hydrogen. The hyperfine splitting of $\overline{p}\mathrm{He}^+$, which was caused by the coupling of the electron spin and the $\overline{p}$ orbital magnetic moment, was observed [18, 19]. OBELIX collaboration [20] also reported the observation of long-lived antiprotons in helium.

Theoretical calculation was improved in accordance with the experiments. Since early calculations of the transition wavelengths by Ohtsuki [21] and Shimamura [22] had about 1000 ppm accuracy, which was far wider than the laser linewidth, much effort was required for the first resonance search. In 1995, however, a very precise variational calculation was presented by Korobov [23] which enabled us to make much more efficient resonance searches. After applying the relativistic and QED correction, the agreement between three calculations (by Korobov [23], Kino [24] and Elander [25, 26]) and experiment were within the order of ppm.

In the end of 1996, LEAR was closed for a financial reason related to the LHC project. Fortunately, soon after that AD (Antiproton Decelerator) was decided to be built as an alternative antiproton facility. In 1998, ASACUSA (Atomic Spectroscopy And Collisions Using Slow Antiprotons) collaboration was formed and several experiments including high precision spectroscopy of antiprotonic helium atom were

proposed. The AD was started to run in 1999 for several days, and have been operated stably in the following years.

1.3 Metastability of the Antiprotonic Helium Atom

The metastability of the antiprotons in helium discovered in 1991 was later proved to be due to the formations of the $\overline{p}\mathrm{He}^+$atoms. Here we discuss the metastability of the atom in detail. When antiprotons are stopped in helium, most (97%) of them annihilate immediately (within 1 ps), while 3% of them survive as long as several microseconds. Fig. 1.1 is a time spectrum of antiproton annihilation in helium gas (DATS, Delayed Annihilation Time Spectrum). The long-lived component in

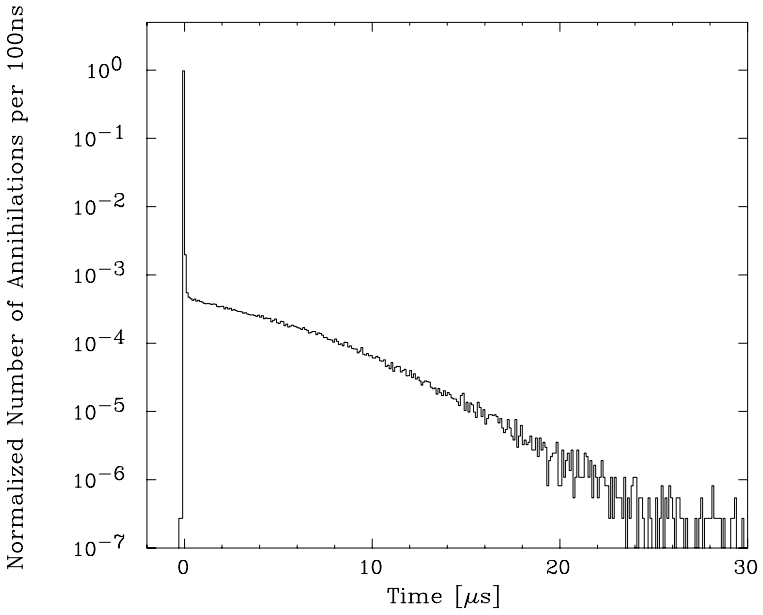

Figure 1.1: Annihilation time spectrum of antiprotons in helium gas of 4 K, 40 kPa. 3% of the total antiprotons have an average lifetime of 3–4 μs [27].

the spectrum is annihilations from the $\overline{p}^4\mathrm{He}^+$atom, of which energy levels are shown in Fig. 1.2. In this energy level diagram, n and l are the principal and angular momentum quantum numbers, respectively*[1]. As we are usually interested in the states where the electron is at the ground state, those quantum numbers represent the states of the antiproton. In the left of Fig. 1.2, two-body ion ($\overline{p}\mathrm{He}^{++}$) states are

[1]The states of this atom are denoted as (n, l).

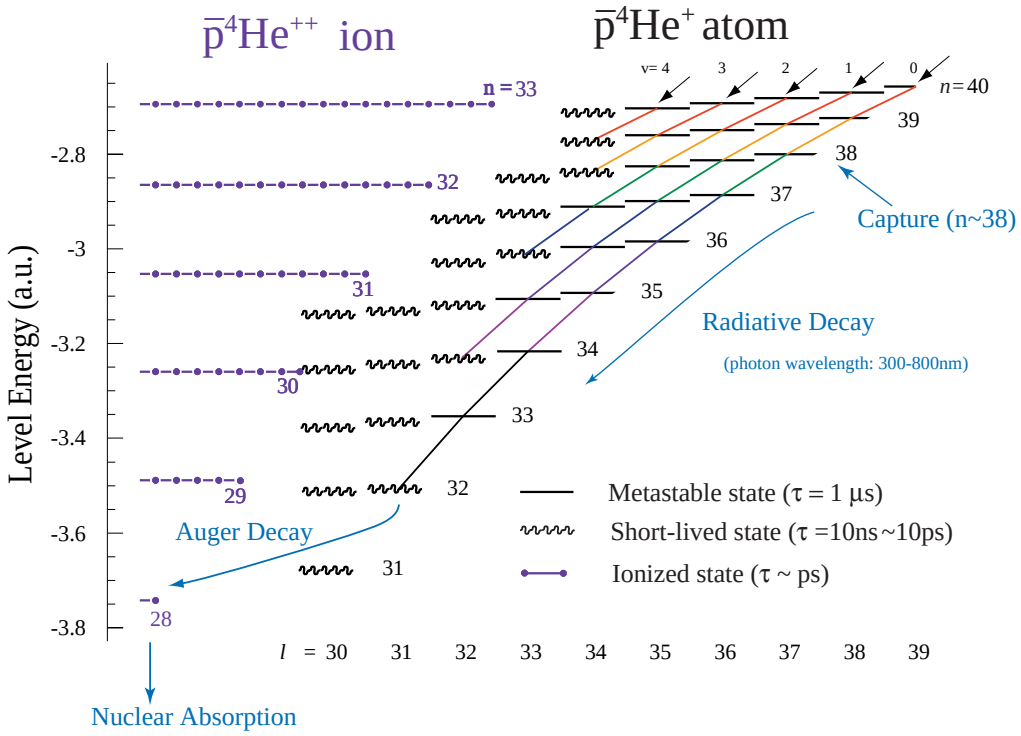

Figure 1.2: Energy diagram of the $\overline{p}$He^{+}atom and the $\overline{p}$He^{++}ion.

also shown.

Most of the antiprotons in the atomic states decay via two channels, which are, radiative and Auger decay (auto-ionization) channels. In Fig. 1.2, states shown with solid lines are called *metastable states*, in which most of the antiprotons de-excite radiatively. Their radiative lifetimes are typically 1–2 microseconds. States shown with wavy lines are called *short-lived states*, as they have shorter lifetimes due to their large Auger rates. An interesting feature of the Auger rate is a drastic dependence on the lowest possible transition multipolarity L, which is equal to the minimum angular momentum carried away by the Auger electron. Such a dependence was predicted from early calculations [4, 21]. Typically,

$$\gamma_A \sim 10^{17-3L}\ \mathrm{s}^{-1} \text{ for } L = 2, 3, 4. \tag{1.1}$$

As the radiative rates are $\sim 10^6\ \mathrm{s}^{-1}$ order, states with $L \leq 3$ are usually short-lived (Auger-dominated) states. In the states with $L > 3$, fast Auger decays are suppressed and the atom de-excites radiatively.

The quantum number $v = n - l - 1$, shown at the top of Fig. 1.2, corresponds to the number of nodes of the radial wavefunction. If we regard this atom as a molecule (molecular picture), v should be called as the vibrational quantum number. It is known experimentally and theoretically that v-changing radiative transition dipole moment is comparably small. Therefore, radiative de-excitations tend to occur so that v is conserved and make *cascade chains*. In this respect, transitions of $\Delta n = -1, \Delta l = 1$ type are called *favored transitions*, while another specific-type ($\Delta n = 1, \Delta l = -1$) transitions are called *unfavored transitions*. Typically the transition dipole moment μ_{if} is 0.2 - 0.4 debye for favored transitions, and 0.02 - 0.03 debye for unfavored ones. Fig. 1.3 shows theoretical radiative decay rates which can be evaluated by

$$\gamma_{rad} = \frac{4}{3}\frac{\omega^3 \mu_{if}^2}{\hbar c^3}, \tag{1.2}$$

where ω is the transition frequency.

Long-lived antiprotons are usually said to be captured at $n_{\mathrm{init}} \sim 38$ (for $\overline{p}^4\mathrm{He}^+$, or 37 for $\overline{p}^3\mathrm{He}^+$) states initially. This n_{init} corresponds to $\sqrt{M^*/m_e}$, where M^* is the reduced mass of antiproton in the atom and m_e is the electron mass*[2]. After successive radiative transitions along the $v =$ constant cascade chain, the antiproton

[2]The reduced mass in a three-body system depends on its definition. Since the electron has much smaller mass, here we take the reduced mass of antiproton as $\frac{1}{M^*} = \frac{1}{M_{\bar{p}}} + \frac{1}{M_\alpha}$, where $M_{\bar{p}}$ is the mass of antiproton, and M_α is the mass of helium nucleus. m_e should also be reduced mass, however, the difference from normal mass is negligible.

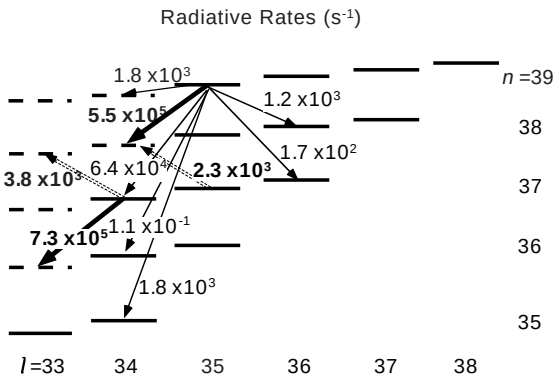

Figure 1.3: Radiative decay rates of some transitions. The favored transitions, which are shown as bold arrows, are dominant. The rates for unfavored transitions (dotted arrows) are shown for comparison with the other transitions, but real radiative transitions can happen only to the opposite direction.

reaches one of the short-lived states ('wavy' states shown in Fig. 1.2), where the antiproton can easily proceed to a two body state by ejecting the electron (*i.e.* Auger transition).

After the Auger transition, Stark mixing of the degenerate angular momentum levels of ionized $\overline{p}\mathrm{He}^{++}$immediately makes the wavefunctions of the antiproton and nucleus overlap. Then the antiproton is absorbed by the nucleus, and finally annihilates into pions.

1.4 Principle of the Laser Spectroscopy

The following method has been used for the measurement of the transitions such that the parent state is metastable and the daughter state is short-lived (e.g. the (39, 35)→(38, 34) transition having a wavelength of 597 nm).

The $\overline{p}\mathrm{He}^{+}$atoms are formed by stopping antiprotons in a helium gas target. The dipole transition between the states can be induced by a laser beam of correspondent wavelength. The antiprotons annihilate immediately after the laser-induced transition to the short-lived daughter state. As an antiproton annihilates into pions, the destructions of the $\overline{p}\mathrm{He}^{+}$atoms are observed by detecting pions. Fig. 1.4 shows annihilation time spectra for different laser wavelengths around a resonance center. The area of the peaks in the spectra is proportional to the number of antiproton annihilations induced by the laser shots.

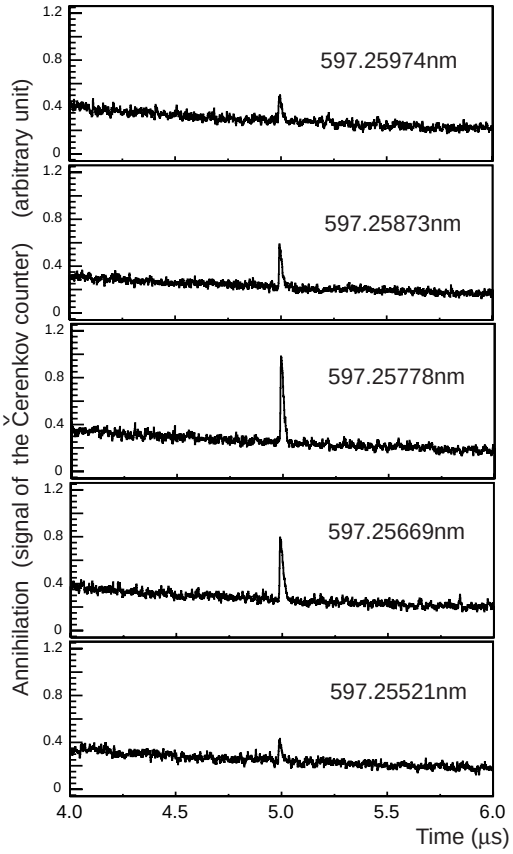

Figure 1.4: Annihilation time spectra of for different wavelengths. Measured at the AD.

A "resonance profile" can be drawn by taking the spectra for various laser wavelengths and plotting the peak area against the wavelength, as shown in Fig. 1.5. The central transition wavelength, which corresopnds to the level-energy difference of the two states, is determined by fitting this profile with a proper function.

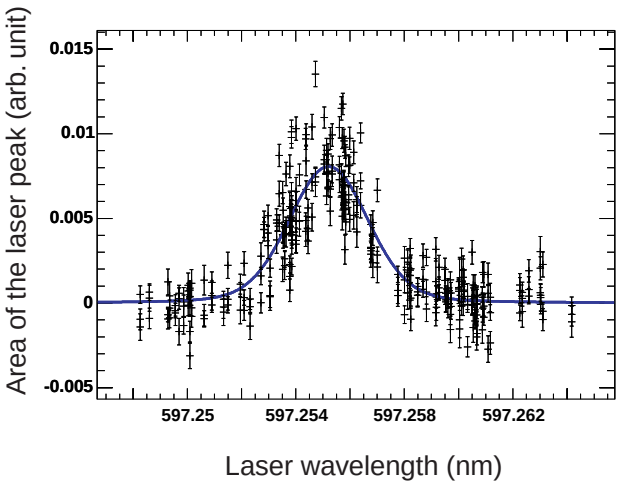

Figure 1.5: Resonance profile of the (39, 35)→(38, 34) transition. Measured at the AD.

The state lifetimes can be measured by many methods, depending on their magnitude. Two different methods used for the short-lived states are explained here. If the rate is fast enough, the resonance is observed as a far wider resonance than a typical one dominated by the laser linewidth (typically 1 GHz, same as the width of Fig. 1.5), due to its large natural width. The large natural width is given by

$$\Delta\nu_{\mathrm{nat}} = \gamma/2\pi, \tag{1.3}$$

conforming to the principle of uncertainty. On the contrary, if the decay rates are slow enough, the laser-induced annihilation spikes are prolonged to have long tails, reflecting the delay of the antiproton annihilations. Fig. 1.6 shows an example of a prolonged spike. For these cases, the lifetimes can be determined by evaluating the changes of the resonance width or the spike shape.

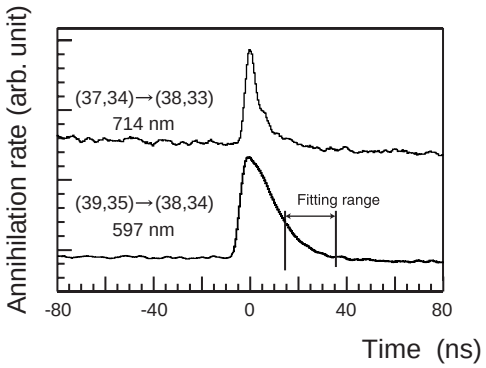

Figure 1.6: Prolonged laser resonance spike (lower) and not prolonged one (upper). Measured at the AD.

1.5 Energy Level and Lifetime Measurement in the Past Experiments

The laser spectroscopy method was actually carried out at LEAR, and produced many fruitful results. The results of the energy level and lifetime measurements are reviewed here.

1.5.1 Density Shift and High Precision Spectroscopy

In general, owing to collisions with surrounding atoms or molecules, the center of atomic resonance line is shifted and the linewidth is broadened as compared with those of an isolated atom. Such shift, called "density shift"*[3], is observed for the $\overline{p}\mathrm{He}^+$atoms as well. For example, the (39, 35)→(38, 34) of $\overline{p}^4\mathrm{He}^+$resonance profiles at three different target pressures are shown in Fig. 1.7. The central wavelength is shifted by 6 pm (corresponding to 4 GHz) in the spectrum of 103 kPa compared to that of 24 kPa. We need unshifted wavelength at zero-density limit for comparing it with the theoretical calculations of the transition wavelength in vacuum [28, 29].

The experimental result at LEAR shows that the shift in frequency is proportional to the density even when the pressure is as high as a few bars (atomic density $\rho \sim 10^{21}$–10^{22} cm^{-3}, see also App. A.2). This result suggests basically density shift can be explained by the semi-classical two-body impact theory (App. B). The density shift and the broadening for the $\overline{p}\mathrm{He}^+$atom is evaluated by Korenmann [30] and

[3]We use the term "density shift" as the density dependence of the frequency shift $\frac{\partial\omega}{\partial N}$, as well as shift itself.

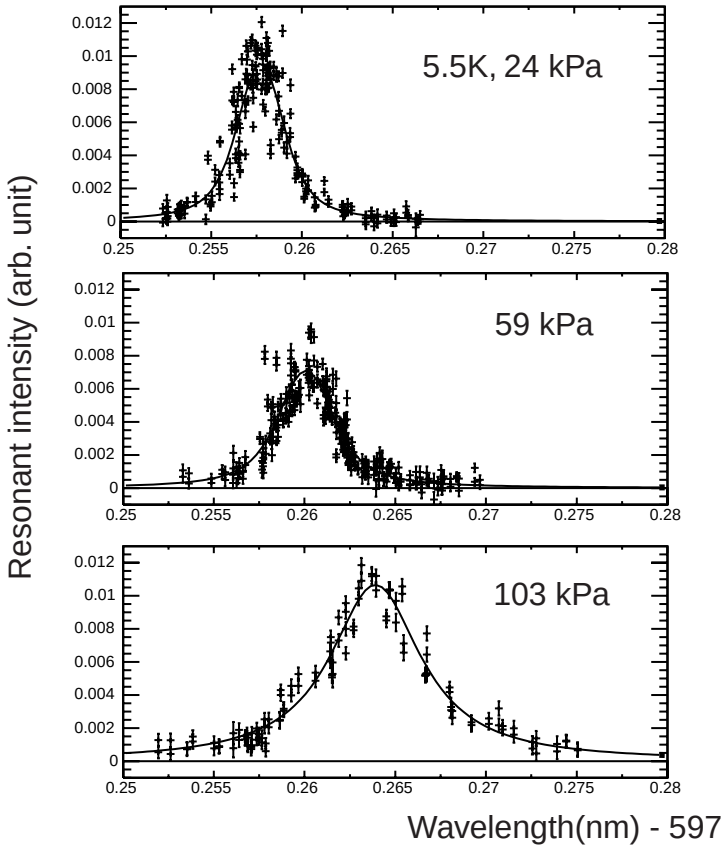

Figure 1.7: Resonance profiles of the (39, 35)→(38, 34) (597 nm) transition at three different target pressures. The target temperature was 5.5 K for all. Measured at the AD.

Bakalov [31], using the two-body impact theory. As long as the shift is proportional to the density, we can deduce the transition wavelength in vacuum by scanning resonances at several different (3 to 4) target densities and extrapolating the data linearly to zero density.

In previous experiment at LEAR, the density shifts of two transitions were measured [32]. The experimental shifts (Table 1.1) were in a good agreement with the calculation by Bakalov [31].

Transition	Wavelength (nm)	Density shift $\frac{\partial\omega}{\partial N}$ (10^{-21} GHz cm^3)	
		Experiment	Theory [31]
$\overline{p}^4$He$^+$(39, 35)→(38, 34)	597.2570±0.0003	-4.05 ± 0.07	-3.96
$\overline{p}^4$He$^+$(37, 34)→(36, 33)	470.7220±0.0006	-1.5 ± 0.1	-1.42

Table 1.1: Density shift and extrapolated central wavelength measured at LEAR [32]. The atomic density 10^{21} cm^{-3} corresponds to 6.65 g/l for helium gas (see A.2).

1.5.2 Hyperfine Splitting

The $\overline{p}$He$^+$atom has a hyperfine structure, which was observed in the laser spectroscopy experiment at LEAR [18]. The $\overline{p}^4$He$^+$atom has three angular momenta. They are the orbital angular momentum (mainly carried by the antiproton) $\boldsymbol{L}$, the electron spin $\boldsymbol{S}_e$, and the antiproton spin $\boldsymbol{S}_{\bar{p}}$*[4]. Here we define the HFS (hyperfine structure) as the structure comes from the coupling $\boldsymbol{L}\cdot\boldsymbol{S}_e$, and SHFS (superhyperfine structure) as the other couplings, namely, $\boldsymbol{L}\cdot\boldsymbol{S}_{\bar{p}}$, $\boldsymbol{S}_e\cdot\boldsymbol{S}_{\bar{p}}$ and spin-spin tensor coupling $2\{L(L+1)(\boldsymbol{S}_e\cdot\boldsymbol{S}_{\bar{p}})-3(\boldsymbol{L}\cdot\boldsymbol{S}_e)\cdot(\boldsymbol{L}\cdot\boldsymbol{S}_{\bar{p}})\}$.

With the laser spectroscopy experiment, the doublet structure due to the HFS was observed for some of the resonance line such as (37, 35)→(38, 34), which has a transition wavelength of 726 nm. The hyperfine splitting of this transition is 13 GHz for the parent state and 11 GHz for the daughter state, and the superhyperfine splittings are of the order of 100 MHz. The difference of the hyperfine splitting between the two states (1.8 GHz) appears as the doublet structure in the laser resonance profile (Fig. 1.8). Typically unfavored transitions have about 2 GHz of splitting, and favored transitions have smaller splittings of about 500 MHz or less. Evaluations of such considerably large splittings are important for measurements of the transition energies and lifetimes.

[4]The $\overline{p}^3$He$^+$has an additional angular momentum, the nuclear spin of ^{3}He^{++}.

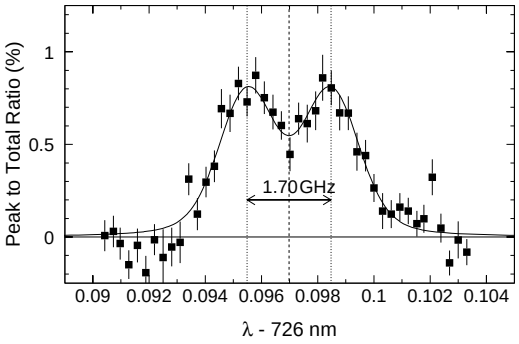

Figure 1.8: Resonance profile of the 726 nm transition [18].

1.5.3 CPT Test

In the experiments at LEAR, ten transitions of $\overline{p}^4\mathrm{He}^+$and three transitions of $\overline{p}^3\mathrm{He}^+$were observed. Among them, the transition wavelength of the (39, 35)→(38, 34) of $\overline{p}^4\mathrm{He}^+$(597 nm) was most precisely measured by taking the density shift effect into account. The wavelength was determined with a ppm-order precision, and the difference between the experimental results and calculations by Korobov [23], Kino [24] and Elander [25, 26] were within several ppm. Assured by the CPT theorem, a proton and an antiproton are usually expected to have exactly the same mass and charge. If the experimental and theoretical transition wavelengths are in a good agreement, we are able to make sure that there are no differences on the proton-antiproton mass and charge, since the precisely-known proton mass was substituted for the antiproton mass in the theoretical calculations (CPT test of antiproton, see Sec.4.4.1 for the detailed analysis procedure). From a comparison of the experimental wavelength with the theories, the antiproton-proton mass and charge ratios were determined with the following precision [32].

$$|\frac{M_{\bar{p}} - M_p}{M_{\bar{p}}}| = |\frac{Q_{\bar{p}} + Q_p}{Q_{\bar{p}}}| < 5 \times 10^{-7}. \tag{1.4}$$

1.5.4 Lifetime Measurement

The radiative lifetimes of two states, the (39, 35) and (37, 34) of $\overline{p}^4\mathrm{He}^+$, were studied at LEAR [33]. The experiment results shown in Fig. 1.9, were obtained by a method called "depletion-recovery method". The spectra shown in the top of Fig. 1.9 are the differences of the annihilation spectra with and without populational depletion by laser pulses. They illustrate the radiative annihilation spectra of the specific $\overline{p}\mathrm{He}^+$states, namely, the parent states of the laser transitions. The radiative rates of the parent states were determined by the time constant of these depletion-

recovery spectra. An interesting feature of this result is the density dependent

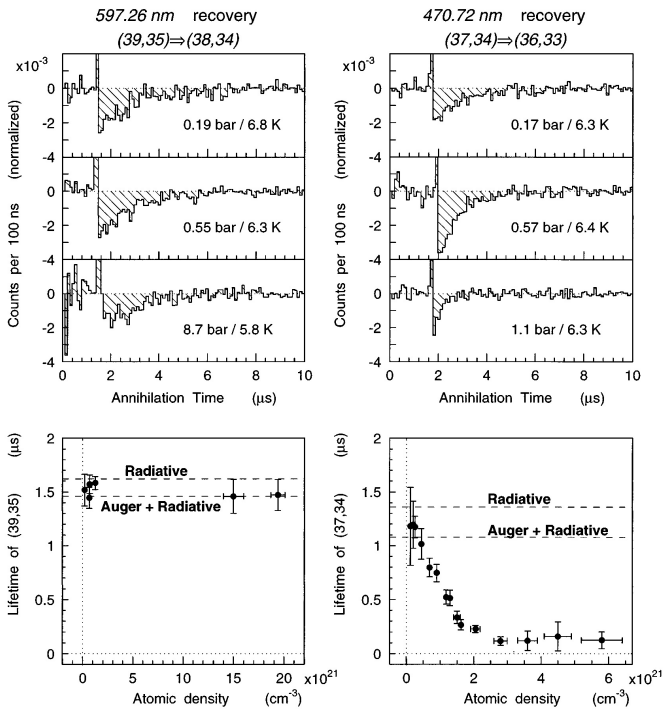

Figure 1.9: Depletion-recovery spectra (upper) and the lifetimes (lower) of the (39, 35) and (37, 34) of $\overline{p}^4\mathrm{He}^+$[33].

lifetime of the (37, 34) state. The (37, 34) state, which is metastable at a standard helium target condition (5–6 K, 20–30 kPa), changes into short-lived in a high-pressure helium gas. Such a density dependence is not observed in the (39, 35), as well as most of the other states.

The Auger lifetimes of two short-lived states, (38, 34) and (36, 33) of $\overline{p}^4\mathrm{He}^+$, were measured [33] at LEAR by analyzing the decay constants of the annihilation signals in the ADATS (Fig. 1.10). For these states, the decay rates are small enough to be observed in the time spectrum as the delay of annihilations.

A large natural width was observed for the unfavored transition (37, 34)→(38, 33) of $\overline{p}^4\mathrm{He}^+$at LEAR (Fig. 1.11), which indicates that the (38,33) state has a very large Auger rate of 10 ps-order.

1.6 Theoretical Three-body Calculation

As described in the previous section, The limit for the proton-antiproton mass and charge differences were determined by a comparison between the experimental

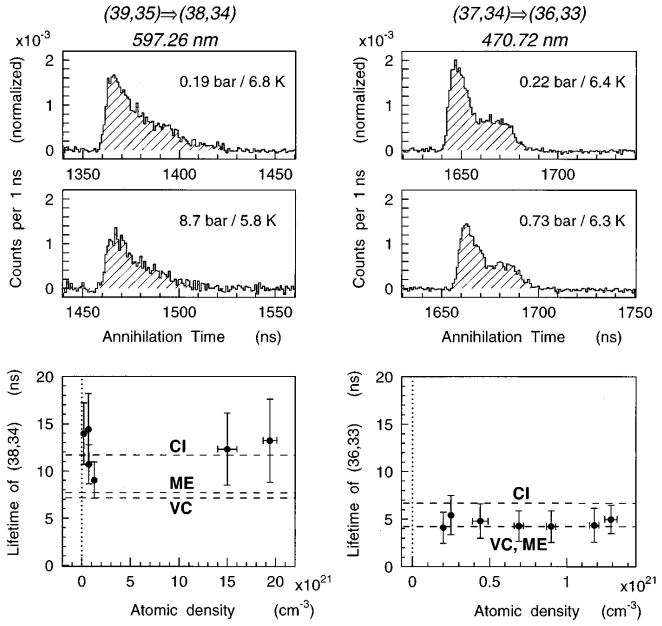

Figure 1.10: Annihilation signals of the laser-induced transitions, (39, 35)→(38, 34) and (37, 34)→(36, 33), at two different target densities for each (upper). Auger lifetimes of the daughter states were obtained from the above spectra, independent of the target density (lower) [33].

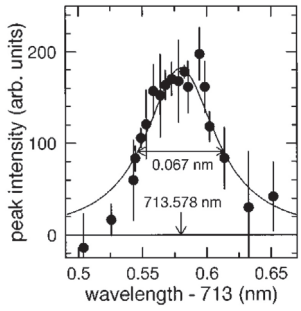

Figure 1.11: Resonance profile of (37, 34)→(38, 33) [34].

and theoretical values. These days the theoretical calculations were greatly improved from the LEAR period. An overview of latest precise calculation methods by Korobov [28] and Kino [29] are presented in this section.

Since the $\overline{p}\mathrm{He}^+$atom is a three-body Coulomb system, the relativistic equation for its atomic states cannot be solved directly, unlike the hydrogen-like system. In the calculations by Korobov or Kino, nonrelativistic (Shrödinger) equation was solved by a variational method at first, and then relativistic and QED corrections were applied.

1.6.1 Precise Coulomb Three-body Nonrelativistic Calculation

The non-relativistic Hamiltonian of $\overline{p}\mathrm{He}^+$in atomic units (Sec. A.1) is

$$\begin{aligned} H &= -\frac{1}{2\mu_1}\boldsymbol{\nabla}^2_{\boldsymbol{R}} - \frac{1}{2\mu_2}\boldsymbol{\nabla}^2_{\boldsymbol{r}} - \frac{1}{M_{He}}\boldsymbol{\nabla}_{\boldsymbol{R}}\boldsymbol{\nabla}_{\boldsymbol{r}} - \frac{2}{R} - \frac{2}{r} + -\frac{1}{|\boldsymbol{R}-\boldsymbol{r}|}, \\ \mu_1^{-1} &= M_{He}^{-1} + M_{\bar{p}}^{-1}, \\ \mu_2^{-1} &= M_{He}^{-1} + M_e^{-1}, \end{aligned} \tag{1.5}$$

where $\boldsymbol{R}$ and $\boldsymbol{r}$ are the position vectors of $\overline{p}$and electron, respectively.

The two calculations [28, 29] both start with this Hamiltonian and apply the variational method, but their basis functions are different.

Their wavefunctions are

$$\Psi^J_M(\boldsymbol{r},\boldsymbol{R}) = \sum_{l,L} r^l R^L [Y_l \otimes Y_L]_{JM} G^{JM}_{lL}(R,r,\theta), \tag{1.6}$$

where l is the angular momentum of the electron, L that of the antiproton, J and M the total angular momentum and its z-component. Korobov uses

$$G^J_{lL}(R,r,\theta) = \sum_{i=0}^{\infty} C_i \exp(-\alpha_i R - \beta_i r - \gamma_i |\boldsymbol{R}-\boldsymbol{r}|) \tag{1.7}$$

type function, where the complex coefficients α_i, β_i, and γ_i are generated in a quasirandum manner [35]. Kino's function is expanded by Gaussians:

$$G^J_{lL}(R,r) = \sum_{n,N} C_{n,N} \exp(-a_n r^2 - A_N R^2), \tag{1.8}$$

where a_n and A_N are given by the geometrical progression [36] method.

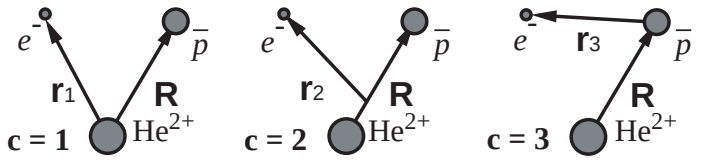

Figure 1.12: Three rearrangement channels used in [37].

Kino uses "coupled rearrangement channel method" to represent the dual (atomic and molecular) character of the atom. In his method, the wave functions are described by functions of three coordinate systems, called channels. The three channels are shown in Fig. 1.12. The channel c=1 is suitable for representing the atomic character of the system, where two particles orbit around the nucleus. The second channel c=2 is for the diatomic molecular character of the system, where the electron moves around two massive nuclei. The last channel c=3 is good for describing correlation of the electron and antiproton. The trial wavefunction is represented as a sum of three channels.

1.6.2 Relativistic Corrections

For the calculations of ppm-order precision, the relativistic corrections have to be taken into account.

The leading contribution is the relativistic (or binding) correction for the electron,

$$E_{rc} = \alpha^2 < -\frac{\boldsymbol{p_e}^4}{8m_e^3} + \frac{4\pi}{8m_e^2}[Z_{He}\delta(\boldsymbol{r}_{He}) + Z_{\bar{p}}\delta(\boldsymbol{r}_{\bar{p}})] > . \tag{1.9}$$

Another major contribution is the one-loop self energy,

$$\begin{aligned} E_{se} &= \frac{4\alpha^3}{3m_e^2}[\ln\frac{1}{\alpha^2} - \ln\frac{k_0}{R_\infty} + \frac{5}{6} - \frac{3}{8}] < [Z_{He}\delta(\boldsymbol{r}_{He}) + Z_{\bar{p}}\delta(\boldsymbol{r}_{\bar{p}})] > \\ &+ \frac{4\alpha^4}{3m_e^2}[3\pi(\frac{139}{128} - \frac{1}{2}\ln 2)] < [Z_{He}^2\delta(\boldsymbol{r}_{He}) + Z_{\bar{p}}^2\delta(\boldsymbol{r}_{\bar{p}})] > \\ &- \frac{4\alpha^5}{3m_e^2}[\frac{3}{4}] < [Z_{He}^3\ln^2(Z_{He}\alpha)^{-2}\delta(\boldsymbol{r}_{He}) + Z_{\bar{p}}^3\ln^2(Z_{\bar{p}}\alpha)^{-2}\delta(\boldsymbol{r}_{\bar{p}})] > . \end{aligned} \tag{1.10}$$

This is caused by the electron interacting with the electric field created by itself. In the above expression,$\ln(k_0/R_\infty)$ is the Bethe-logarithm [38] term, which arises from

Table 1.2: Contributions from different relativistic and QED corrections to the energy of the $(37, 34) \rightarrow (38, 33)$ transition [28].

Correction	Energy (GHz)	
E_{nr}	420 158 166	(20)
E_{rc}	-43 753	(30)
E_{rc-QED}	360	
E_{se}	5929	(5)
E_{vp}	-189	
E_{kin}	-4	
E_{ret}	-65	
E_{FSC}	4	
E_{total}	420 120 448	(40)

the low-energy photon contribution, and is one of the most difficult $\alpha^n(Z\alpha)^4$-order corrections to evaluate precisely.

Other minor contributions were also considered in the calculations by Korobov and Kino. They are, the relativistic correction to the kinetic energy for heavy particles E_{kin}, the one-loop vacuum polarization E_{vp}, the anomalous magnetic moment of the electron E_{rc-QED}, the retardation of the potential (transverse photon exchange) E_{ret}, and the nuclear finite-size correction E_{FSC}. See Ref. [28] for explicit formulations. Table 1.2 shows an example of the contributions from the various relativistic corrections, calculated by Korobov [28]

1.6.3 Complex Coordinate Rotation

The atomic states of the antiprotonic helium are not true bound states but should be regarded as resonant states, which eventually break up into subsystems after finite lifetimes.

A typical resonant state is *shape-type resonant state*. This type of resonance is found in radioactive nuclei, for example. In such a nucleus, an α particle can be temporary trapped by the potential well by tunneling phenomenon and eventually emitted, thus the system has a finite lifetime.

In another case, the potential can be spherical asymmetric. The r-coordinate is coupled to the angles and the bound state is pushed up into the continuum. This kind of state is called *Feshbach-type resonant state*, which can be explained semi-classically, while the shape-type resonant state is purely a quantum mechanical phenomenon. Some states of the antiprotonic helium atom should be treated as

Feshbach-type resonant states.

For precise calculations of such resonant states, we have to consider the complex Hamiltonian, of which the real part represents the level energy and the imaginary part is the lifetime. A good method to treat such resonant states correctly is complex-coordinate rotation [39, 40] method. Using this method, the coordinates are rotated in the complex plane by

$$(\boldsymbol{r}, \boldsymbol{R}) \rightarrow (\alpha \exp(i\theta)\boldsymbol{r}, \alpha \exp(i\theta)\boldsymbol{R}), \tag{1.11}$$

where α and θ are arbitrary parameters for the rotation. The equation of motion is solved by the variational method for the rotated Hamiltonian. The level energy and lifetime are obtained at the same time as the complex eigenenergy.

By choosing a proper set of parameters (α, θ), the energy and lifetime can be calculated precisely as a bound-state equation. Fig. 1.13 shows an example of CCR calculation for different parameter sets of (α, θ). For this case, the convergence point can be found at $\frac{\partial E}{\partial \theta}$ = minimum, almost independent of α.

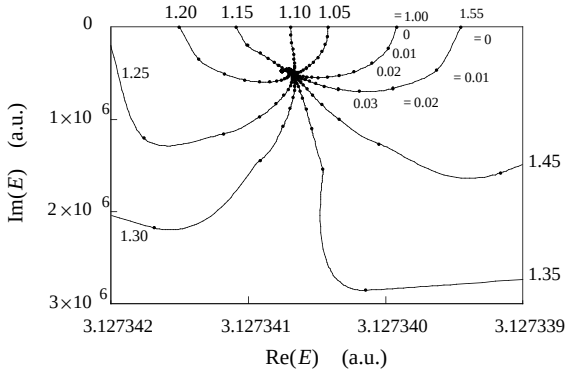

Figure 1.13: Calculations of the complex eigenenergy using various set of parameters [29]. The calculations with different α converges into a point in the complex plane.

Chapter 2

Purpose of the Experiment

The purpose of the experiment presented in this work is to measure two fundamental properties of the $\overline{p}\mathrm{He}^+$atom, the energy and lifetime (or equivalently, decay rate) of the states, precisely and systematically. Among the lifetime, the Auger lifetime was especially focused on.

We tried to measure the transition wavelengths as precise as possible for many $\overline{p}\mathrm{He}^+$transitions, with the considerations of the density shift effect, which can be eliminated by the extrapolation method described above, or by using a newly prepared low-density target.

High precision measurements at the AD were expected to have a huge difficulty. The previous high-precision spectroscopy at LEAR was done with continuous antiproton beam (10^4 antiprotons per second), while the AD can produce only pulse beams (5×10^7 antiprotons with a repetition time of 85 s). We had to use a method called "analog method" [41], which was regarded as unsuitable for high-precision measurements at LEAR, and the whole experimental setup was arranged to fit this method. Its components, narrow-bandwidth short-pulse lasers, fast-response photomultiplier tubes, a high-bandwidth digital oscilloscope, a RFQ decelerator, a low-density target system and so on, are described in the next chapter.

For the decay rates, the relationship of the rate and the transition multipolarity, usually known by the approximation formula Eq.(1.1), was studied as a main topic. Some decay rates can be larger than the approximated values. The reasons for such anomalous decay rates were investigated.

The obtained results can be compared with latest precise variational three-body calculations [28, 29]. The validity of the calculations were tested on both the energies and decay rates of the states, which are the real and imaginary parts of the complex energy. The agreement of the experiment and theories enables us to put a new limit (CPT limit, here defined as the maximum possible difference of an particle

and its antiparticle.) on the proton-antiproton mass and charge differences. By the experiment-theory comparison, a determination of the CPT limit far better than the result at LEAR (5×10^{-7}) was aimed.

Chapter 3

Experimental Method

3.1 Overview

Our experimental setup is schematically shown in Fig. 3.1. Antiprotons extracted

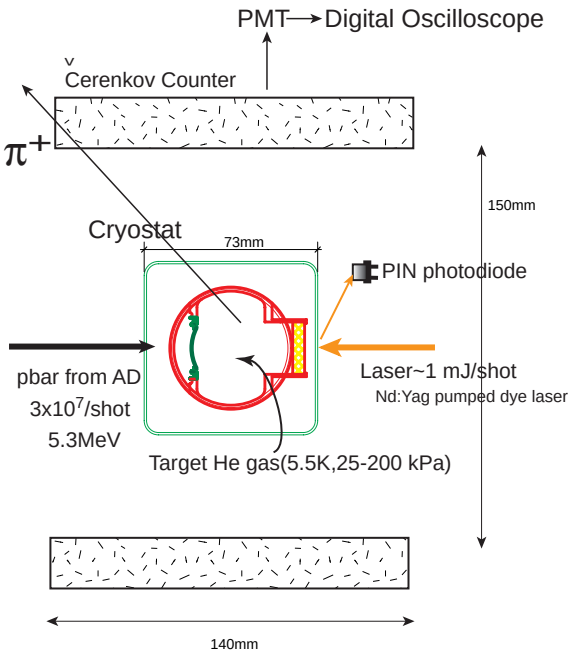

Figure 3.1: Experimental setup (at high density).

as a pulse beam from the AD were stopped in a helium gas target. After the $\overline{p}\mathrm{He}^+$atoms were formed, the target was irradiated by a laser beam coming from the opposite direction. The timing of the laser shot was recorded by a PIN photodiode. The target gas was cooled at 5.5–10 K by a cryogenic system. The annihilations

of antiprotons were detected by surrounding Čerenkov counters. In the following sections, each component of the experimental setup is described in detail.

3.2 AD

The AD (Antiproton Decelerator) is a facility which decelerates and cools antiprotons for providing low energy and pure antiproton beams. The previous antiproton-producing system used until 1996 consisted of an Antiproton Accumulator (AA), an Antiproton Collector (AC) and a storage ring (Low Energy Antiproton Ring; LEAR). Unlike the previous complex system of AA/AC/LEAR, the AD can produce antiprotons only as pulse-extracted beams, but is a much simpler and economical facility.

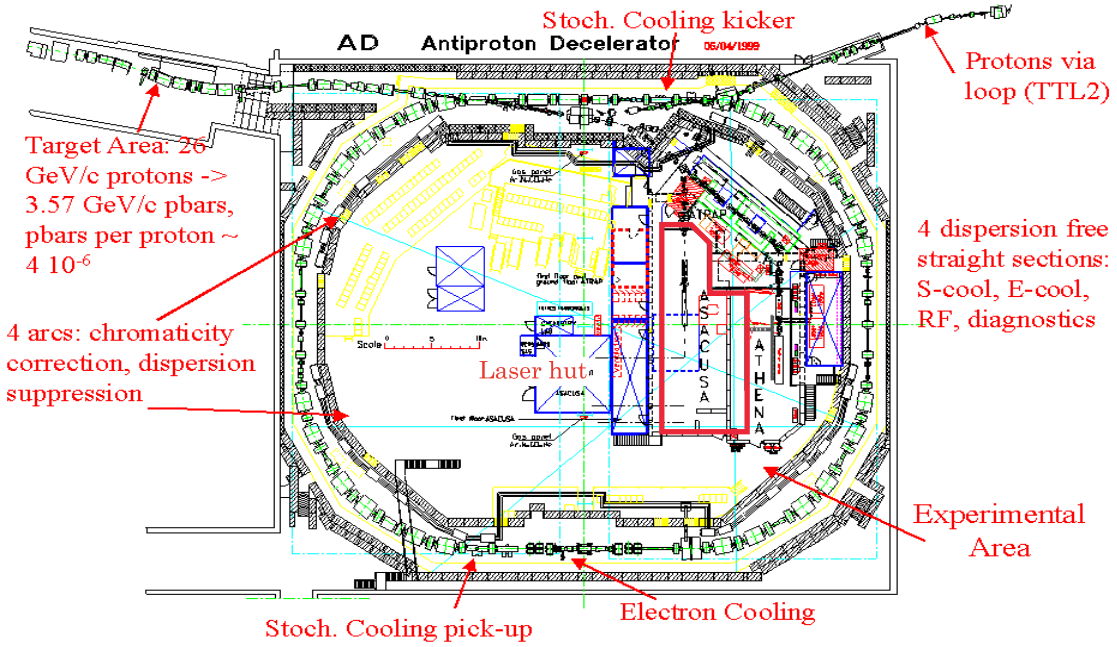

Figure 3.2: AD ring and beam transfer line to our experimental area (labelled as "ASACUSA"). Antiprotons produced at the target are transferred to the AD ring, cooled in the ring, then extracted to the experimental area. The laser beam is produced in the "laser hut" and transported to the area through a corridor.

The antiproton-production beam coming from CERN PS is 10^{13} protons at 26 GeV/c. About 5×10^7 antiprotons are produced at a platinum target and collected

at 3.57 GeV/c by a magnetic horn, then decelerated in the ring. After four stages of stochastic and electron coolings (Table. 3.1), antiprotons are cooled down to 100 MeV/c (kinetic energy = 5.3 MeV). The transverse emittance is 0.3 mm mrad and the momentum spread is 0.01% when the last electron cooling is finished. The 100–300 ns-wide antiproton pulses are extracted with a repetition time of 85 seconds. An extracted pulse consists of 3×10^7 antiprotons.

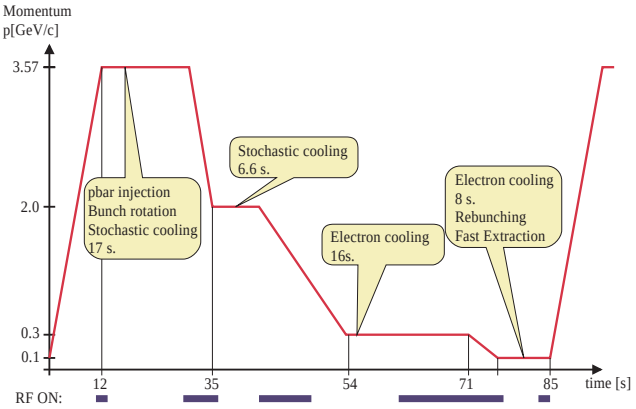

Figure 3.3: Deceleration and cooling cycle of the AD. One cycle is 85 s [42].

Momentum (GeV/c)	Cooling Process	transverse emittance (π mm mrad)	Δp/p (%)	Cooling time (s)
3.5	Stochastic	200 $\rightarrow$ 5	1.5 $\rightarrow$ 0.1	20
2.0	Stochastic	9 $\rightarrow$ 5	0.18 $\rightarrow$ 0.03	15
0.3	Electron	33 $\rightarrow$ 2	0.2 $\rightarrow$ 0.1	6
0.1	Electron	6 $\rightarrow$ 1	0.3 $\rightarrow$ 0.01	1

Table 3.1: Four stages of cooling.

3.3 RFQD

A major improvement in the last few years is that we started to use a new radio-frequency quadrupole decelerator (RFQD) [43]. The apparatus can decelerate antiprotons from 5.3 MeV to below 100 keV by an RFQ electric field. Decelerated antiprotons can be stopped at a low enough density target ($\rho = 10^{17}$–10^{18} cm^{-3}), for which the density shift effect is negligible. This kind of apparatus is widely used for

accelerating particles, but our RFQ beamline is used for deceleration, for the first time in the world.

Fig. 3.4 shows the side view of the RFQD. The incoming antiprotons of 5.3 MeV are bunched by a coaxial TEM double-gap resonator. A corrector cavity to preserve the energy acceptance is also installed upstream of a rf tank. Inside the rf tank, there are 34 "rf cells", each of which consists of four-rod type electrodes are placed, and an rf voltage (202.5 MHz, 167 kV) is applied to them. The whole rf system can be biased ± 60kV so that the kinetic energy of the beam is variable between 10 keV and 120 keV. The beam profile was monitored by a scintilator screen (upstream of the rf tank) and secondary emission wire chambers (downstream) for the tuning.

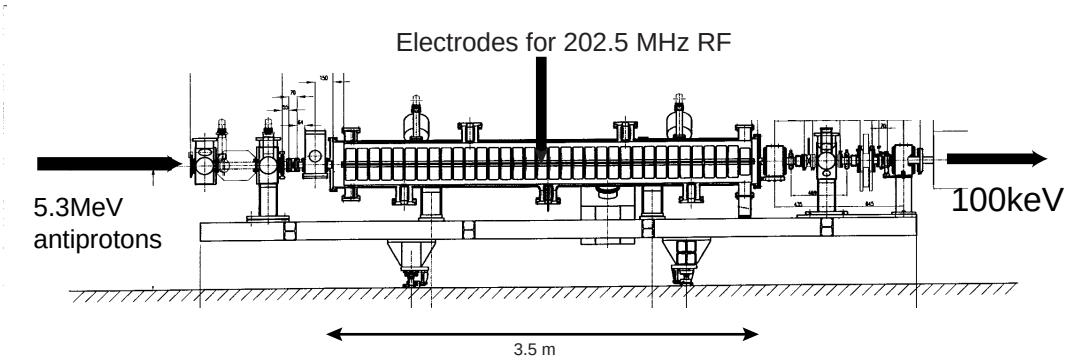

Figure 3.4: Side view of the RFQD [44].

Since the deceleration efficiency (the ratio of the decelerated particles to the total) of the RFQD is about 30%, a bending line is installed in the downstream of the RFQD in order to avoid undecelerated (5.3 MeV) antiprotons coming into the target (Fig. 3.5). After focusing by two solenoids, only decelerated antiprotons are transferred to the target by dipole and quadrupole magnets. With this bending line, the undecelerated antiprotons were totally prevented from entering the target, and the unnecessary annihilation signals decreased very much.

Due to the deceleration efficiency, RF noise arising from the RFQD, and the large stopping distribution of the antiprotons, the laser peak observed at the low-density measurement is not as sharp as the high-density measurement. The high-density measurement is suitable for measurements in which low intensity signals are expected, such as scans of unfavored transitions having small dipole moments.

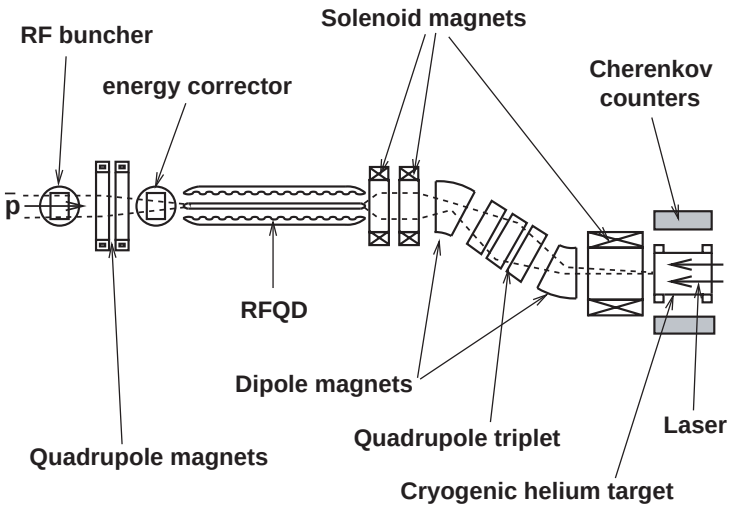

Figure 3.5: Bending line for the slow antiprotons [45].

3.4 Cryogenic System

In our experiment, the $\overline{p}$He$^+$atoms are formed in a helium gas target cooled down to 5.5–10 K. One reason why we needed such low temperature gas is to exclude impurity gases such as hydrogen, oxygen and nitrogen. These gases interact with antiprotonic helium atoms strongly and quench even if their concentration is only a few ppm [10, 46–48]. Another reason is to reduce the resonance width. High temperature increases the Doppler broadening, which is proportional to square-root of the temperature. The collisional broadening is also considerably large when the temperature is high. On the other hand, too low temperature causes another problem. Below the critical temperature of 5.2 K, the gas density varies drastically with a slight change of the pressure (see Fig.3.6). This produces a large uncertainty of the density. With the above considerations, we kept the target temperature at 5.5–10 K.

We used two different cryogenic system according to the antiproton beam energy. The two conditions (whether the RFQD is used or not) are summarized in Table 3.2.

Fig. 3.7 is the vertical cross section of the high-density cryostat. The target is isolated in 10^{-6} Torr vacuum, and its temperature is kept cool with the supply of liquid nitrogen and helium. The window for the antiproton beam is 25 μm thick,

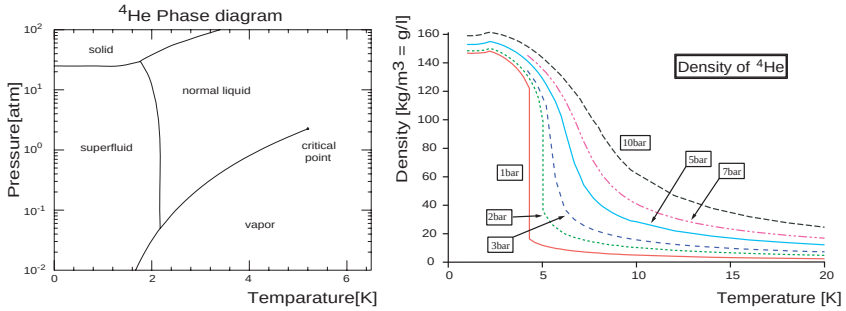

Figure 3.6: Phase diagram (left) and density-temperature plot of ^{4}He (right).

Table 3.2: Two target conditions of the experiment.

	High density	Low density
Kinetic energy of $\overline{p}$	5.3 MeV	80-100 keV
Gas density	1×10^{20}–5×10^{21} cm^{-3}	10^{17}–10^{18} cm^{-3}
Temperature	5.5–6 K	9–10 K
Pressure	20–200 kPa	0.01–0.3 kPa
Size of the stopping distribution	a few cm	$>$ 10 cm

and made of stainless steel. Another window is made of quartz for the laser beam coming in. The cryostat for the low-density target is shown in Fig. 3.7. It has a much larger geometry than the high-density cryostat, because of the large stopping volume of the low-energy antiprotons. We can arbitrary set the gas density using the gas system shown in Fig. 3.9.

The pressure and temperature of the target helium gas were measured and recorded every 30–50 seconds. The temperature was measured with thermocouples placed inside the cryostat, and stabilized at 5.5–6 K (high density) $\sim$ 10 K (low density) by a PID-controlled heater. The pressure is measured with MKS Baratron gauges, which determines pressure by measuring the change in capacitance between a diaphragm (movable plate) and an electrode. The temperature was stabilized within 0.1 K, and and the precision of the pressure measurement was 0.1–1 kPa for the high density target, 0.1–1 Pa for the low density target.

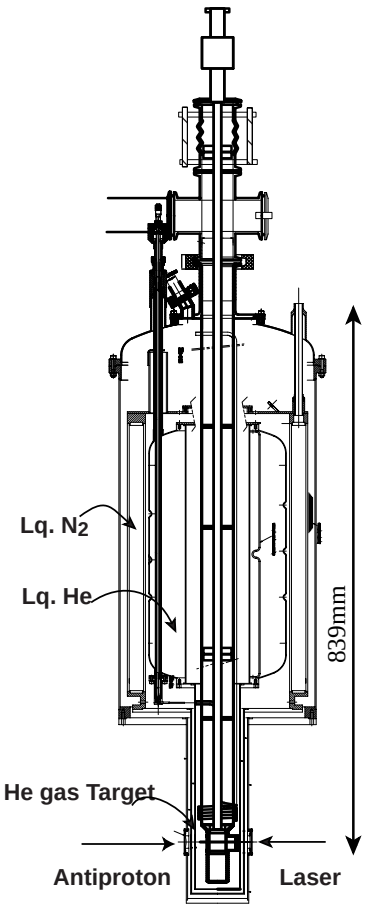

Figure 3.7: Small cryostat for the high-density measurement. Target He gas is filled thorough a long tube at the center of the cryostat. Liquid N_2 and He layers are surrounding the tube to keep the target cool.

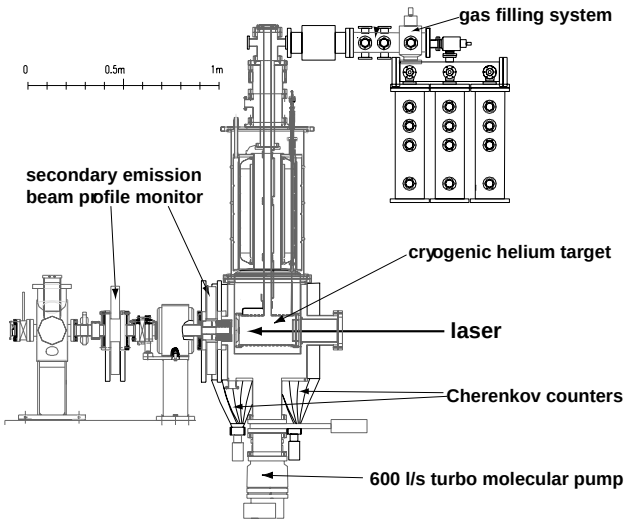

Figure 3.8: Large cryostat for the low-density measurement. The arrangement of detectors (beam profile monitors, Čerenkov counters) are also shown.

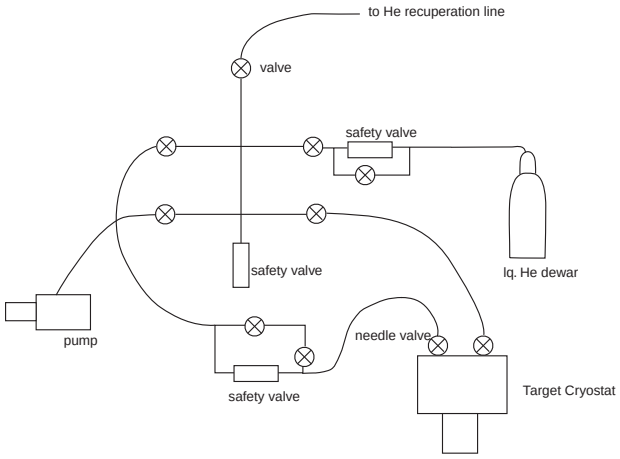

Figure 3.9: Diagram of the gas system for the high-density cryostat. We can inject He gas from the dewar, or evacuate the target by the pump. Safety valves are installed to avoid overpressurizing. A similar system is used for the low-density cryostat.

3.5 Detection System

In this section, our detection system for the antiprotons are explained. The spatial profiles of the beam was monitored by secondary electron emission detectors, and the time profile, by a Čerenkov counter. Two Čerenkov counters were placed beside the cryostat to measure time spectra of antiproton annihilations.

3.5.1 Beam Profile Monitor - Secondary Electron Emission Detector

The horizontal and vertical profiles of the antiproton beam are measured by secondary electron emission detectors. The detector is very thin (5 μm-thick polyester in total) so that we can measure the beam non-destructively. It consists of an anode foil and two position-sensitive cathode foils. The anode foil is made by depositing 20 nm-thick layers of gold on a polyester foil. Two cathode foils for the X and Y projection of the beam are placed both side of the anode foil, and are position sensitive by making a structure of 20 segmented strips on the surface. The electrodes are 50 nm-thick layers of alminium. When antiprotons hit the strip electrode, secondary electrons are emitted toward the anode foil, which is biased at a voltage of 50–100 V. The electric charges were measured by ADC using charge-sensitive preamplifiers connected to the electrodes one by one. Since a strip is about 1 mm wide, we can obtain beam profiles in the 20 mm x 20 mm area with 1 mm precision. A photograph of the detector and a measured profile is shown in Fig. 3.10 and Fig. 3.11, respectively.

3.5.2 Cherenkov Counters

An antiproton annihilates into 3–7 pions. In our experiment, charged pions produced by the annihilations of antiprotons are detected by three Čerenkov counters. Two of them are placed beside the target, covering 40% - 50% of the total solid angle. The other one is laid more than 1 m away from the target in order to detect only the prompt peak, which is produced by immediate annihilations of most ($\sim$97%) of the antiprotons. The radiators are UV-transparent Lucite. They have 30 cm $\times$ 14 cm area and 90 cm $\times$ 40 cm, for the high-density and low-density measurement, respectively. Their thickness is 1–2 cm. Due to the large stopping volume of antiprotons, the geometry of the radiators used for the low-density target is much larger.

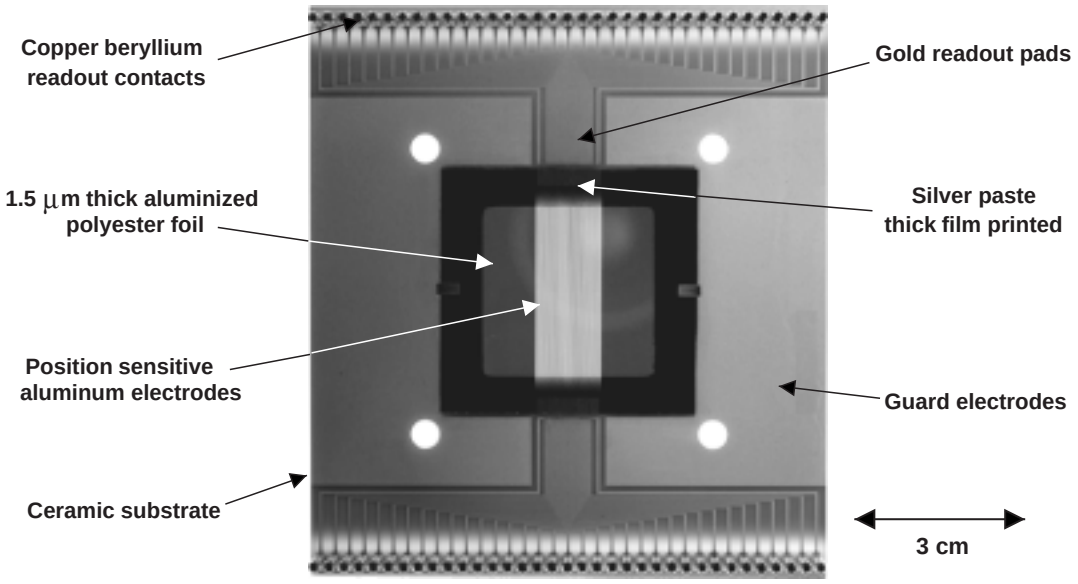

Figure 3.10: Photograph of the secondary electron emission detector.

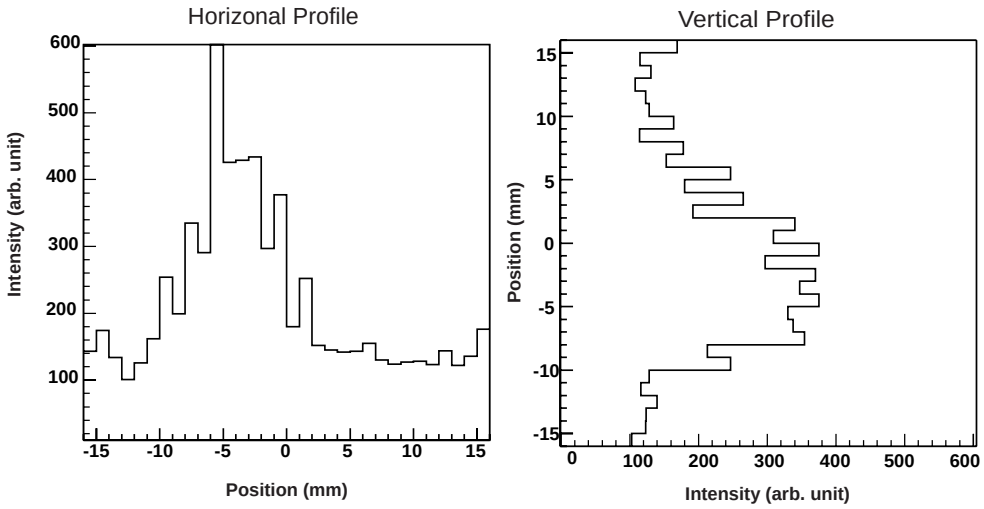

Figure 3.11: Two-dimensional profiles of an antiproton beam measured by the secondary electron emission detector.

Since the pions decay into muons and then into electrons*[1], a lot of positrons which originates from positive pions stopped in surrounding material are also detected. Muon has a lifetime of 2.2 μs, which is the same order as that of antiprotonic helium atom ($\sim$3 μs). This means that the signals of π^+-μ^+-e^+ cannot be distinguished from those of pions created from the decays of antiprotonic helium atoms, and remain as background signals.

The Čerenkov light is detected by gatable fine-mesh photomultiplier tubes (PMT) developed for this experiment (Hamamatsu Photonics R5505GX-ASSYII). It has 15 fine-mesh dynodes The rise and fall time are 1.6 ns and 4.3 ns, respectively. The photocathode is bialkali and has a 17.5 mm of diameter. Compared to a typical PMT, this tube is high-speed, less affected by magnetic field and has a good linearity.

The amplified analog signals from the PMT are directly fed to a digital oscilloscope with a bandwidth of 1 GHz. This method is called *analog method*, in contrast with the event-by-event detection system [49] used at LEAR, so a time spectrum obtained with this method is called ADATS (Analog Delayed Annihilation Time Spectrum). The event-by-event detection system was able to detect single annihilation of an antiproton, but it was not capable of detecting a large number of antiprotons arriving in high rate ($> 10^4$/s). Another restriction was that the laser can be fired only $\sim$1 μs after the arrival of the antiprotons, because of the complexity of the event detection. The analog method is suitable for AD, where we can extract antiprotons only as pulse beams.

The gatability of the PMT is required for detecting only the delayed part of the annihilation time spectrum. The prompt peak is huge compared to the delayed part, which consists of only 3% of extracted antiprotons (and muons). As the dynamic range of the PMT and the resolution of the digital oscilloscope are limited, we had to eliminate the unnecessary prompt peak. Unless we exclude the prompt peak, we have saturated signal delayed time spectra are distorted by after pulses, otherwise we can use only small part of the full dynamic range. Synchronized with the trigger from the AD, the PMT is activated by a gating circuit when the prompt annihilations are over. The PMT for the prompt peak is ungated to record the shape of the prompt annihilation.

The upper spectrum in Fig. 3.13 is an ADATS obtained by one of the Čerenkov counters near the target. The two peaks in the spectrum correspond to annihilations induced by successive two laser shots. The lower spectrum in Fig. 3.13 is obtained by the distant Čerenkov counter, which was not gated. The large peak in this spectrum represents a huge amount of prompt annihilations of about 97% of total antiprotons

[1] This is called "π-μ-e decay" chain.

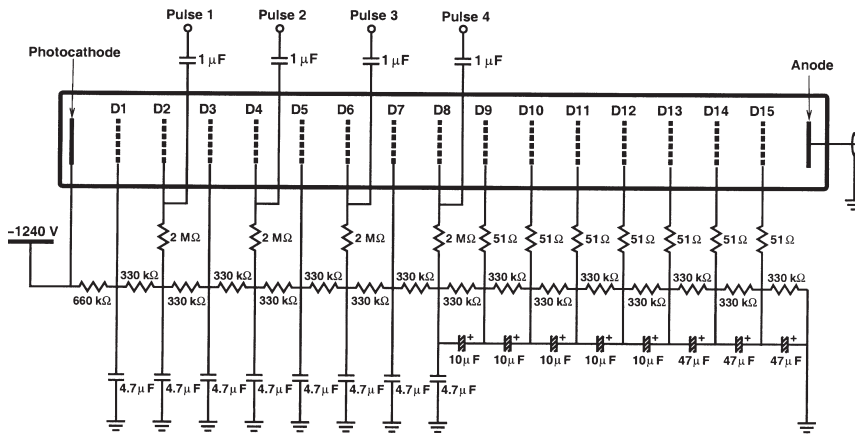

Figure 3.12: Gatable fine-mesh PMT R5505GX-ASSYII and its voltage divider circuit. The electron multiplification can be gated off by reversing the potentials of dynodes D2, D4, D6 and D8 [50].

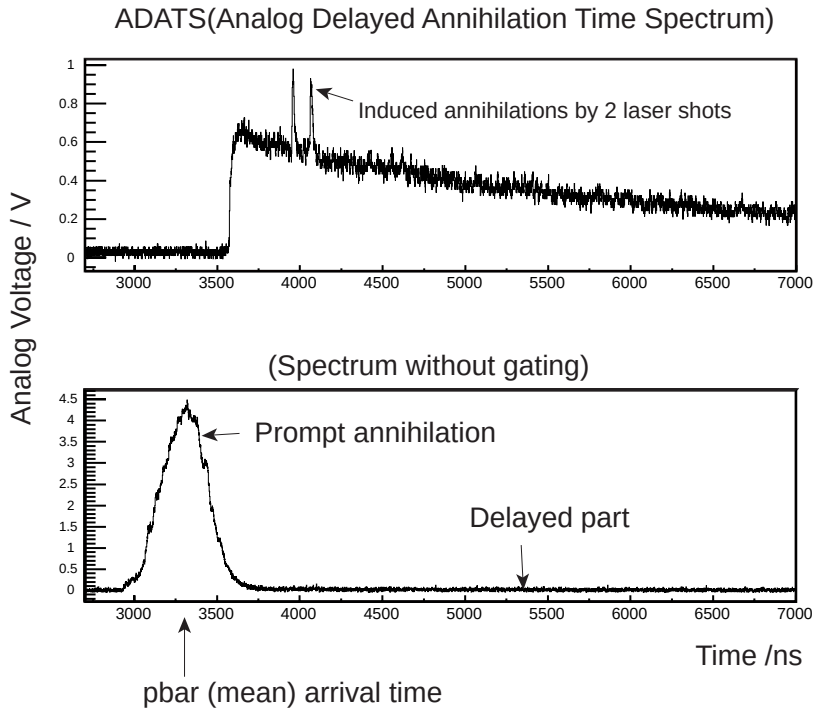

Figure 3.13: ADATS and prompt annihilation

in a pulse. The time profile of the prompt annihilation peak is a Gaussian-like shape with the width of 100–300 ns.

3.6 Laser System

3.6.1 Laser System

Fig. 3.14 is a schematic diagram of our laser system. Since most of the transitions

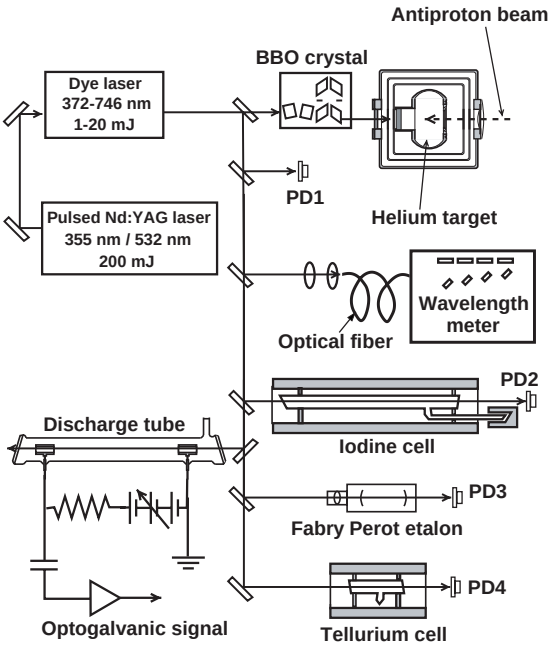

Figure 3.14: Schematic diagram of the laser system. PD 1–4 are PIN photodiodes [51].

of our interest have wavelengths of visible or ultraviolet light, a dye laser system is a good solution to make such transitions over a wide range of wavelengths. Our dye laser (Lambda-Physik Inc. Scanmate 2E) can produce from infrared to ultraviolet wavelengths (320–860 nm) with a narrow bandwidth of 600 MHz. Its shot-to-shot power fluctuation is 5% in best cases. Synchronized with the trigger from AD, the laser can be fired anytime after the arrival of antiprotons. To obtain ultraviolet (280–420 nm) laser beams, a BBO-type III crystal can be used for the frequency-

doubling. The dye laser is pumped by a pulsed Nd:Yag laser (Coherent Infinity), which has wavelengths of 533 or 355 nm, and power of 200 mJ/pulse.

The laser power required for our experiment can be evaluated as the following. Rabi frequency Ω is given by [52]

$$\Omega = \mu E_0 \hbar, \tag{3.1}$$

where μ is transition dipole moment and E_0 is amplitude of the electric field by the laser. The power density which gives $\Omega t = 2\pi$ is

$$\begin{aligned} P &= 1.5 \text{ MW/cm}^2 \text{ for } \mu = 0.3 \text{ debye (favored transitions)} && (3.2)\\ &= 150 \text{ MW/cm}^2 \text{ for } \mu = 0.03 \text{ debye (unfavored transitions).} && (3.3)\\ & && (3.4) \end{aligned}$$

In order to make favored and unfavored transitions, the power density should be comparable to these power densities, respectively. For favored transitions, the energy density of the laser at the target position was 0.1 - 1.0 mJ/cm^2. As the pulse length of the laser is 5 ns, it produces power density of 0.2 - 2 MW/cm^2, which is sufficient for making transitions. For unfavored transitions, laser beams with 1–2 order of magnitude higher power density were applied.

The dye laser used in our laser system can be operated in two modes. The laser in the "broadband" mode can be high power (a few 10 mJ/shot) but the linewidth is several GHz. Another is the "high-resolution" mode, which puts severe constraint on the laser frequency by an intracavity etalon to have a narrow linewidth of 600 MHz. For some unfavored transitions, the laser was operated in the broadband mode to fulfill the requirement of high power. The laser beam was transported from the laser hut to the experimental area (see Fig. 3.2) for several 10 meters by ~ 5 mirrors and a pair of lenses.

The timing of laser shot is recorded by a 1 GHz-bandwidth PIN photodiode placed near the target cryostat. Fig. 3.15 shows an ADATS and a spectrum of PIN photodiode signal. The PIN photodiode (in Fig. 3.1) picks up the reflection light of the laser, and produces a sharp signal with a good linearity and low noise. By referring to the photodiode signal, the timing of laser peak position is determined with a precision of few nanoseconds.

The wavelength is measured by a wavemeter (ATOS LM-007), which has four interferometers. Each interferometer covers approximately two orders of magnitude of the laser frequency below its own free spectral range (Table. 3.3), thus eight-digit precise wavelength can be measured. The highest-precision interferometer has a

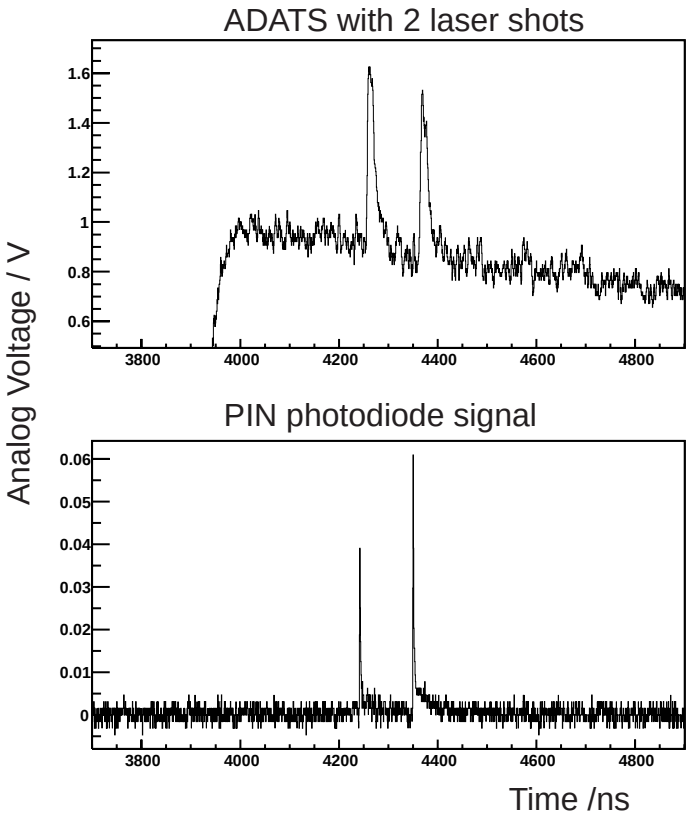

Figure 3.15: ADATS and PIN photodiode signal

interferometer #	Base length	Free Spectral Range
1	3 μm	1000 cm^{-1}, 30 PHz
2	50 μm	50 cm^{-1}, 1.5 PHz
3	1.5 mm	2.7 cm^{-1}, 81 GHz
4	40 mm	0.127 cm^{-1}, 3.8 GHz

Table 3.3: Base lengths and free spectral ranges (in cm^{-1}) of the four interferometers in the wavemeter.

base length of 40 mm, and its resolution is 0.6 GHz. Therefore, the wavemeter has a (relative) precision of 0.5 - 1 pm for the wavelengths of visible light.

Fig. 3.16 shows spectra of the four interferometers by a typical laser shot. The distance between fringes (peaks) corresponds to the free spectral range. The positions of the fringes are determined by a computer analysis, then converted to a wavelength. Since the absolute precision of the wavemeter is not as precise as 0.6

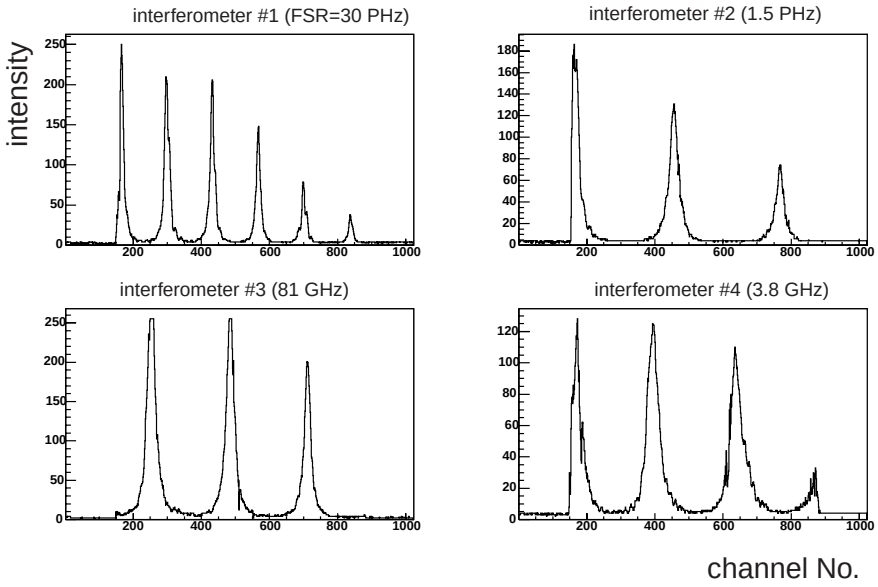

Figure 3.16: Spectra of the four interferometers, each of which determines approximately two digits of the wavelength.

GHz, we performed calibration measurements, described in the next subsection.

3.6.2 Absolute Wavelength Calibration

To improve the absolute precision of the laser wavelength, our wavelength meter is absolutely calibrated against molecular ro-vibrational lines of iodine or tellurium, or atomic lines of neon or argon by optogalvanic spectroscopy.

Ro-vibrational lines of iodine molecule are widely used for optical calibration measurements in the wavelength range of 500–900 nm. We performed the following measurement in the intervals of the antiproton pulses for the resonance scans of the $\overline{p}\mathrm{He}^{+}$atom.

An enclosed cylindrical glass cell containing a small amount of iodine solid was put in an oven heated to over 500 °C. The power of the laser shot penetrating the cell was measured by a PIN photodiode (PD 2, shown in Fig. 3.14) via an analog-to-digital converter (ADC, LeCroy 2249A) and normalized by the readout without the cell (PD 1).

Molecular tellurium (Te_2) lines are used for the calibration of the wavelength below 500 nm. A glass cell heated to over 600 °C containing tellurium was used in the same way as iodine cell.

Optogalvanic spectroscopy of neon and argon was performed for some wavelength scans for which no I_2 or Te_2 lines can be found. a glass cell, containing a pair of 3 cm-long electrodes made of iron and aligned 30 cm-apart from each other, was filled with neon or argon gas at the pressure of 0.1 kPa. A 50 mA discharge was induced between the electrodes, and laser pulses were fired along the discharge. The resulting optogalvanic signals were detected through a decoupling condenser connected to the anode electrode, and measured by an amplifier and ADC. The consistency with the iodine and tellurium lines were checked for some higher-wavelength lines, and the agreement was good (within few 10 MHz).

Fig.3.17 shows an example of measured iodine absorption lines around 597 nm .

For the reference lines, precise measurement results or empirical formulae of iodine [53] tellurium [54] neon [55] argon [56] were used. The central positions of the peak for the measured absorption spectra were determined by fitting, and compared with theoretical lines. After the calibration, an absolute wavelength was obtained with precisions of 20–50 MHz.

3.7 Data Acquisition

Fig. 3.18 illustrates our data acquisition system. The analog electric signals acquired by the devices are converted to digital data, then transferred to PCs via

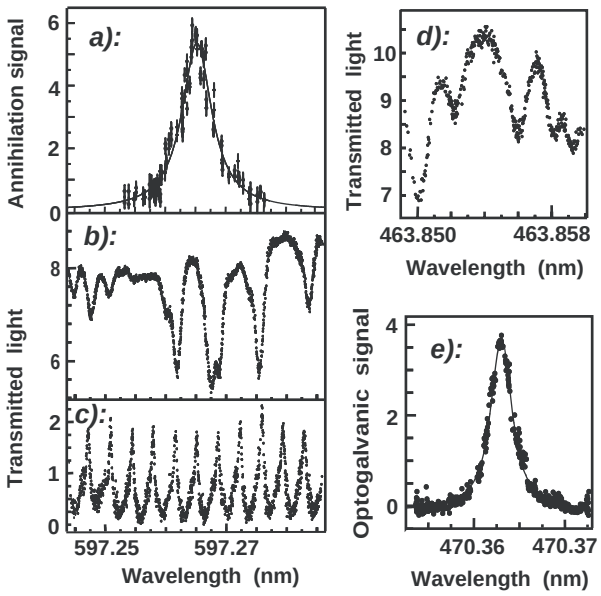

Figure 3.17: a): Resonance profile of the (39, 35)→(38, 34) transition scan. b): Iodine transmission spectrum (the signal ratio of PD 2 to PD 1) measured in the intervals of the antiproton pulses for the above scan. c): Fabry-Perot etalon transmission spectrum simultaneously measured for checking whether the wavemeter offset is constant all over the scan. d): Tellurium transmission spectrum. e): Optogalvanic signal of argon [51].

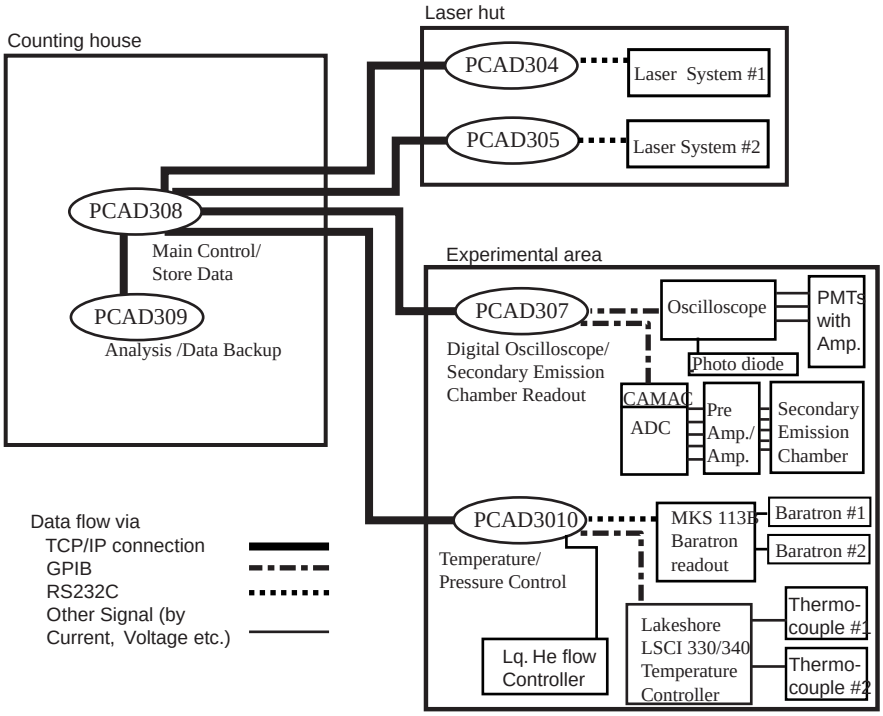

Figure 3.18: Diagram of the data acquisition system. PCAD3xx is the hostname of the PC.

serial or GPIB connections. Programs written for National Instruments LabView are used for the readout of the data. A main PC (PCAD308 in Fig. 3.18) collects all the data from the other PCs through a LAN. The amount of the data is 1 MB/shot, which can be handled by the comparably slow connections of GPIB. The main PC writes the whole data of a shot onto a file, and essential data are converted into a ROOT*[2] file in a compressed format (about 200 kB/shot) for the on-line analysis. The setting of instruments can be changed remotely from the main PC without losing an antiproton pulse.

3.8 Changes of the instruments from LEAR

Table 3.8 summarizes the changes in the instruments from the past experiments at LEAR. The previous high precision spectroscopy was done with a continuous

Facility	LEAR	AD
$\overline{p}$ energy	5.8–21 MeV	5.8 MeV or 80–110 keV (RFQD)
$\overline{p}$ continuous beam	10^4 /s	not available
$\overline{p}$ pulsed beam	$10^{8–9}$/s, every 10 min.	3×10^7, every 85 s.
Laser linewidth	$\sim$ 1 GHz	$\sim$ 600 MHz
UV laser	not available	available
Low target density	not available	available
Detection method	event-counting (digital)	analog method

Table 3.4: Summary of the instrumental changes from LEAR.

antiproton beam (10^4 antiprotons per second) at LEAR, while this time AD can produce only pulse beams of 10^7 antiprotons with an interval of 85 s. This is a fundamental difference of the two facilities.

The whole experimental setup was arranged to be suitable for the analog method. The previous event-by-event detection system consisted of small scintillation counters to detect antiproton beam, "sandwich" counters seven lead/scintillator plates to detect annihilations, and a logic circuit to select events. At the AD, we used a simpler detection system with photomultiplier tubes with a good linearity and fast response (4 ns of fall time), and a digital oscilloscope with a high bandwidth of 1 GHz. A major difference in annihilation spectra is the existence of the π-μ-e background. At LEAR, only antiproton events could be chosen by rejecting muon events, but the current detection system cannot exclude the π-μ-e background. Fortunately

[2]ROOT is a C++ language-based framework for physics data analysis, developed at CERN.

it have never been a serious problem, owing to a high-resolution detectors and the stable beam of the AD.

The laser system was changed from an excimer-pumped dye laser system to a Nd:Yag-pumped dye laser. The laser bandwidth is improved from more than 1.0 GHz to about 0.6 GHz. The laser pulse width is changed from 40 ns to 5 ns, without reducing the power per shot. The short pulse makes the induced peaks in ADATS narrower, and decreases the noise. By performing the iodine calibration with high-precision reference lines, the absolute precision of the frequency improved to 20–50 MHz, from the previous precision of 300 MHz. Since the previous system applied the laser to an antiproton event, the laser was fired more than hundred times in one second. This time the laser was shot only once in 1.5 minutes, which gives us more stable laser shots and requires less times of the dye exchange.

The RFQD made the low-density measurements possible, and the density effects were completely eliminated. A low-density cryogenic target system, Large Čerenkov radiators, and a bending beamline were also prepared for the low-density measurements.

The data acquisition and analysis system were totally rewritten. The new system can remotely change various settings of the devices, for example, the voltage range of the oscilloscope. The analysis program has an ability to display the resonance profile in scanning, which used to be obtained by an analysis after the scan. They also helped to accomplish a more efficient experiment.

Chapter 4

Transition Energy Measurement

4.1 Discovery of New Resonances

For a systematic study of the energies and lifetimes, we had to observe many transitions of the $\overline{p}$He$^+$atom. Among the thirteen transitions observed at LEAR, only one transition was used for the deduction of the CPT limit, and Auger rates of two short-lived states were measured. We succeeded in observations of many more transitions at the AD, and they were studied systematically. Fig. 4.1 shows all the $\overline{p}$He$^+$transitions observed at LEAR and the AD until 2002*[1]. The energies of 13 transitions were measured with precisions of better than 0.2 ppm, and decay rates of 18 states were studied. The resonances which have wavelengths of under 400 nm were observed by using the frequency-doubled laser. Such ultraviolet wavelengths could not be produced by the previous laser system at LEAR. With newly found ultraviolet transitions, we confirmed the lowest metastable states of the v=0 and 1 cascades of both $\overline{p}^4$He$^+$and $\overline{p}^3$He$^+$.

4.2 Analysis of ADATS

The first procedure for the deduction of the transition energy was the fitting of ADATS. What we need to evaluate is the area of the laser resonance peaks in the ADATS, which is proportional to the number of charged pions detected, thus it is also proportional to the number of annihilated $\overline{p}$He$^+$atoms induced by the laser shots. An ADATS contains a continuum spectrum as well, which consists of the $\pi^+ - \mu^+ - e^+$ decay signals (2.2 μs lifetime), and annihilations of the metastable $\overline{p}$He$^+$atoms ($\sim$ 3 μs lifetime on average).

[1]The (41, 36)→(40, 35) of $\overline{p}^4$He$^+$and (41, 36)→(39, 34) of $\overline{p}^3$He$^+$were discovered in 2003.

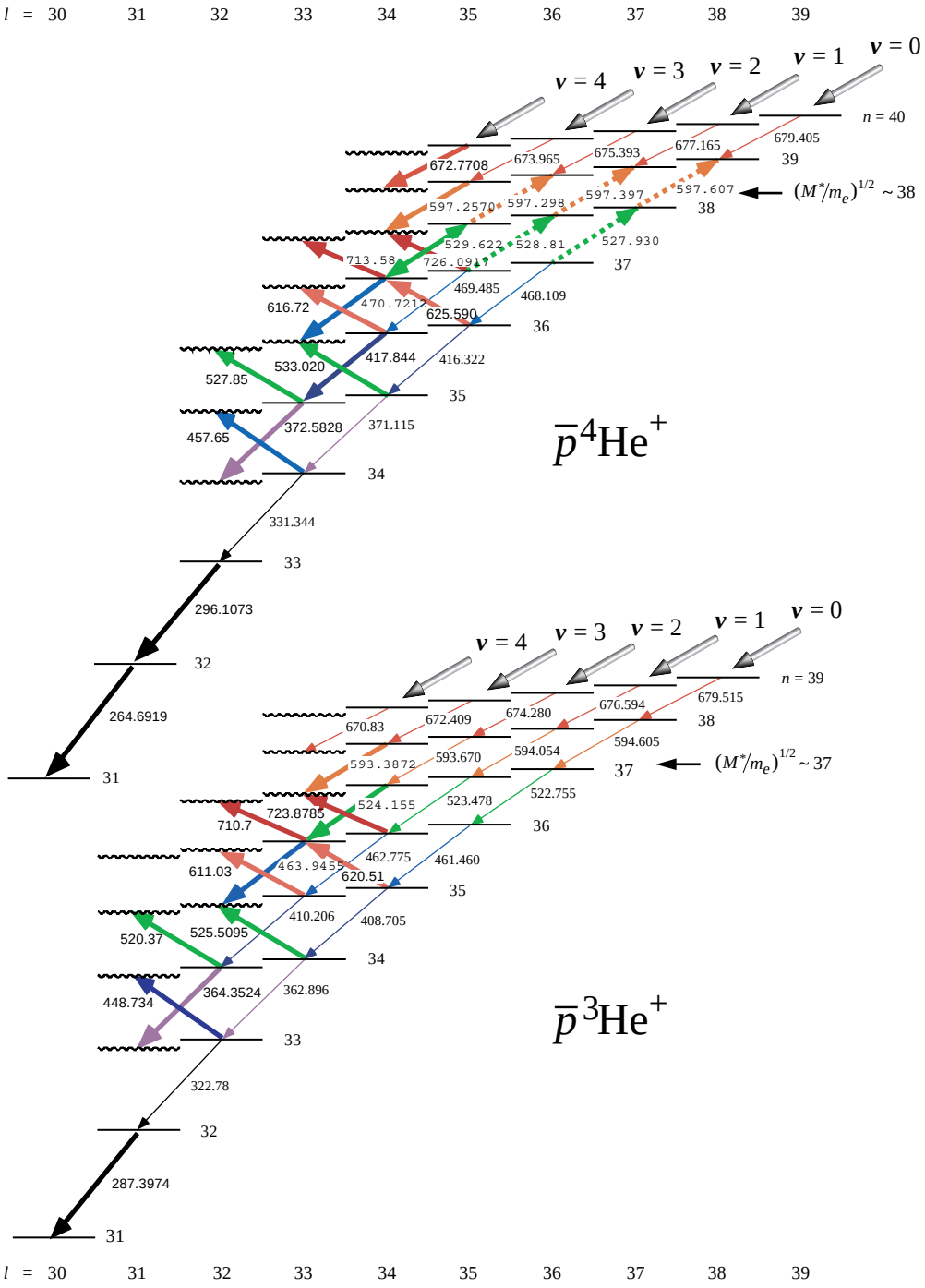

Figure 4.1: $\overline{p}\mathrm{He}^+$transitions observed at LEAR or AD (bold arrows) until 2002. Their wavelengths in nm are shown, particularly in italics for transitions found at LEAR. The transitions with dotted arrows were found by making use of the quenching effect of admixtured hydrogen in helium gas [47].

We fitted the spectrum by a function, in order to subtract the continuum part from the whole spectrum. The shape of the continuum part resembles an exponential function, however, it has more complex shape due to its structure (signals of $\pi-\mu-e$ and several metastable cascade chains of $\overline{p}\mathrm{He}^+$are overlapped). So we took a small fitting region (a few 100 ns) and used a sum of two exponential functions,

$$f(t) = N_1 \exp(-\lambda_1 t) + N_2 \exp(-\lambda_2 t), \tag{4.1}$$

which fits the curvature of the spectrum better. A fixed time range ($\sim$ 50 ns) around the peak position was excluded from the fitting. An ADATS fitted by the "double-exponential" function is shown in Fig. 4.2.

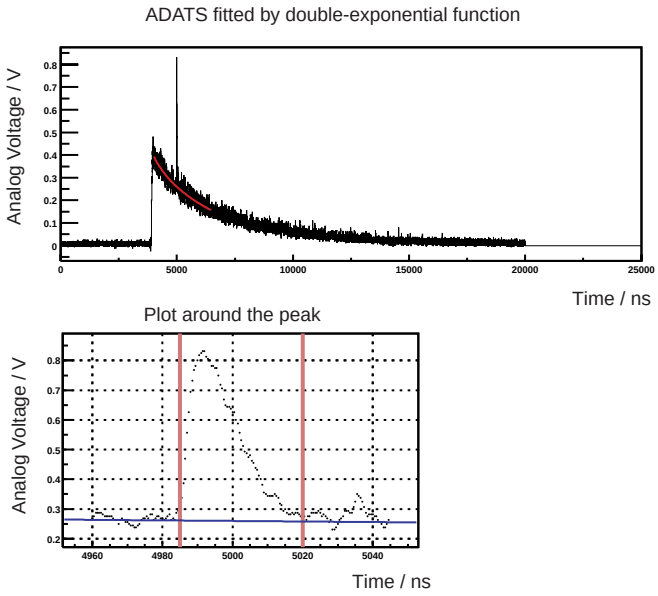

Figure 4.2: ADATS fitted by a double-exponential function. two vertical lines in the magnified spectrum (bottom) indicate the peak range, which is excluded from the fitting.

Since the intensity of the antiproton pulses fluctuates shot by shot, the peak area had to be normalized by the intensity of the pulse. We defined "total area" as the integral of ADATS from a fixed timing (usually $\sim 1\mu$s after the antiproton arrival) to the end of the spectrum (Fig. 4.3) . The value "peak-to-total" can be defined as the peak area divided by the total area. Using this normalized value, the amount of laser-induced annihilations of the $\overline{p}\mathrm{He}^+$atom can be compared for a number of antiproton pulses consistency.

As we used the analog method, spectra were recorded as digitized voltage of analog signal and do not directly tell us the number of events. So we estimated

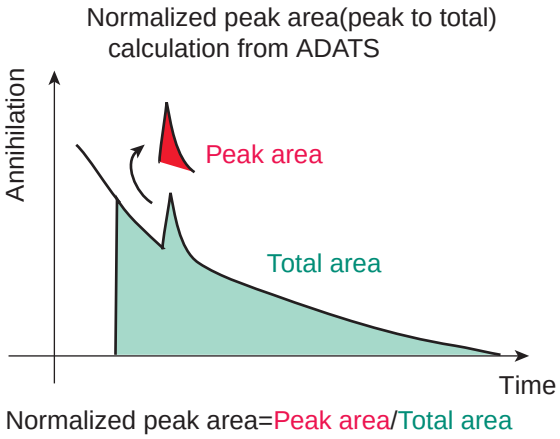

Figure 4.3: Peak area and total area.

the uncertainty of the peak-to-total with the following procedure. We considered the statistical fluctuations of $\overline{p}\mathrm{He}^+$atoms, analog noise of the PMT signal, and the digitization error comes from the resolution of the digital oscilloscope as the error sources. The statistical fluctuations with analog noise were sampled over the fit range (for about 100 ns before and after the peak) by calculating the residual in the fit.The squared-sum of the residual for the fit area ($\equiv \Sigma_{\mathrm{fit}}\sigma_f^2$) was converted to the error of the peak area by a multiplication with the ratio of the area. As the peak area was deduced by:

$$(\text{Peak area}) = (\text{Peak range integral}) - (\text{Subtracted area}), \tag{4.2}$$

where "Peak range integral" is the integral of the ADATS over the peak range including the continuum part, and "Subtracted area" is continuum part in the peak range, the ratio R_A should be

$$R_A = \frac{(\text{Peak range integral}) + (\text{Subtracted area})}{(\text{Fit area})}. \tag{4.3}$$

The digitization error σ_{digit} is determined from the resolution of the digital oscilloscope, and added over the peak range. Finally the total error σ_{stat} was obtained by the following formula.

$$\sigma_{stat} = \sqrt{R_A\Sigma_{\mathrm{fit}}\sigma_f^2 + \Sigma_{\mathrm{peak}}\sigma_{digit}^2}. \tag{4.4}$$

The peak-to-total values with its error obtained in this way were used in the following analysis.

4.2.1 Fitting of Resonance Profiles

A resonance profiles can be drawn by plotting the peak-to-total value against the laser wavelength. We deduced the central wavelength and width of the resonance by fitting the profile curve with a sum of two Voigt functions. The Voigt function is the convolution of a Gaussian and a Lorentzian, of which the explicit formula is written as follows:

$$V(\omega) = \frac{\gamma}{2^{1/2}\pi^{3/2}\delta} \int_{-\infty}^{\infty} \frac{\exp\{-(\omega-\nu)^2/2\delta^2\}}{(\omega_0-\nu)^2+\gamma^2} d\nu, \tag{4.5}$$

where ω_0 is the central frequency, γ is the Lorentzian width defined as the Lorentzian full width at half maximum (FWHM) = 2γ, and δ is the root-mean square width of the Gaussian (FWHM = $\sqrt{2\log 2}\delta$). This is the general shape of resonance profile as far as we consider various sources of broadening, discussed in App. C. The two Voigt functions have identical shape but their centers are separated by $\Delta\nu_{\rm HF}$, which is a parameter introduced to represent the hyperfine splitting. The separation was fixed at theoretical values by Bakalov and Korobov [57], or assumed as (2 ± 0.5) GHz for uncalculated states of unfavored transitions. For the (34, 33)→(35, 32), an asymmetry in the two hyperfine lines was theoretically expected [58]. because of a difference in the SHFS. This effect (a splitting of 200 MHz) was considered in the fitting.

For the integration, we used numerical calculation using the trapezoidal formula, which is the replacement of the integral over infinite range by the sum of small fragments over a finite range (25000 divisions over a range five times wider than the full width). The resonance profiles fitted with Voigt functions are shown in Fig. 4.4 and Fig. 4.5. Fig. 4.4 shows profiles of eleven transitions measured at the low-density target. Fig. 4.5 shows the other two, each of which were measured at three different target densities.

The laser dye used, central wavelength, and target density of the shown resonance scans are summarized in Table 4.2.1.

4.2.2 Deduction of Zero-density Wavelength

As described in Sec. 1.5.1 and Sec. 3.3, the transition wavelengths at zero-density limit were obtained by a linear extrapolation of the results of various densities, or by measuring at a low-density target.

Two transition lines were not measured at the low density condition. One was the (33, 32)→(32, 31) of $\overline{p}^4{\rm He}^+$(296 nm) was not found at the low-density target*[2].

[2]The reason will be presented in Sec. 5.7.3.

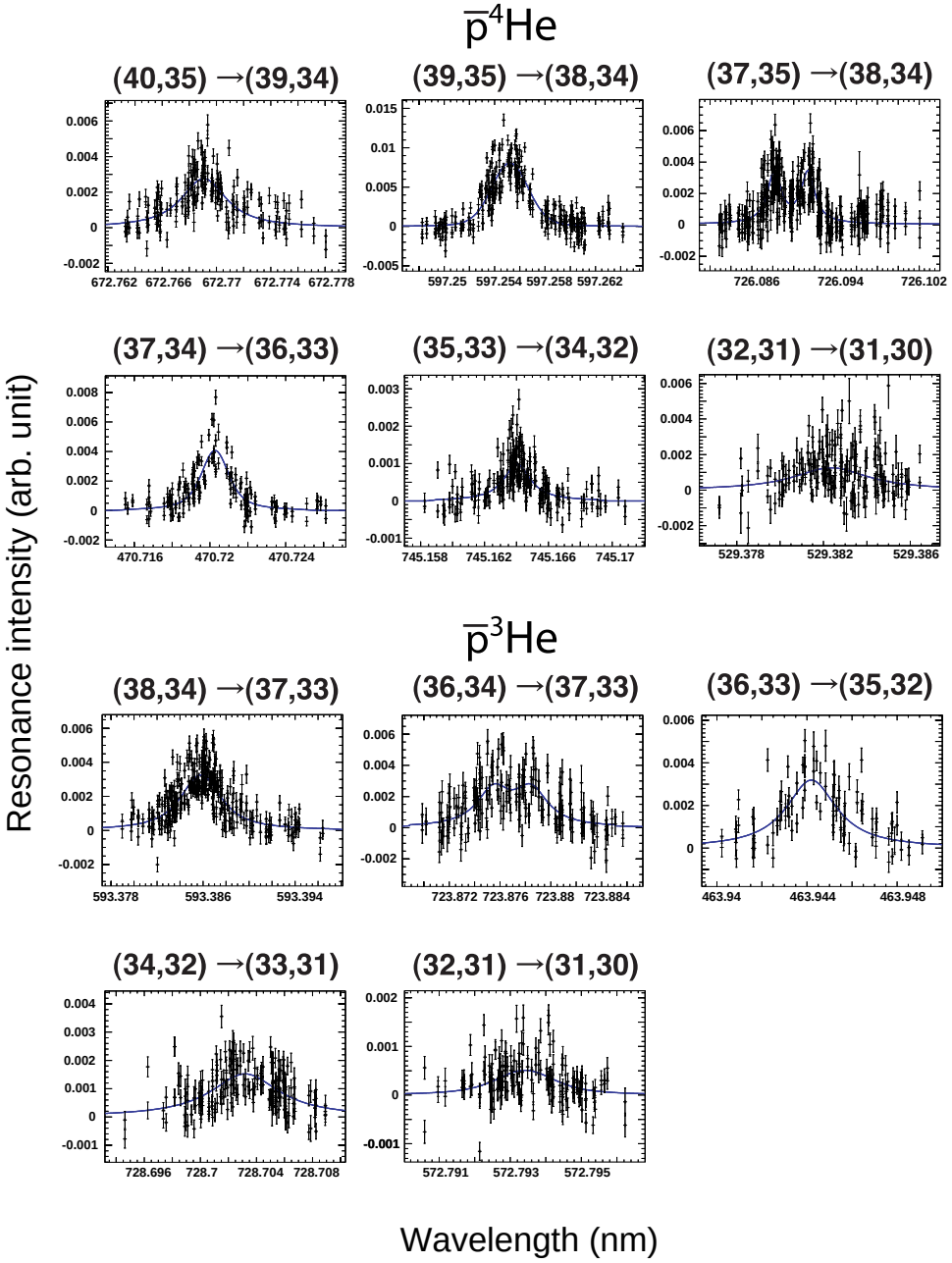

Figure 4.4: Profiles of the laser resonances measured at the low-density target.

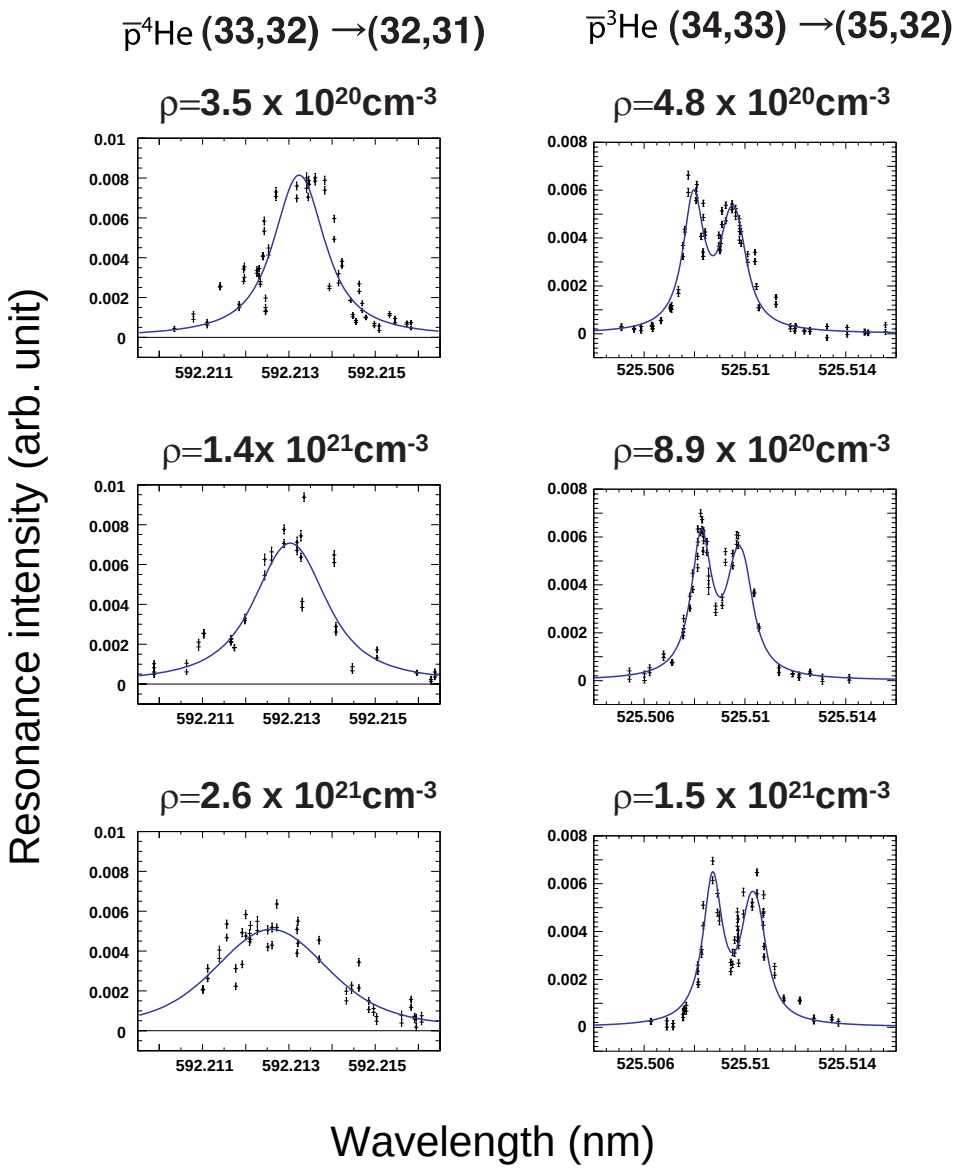

Figure 4.5: Profiles of the laser resonances measured at the high-density target, with the target conditions. Asymmetric shapes are due to the 200 MHz-difference of the SHFS.

Transition	Dye	Central wavelength (nm)	Target density (atoms per cm^3)
$\overline{p}^4He^+$			
(40, 35)→(39, 34)	Oxazine 170	672.769 06	low
(39, 35)→(38, 34)	Rhodamine B	597.255 21	low
(37, 35)→(38, 34)	Pyridine 2	726.897 54	low
(37, 34)→(36, 33)	Coumarin 102	470.720 27	low
(35, 33)→(34, 32)*	Pyridine 2/LDS-751	745.164 04	low
(33, 32)→(32, 31)*	Rhodamine B	592.213 23	3.5×10^{20}
		592.213 02	1.4×10^{21}
		592.212 57	2.6×10^{21}
(32, 31)→(31, 30)*	Coumarine 152	529.382 35	low
$\overline{p}^3He^+$			
(38, 34)→(37, 33)	Rhodamine B	593.385 81	low
(36, 34)→(37, 33)	Pyridine 2	723.876 97	low
(36, 33)→(35, 32)	Coumarine 47	463.944 19	low
(34, 33)→(35, 32)	Coumarine 152	525.508 75	4.8×10^{20}
		525.509 04	8.9×10^{20}
		525.509 53	1.5×10^{21}
(34, 32)→(33, 31)*	Pyridine 2	728.703 19	low
(32, 31)→(31, 30)*	Rhodamine 6G/B	574.793 41	low

Table 4.1: List of the scans shown in Fig. 4.4 and Fig. 4.5. The central wavelengths, laser dyes used for the scans, target densities are shown. Transitions measured with frequency-doubled laser were marked as stars(*) Densities indicated as 'low' are actually 10^{17}–10^{18} cm^{-3}, at which the collisional shift is negligible.

Another was the (34, 33)→(35, 32) of $\overline{p}^3He^+$(525 nm), which was an unfavored transition and low-intensity signals were expected. Fig. 4.6 shows the extrapolations for these two states. The central transition frequencies (remember the shift in frequency is proportional to the density) are plotted against the target density. They were fitted by linear functions and zero-density wavelengths were obtained.

4.2.3 Absolute Wavelength Calibration

All the reference lines used for the absolute calibration of 13 $\overline{p}He^+$transition lines are summarized in Table 4.2.1.

(Table)

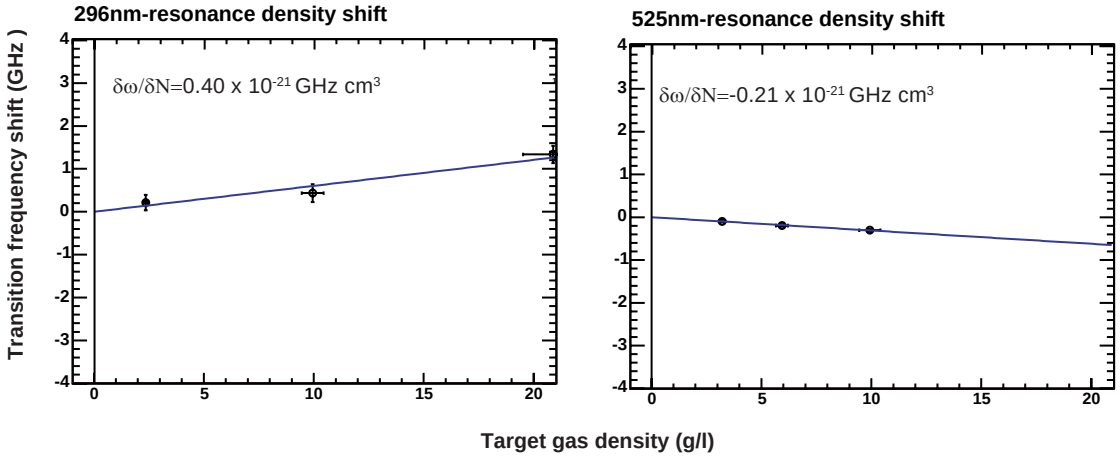

Figure 4.6: Linear extrapolation for the deduction of the zero-density wavelengths of (33, 32)→(32, 31) of $\overline{p}^4\mathrm{He}^+$(296 nm), and (34, 33)→(35, 32) of $\overline{p}^3\mathrm{He}^+$(525 nm). The transition frequencies are plotted against the target density. The density shift $\frac{\partial\omega}{\partial N}$ (slope of the lines) are more than one order of magnitude smaller than that of 597 nm, shown in Fig. 1.7 and Table 1.1. The atomic density 10^{21} cm^{-3} corresponds to 6.65 g/l (see App. A.2).

The measured lines are fitted by Lorentzians, and the center was compared with the reference values. The measured iodine lines are composed by many hyperfine sublevels, and they were Doppler-broadened due to the high temperature. Lines which have symmetrically distributed hyperfine sublevels and wavelengths similar to $\overline{p}\mathrm{He}^+$transitions were selected as the references. Fig. 4.7 is an example of the fitting. Each line was One line in the figure, which was consisted of two nearby lines, was fitted with a sum of two Lorentzians, and one of the centers was compared with the theory. the reproducibility is good for all the lines shown, and the leftmost line is selected to compare with the reference line. Similar analyses were carried out for all the other lines.

4.3 Error Estimation

The experimental errors were determined by the following consideration.

1. Error in the Profile Fitting
   The central wavelengths with its statistical errors were determined by the fittings, but square-root of the reduced χ^2 of the fittings were typically 1.5–2. This is mainly because of the fluctuation of the laser power and irregular

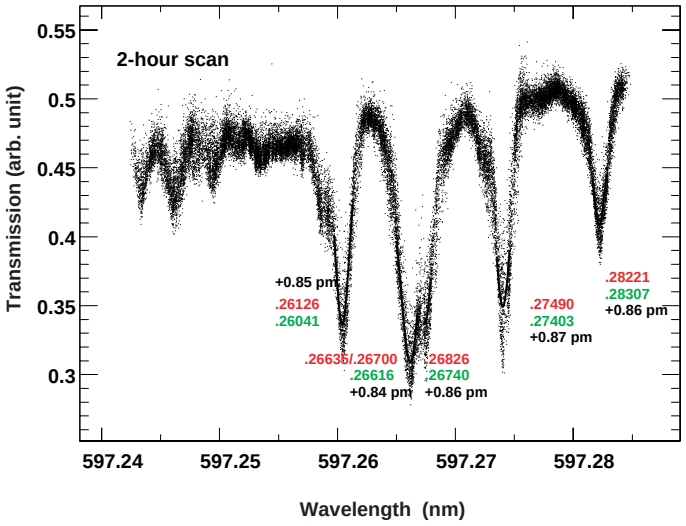

Figure 4.7: An example of fitted iodine lines. The data are taken simultaneously with a scan of $\overline{p}^4\mathrm{He}^+$, (39, 35)→(38, 34) resonance. For each line, (from the top) fitted central wavelength, the theoretically calculated central wavelength, and their difference are shown.

frequency distributions of the laser pulse, the magnitudes of which differ from scan to scan and therefore is unpredictable. To represent these instabilities of the laser, an error was estimated from the reduced χ^2. and added to the statistical error.

2. Error in the extrapolation
   The extrapolation procedure, used in the deduction of the zero-density wavelength, accompanies uncertainty. Errors of 30–50 MHz determined by the linear fittings. Wavelengths measured at the low-density target do not have this uncertainty.

3. Error in the wavelength calibration
   The absolute calibration procedure is also a source of the error. The precision of the the experimental line positions were limited by Doppler effects, statistical fluctuations, and asymmetric distributions of the hyperfine lines. Reference values also have errors, which were given in the references. The stability of the wavemeter in a long time is also considered. The stability of the wavemeter was checked by a helium-neon laser, which wavelength does not change more than 1 Hz, and found to be stable within 15 MHz for over 24 hours. With the above consideration, errors of 20–50 MHz were evaluated.

Finally, 30–200 MHz of errors were put for all the transitions (shown in Table 4.2 in the next section).

4.4 Results and Discussions

Table 4.2 shows the result of transition energy measurements for the 13 transitions. The experimental wavelengths and frequencies are shown with errors. The theoretical values by the two CCR calculations by Korobov [28] and Kino [29] are listed for comparison. Each transition wavelength is determined with a precision of 50–200 ppb, which corresponds to 30–200 MHz in frequency.

Transition	Experiment		Theoretical frequencies (GHz)	
	Wavelength (nm)	Frequency (GHz)	[28]	[29]
$\overline{p}^4\mathrm{He}^+$				
(40, 35)→(39, 34)	672.770 76(10)	445 608.63(7)	445 608.57	445 608.583
(39, 35)→(38, 34)	597.257 04(5)	501 948.80(4)	501 948.765	501 948.769
(37, 35)→(38, 34)	726.091 69(5)	412 885.13(3)	412 885.129	412 885.151
(37, 34)→(36, 33)	470.721 77(9)	636 878.24(12)	636 878.159	636 878.109
(35, 33)→(34, 32)	372.582 83(2)	804 633.05(5)	804 633.053	804 633.020
(33, 32)→(32, 31)	296.107 27(5)	1 012 445.45(17)	1 012 445.630	1 012 445.635
(32, 31)→(31, 30)	264.691 88(5)	1 132 609.2(2)	1 132 609.218	1 132 609.186
$\overline{p}^3\mathrm{He}^+$				
(38, 34)→(37, 33)	593.387 24(8)	505 222.28(7)	505 222.293	505 222.215
(36, 34)→(37, 33)	723.878 50(8)	414 147.48(5)	414 147.518	414 147.479
(36, 33)→(35, 32)	463.945 45(8)	646 180.40(11)	646 180.434	646 180.331
(34, 33)→(35, 32)	525.509 50(9)	570 479.61(10)	570 479.583	570 479.508
(34, 32)→(33, 31)	364.352 35(3)	822 809.18(7)	822 809.178	822 809.124
(32, 31)→(31, 30)	287.397 41(2)	1 043 128.60(8)	1 043 128.620	1 043 128.557

Table 4.2: Experimental transition wavelengths and frequencies, and theoretical frequencies.

The excellent agreement between the experiment and theories is clearly shown in Fig. 4.8. In this figure, the experimental values are centered on the dotted lines, shown with their relative precisions $\Delta\nu_{exp}/\nu_{exp}$ in error bars. The differences of theoretical values from the experimental result are plotted as squares and triangles.

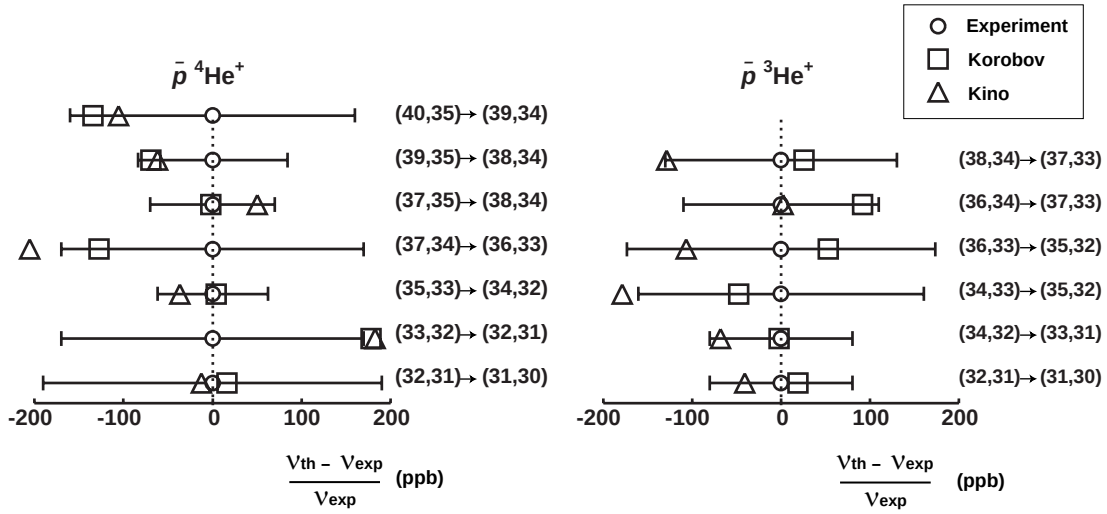

Figure 4.8: Precise comparison of the experimental and the theoretical [28, 29] transition frequencies [45].

4.4.1 CPT test on antiproton mass and charge

The agreement between the experiment and theories enables us to put a CPT limit on the proton-antiproton mass (or charge) difference, which is equal to zero if the CPT theorem holds. Here we describe how we could obtain the CPT limit from the experimental results.

The charge-to-mass ratio of antiproton $Q_{\bar{p}}/M_{\bar{p}}$ has been measured to a high precision of 9×10^{-11} by a Penning trap experiment [59]. Our experiment measures antiprotonic transition energies, which should depend on the antiproton mass and charge. If we assume a hydrogen-like system, this dependence can be written as

$$\hbar\nu = \Delta E \propto M_{\bar{p}} Q_{\bar{p}}^2. \tag{4.6}$$

However, the actual dependence is different from the above, because the system consists of three particles and the antiproton is quite heavy. Instead, we can write the realistic dependence by introducing a parameter f, which depends on the transition:

$$\Delta E \propto M_{\bar{p}} Q_{\bar{p}}^{f-1} = (Q_{\bar{p}}/M_{\bar{p}})^{-1} Q_{\bar{p}}^f = (Q_{\bar{p}}/M_{\bar{p}})^{f-1} M_{\bar{p}}^f. \tag{4.7}$$

If we fix the precisely-known charge-to-mass ratio,

$$\Delta E \propto Q_{\bar{p}}^f \propto M_{\bar{p}}^f. \tag{4.8}$$

The parameter $f = 2$–6 was theoretically evaluated by Kino [37] by calculating the shift of the transition frequency $\delta\nu$ when the input proton mass value is changed

slightly by $\delta M_{\bar{p}}$,

$$f = \frac{\delta\nu}{\delta M_{\bar{p}}}. \tag{4.9}$$

What f indicates is how much the wavelength measurement of the transition can contribute to the CPT test.

Consequently, the CPT limit parameter δ can be obtained by comparing the experimental and theoretical values:

$$\delta = \frac{Q_p + Q_{\bar{p}}}{Q_p} = \frac{M_p - M_{\bar{p}}}{M_p} = \frac{1}{f}\frac{\nu_{th} - \nu_{exp}}{\nu_{exp}}, \tag{4.10}$$

since the theories substituted the precisely-known proton mass for the antiproton mass in the calculations. By averaging $\delta_{\bar{p}}$ for all the thirteen transitions summarized in Table 4.3, The proton-antiproton mass difference

Transition	Wavelength	f	$\delta_{\bar{p}}(10^{-9})$
$\overline{p}^4\mathrm{He}^+(40,\,35)\rightarrow(39,\,34)$	672.770 76(10)	3.11	-39 (51)
$(39,\,35)\rightarrow(38,\,34)$	597.257 04(5)	4.45	-15 (22)
$(37,\,35)\rightarrow(38,\,34)$	726.091 69(5)	6.05	4 (11)
$(37,\,34)\rightarrow(36,\,33)$	470.721 77(9)	2.83	-59 (60)
$(35,\,33)\rightarrow(34,\,32)$	372.582 83(2)	2.54	-7 (24)
$(33,\,32)\rightarrow(32,\,31)$	296.107 27(5)	2.45	74(69)
$(32,\,31)\rightarrow(31,\,30)$	264.691 88(5)	2.38	1(80)
$\overline{p}^3\mathrm{He}^+(38,\,34)\rightarrow(37,\,33)$	593.387 24(8)	3.06	-17 (46)
$(36,\,34)\rightarrow(37,\,33)$	723.878 50(8)	4.05	11(27)
$(36,\,33)\rightarrow(35,\,32)$	463.945 45(8)	2.85	-10 (61)
$(34,\,33)\rightarrow(35,\,32)$	525.509 50(9)	3.63	-31 (44)
$(34,\,32)\rightarrow(33,\,31)$	364.352 35(3)	2.64	-13 (34)
$(32,\,31)\rightarrow(31,\,30)$	287.397 41(2)	2.45	-4 (33)

Table 4.3: Experiment-theory difference of the transition energy $\delta_{\bar{p}}$, and the contribution factor for the test f [45].

$$\frac{M_p - M_{\bar{p}}}{M_p} = \frac{Q_p + Q_{\bar{p}}}{Q_p} = (-3.2 + / - 7.7)\ \text{ppb} \tag{4.11}$$

was obtained, that is, the CPT limit is determined as 10 ppb with 90% confidence level [45].

In the early experiments at AD, we measured four transition wavelengths and obtained a CPT limit of 60 ppb (90% confidence level). This result was published

[60], and referred by Particle Data Group 2002 [61] as the most precise determination of the proton-antiproton mass and charge differences ever done. With the current measurement result, the limit was greatly improved by a factor of fifty from the result at LEAR, by a factor of six even from the previous result.

Chapter 5

Lifetime Measurement

5.1 Measurements of the Radiative Rates

The radiative lifetime of the metastable states have been studied systematically at the AD [62]. Fig. 5.1 shows the experimental result, in which the population of the antiprotons in many states of $\overline{p}\mathrm{He}^+$are plotted against the time elapsed since the formation of the $\overline{p}\mathrm{He}^+$atoms. The initially populated states ($n \sim \sqrt{M^*/m_e}$) lose their population according to the radiative lifetimes (1–2 μs). The lower-lying states have their maximum at later timings, due to the feeding from the upper states. With this measurement along with a cascade simulation, the distribution of the initial population and the average lifetime of the metastable states (~ 3 μs) can be fully explained [62].

5.2 Measurements of the Decay Rates, and Their Anomalies

By the transition-energy measurements described in the previous chapter, theoretical three-body calculations were tested with a very good precision. As the (half) Auger rate is the imaginary part of the complex eigenenergy, the calculations can be checked from another aspect by measuring the decay rates of Auger-dominant states. Decay rates of fifteen Auger-dominant states of the $\overline{p}\mathrm{He}^+$atom were measured at AD, with the same experimental setup as the transition wavelength measurement. Discussions of the decay rate for as many digits as the level energy is difficult both experimentally and theoretically. The experimental difficulty originates from the finite response time in the detection of the antiproton annihilations, and broadening sources for the atomic spectral linewidth (laser linewidth, Doppler width and so on).

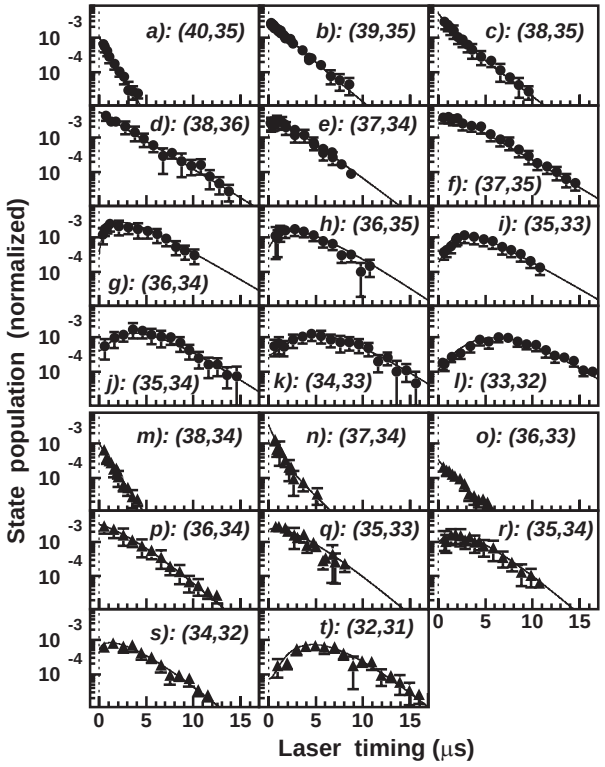

Figure 5.1: Time evolution of the populations of the $\overline{p}$He$^+$states [62]. From a) to l) are the $\overline{p}^4$He$^+$states, and the others are the $\overline{p}^3$He$^+$states. The area of the resonance peak normalized by the antiproton beam intensity is plotted against the laser timing from the formation of the $\overline{p}$He$^+$atoms.

Theoretical difficulty lies in representing continuum-coupled discrete states with a limited set of wave functions, and the small magnitude of the Auger width (order of MHz-GHz) than the transition energies (0.4–1 PHz, visible lights to UV).

Usually the decay rates of the short-lived state are roughly approximated by the relation between the Auger rates and the lowest possible transition multipolarity (Eq.(1.1)),

$$\gamma_A \sim 10^{17-3L}\ \mathrm{s}^{-1} \text{ for } L = 2, 3, 4. \tag{5.1}$$

During the early experiments at AD, two puzzling phenomena related to the decay rates were observed. One was about the (38, 34)→(37, 33) of $\overline{p}^4\mathrm{He}^+$(617 nm). For this transition, the observed central wavelength was difference from the theoretical value by Korobov [23] was 80 ppm (corresponding to 40 GHz), and the resonance was found to have an unexpectedly large FWHM of 20 GHz, values of 1-2 GHz being typical for this L_0 (= 3). This result suggested that its daughter state (37, 33) has a much shorter lifetime than is usual for this L_0.

Another striking deviation from Eq. (1.1) appeared in the search for the transition (32, 31) → (31, 30) (λ = 265 nm) . We expected that the state (32, 31) with $L_0 = 4$ would be the lowest metastable one in the $v = 0$ chain. However, instead of the 265 nm transition, we found the (33, 32)→(32, 31) resonance near the theoretical wavelength 296.11 nm, proving that the state (32, 31) is actually short-lived, and that (33, 32), and not (32, 31), is the lowest metastable state with $v = 0$. We refer to these unexpected large decay rates "anomalies" [63], and their reasons were studied.

5.3 Deduction of Decay Rates - Fast Rates

The deduction of decay rates required different methods according to the magnitude of the rates. Here we discuss the first case.

When the decay rate is fast enough (namely, faster than 6 ns^{-1}), a transition to the state is observed as a broad resonance having a larger natural width than the laser linewidth ($\sim$ 1 GHz at the high resolution mode) Fig. 5.2 shows such broad resonance profiles measured in this work. The (37, 34)→(38, 33) and (36, 34)→(37, 33) were measured at four different density conditions (the temperature was at 5.5 K and the pressure at 25, 60, 100 and 200 kPa), but no significant density dependence was observed. The rest of them were measured at standard target condition (5–6K and 20–30 kPa),

Each resonance profile was fitted with two identical Voigt functions separated

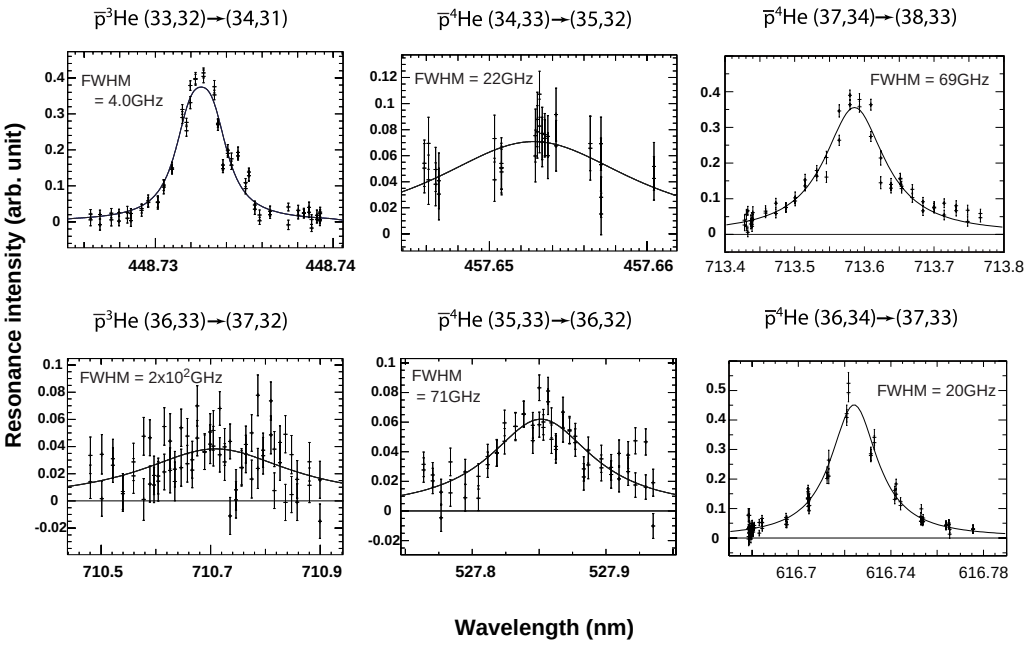

Figure 5.2: Profiles of wide resonances [63, 64].

by a fixed splitting, in the same way as the deduction of the transition wavelengths. Several factors contribute to the observed line width. They include the natural width as well as Doppler and collisional broadening, and instrumental effects such as the laser bandwidth and power broadening. With the consideration of the general lineshape including all these factors (App. C), the fitting was done with a fixed width of Gaussian component at the laser linewidth with Doppler broadening, and the Lorentzian width was obtained. The Lorentzian width was considered to be approximately equal to the natural width $\Delta\nu_{\rm nat}$ because the other factors such as the collisional and power broadening were estimated to be very small. Finally, $\Delta\nu_{\rm nat}$ was converted to the decay rates γ by their inverse relationship (Eq. (1.3)).

The evaluations of the broadening factors other than the natural widths are described in the following sections.

5.3.1 Laser Linewidth

The laser linewidth, which is the second largest component of the total width, was evaluated by analyzing the spectra of the interferometers. In the interferometric spectra what we have (an example is shown in Fig 5.3), there are several peaks (fringes), of which the distance corresponds to the free spectral range (FSR).

The width of a fringe consists of its intrinsic width determined by finnesse ($\sim$

10) and the broadening by the laser linewidth.

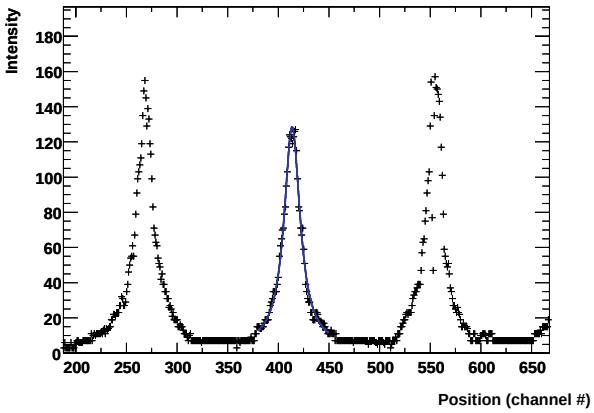

Figure 5.3: A spectrum of the third interferometer for a high-resolution laser. The peak is fitted with a Lorentzian.

The laser lineshape in the broadband mode is a collection of 15–20 Lorentzian lines spaced by 500 MHz, corresponding to the longitudinal modes defined by a 30 cm-long cavity. The laser linewidth can be separated from the intrinsic profile (Lorentzian-shaped) by treating it as a Gaussian. The unit of fringe width can be converted from number of bins to GHz by normalizing with the fringe distance, which is known to be 81GHz (=FSR).

Fig. 5.4 shows the peak widths of high-resolution mode lasers of various wavelengths, plotted against laser wavelength λ. They were obtained by fittings with Lorentzians. The laser linewidths are about 1 GHz or less for these cases, so only the intrinsic width (8 GHz, corresponding to the FSR divided by the finnese) can be obtained.

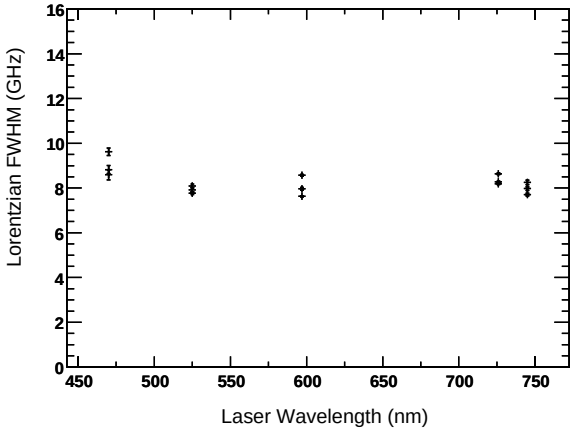

Figure 5.4: Widths of the fringes (narrow-linewidth laser).

Fig. 5.5 shows the peak widths for lasers in the broadband mode, obtained by Voigt function fitting with Lorentzian width fixed at 8 GHz.

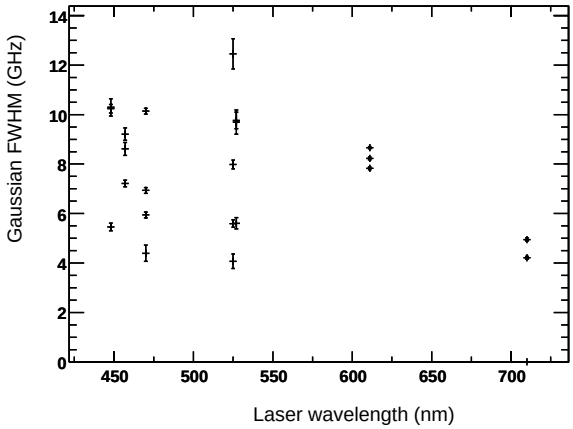

Figure 5.5: Width of the fringes (broadband laser). They were fitted by Voigt functions, and the Gaussian FWHM is shown.

From the above analysis, it was concluded that the laser linewidths in the broadband mode were 4–10 GHz. The large uncertainty is due to the smallness of the broadening effect compared to the intrinsic width. However, such uncertainty does not affect for the deduction of natural widths of broader than 10 GHz. This analysis result is consistent with an observation of the (34, 33)→(35, 32) transition (525 nm) with a broadband mode laser. The resonance has a narrow (10 MHz-order) natural width, and appeared as a full width of 8 GHz, including the hyperfine splitting of about 1.5 GHz (shown in Fig. 5.6).

As the resonance (33, 32)→(34, 31) have a natural width of a few GHz, a measurement with the high-precision laser was performed. For this case, the fourth interferometer (FSR=3.8 GHz) was analyzed with a similar method, and the laser width was deduced as 0.6–1.3 GHz.

5.3.2 Doppler, Power and Collisional Broadening

The other broadening effects, of which details are described in App. C, are much smaller than the laser linewidth.

The Gaussian width includes contributions from the Doppler broadening. For our target temperature ($\sim$ 6 K) and photon wavelength (448–714 nm), the Doppler widths were calculated as 0.3–0.5 GHz, assuming Maxwell-Boltzmann velocity distribution of the atoms.

The power and collisional effects contribute to the Lorentzian width. For the

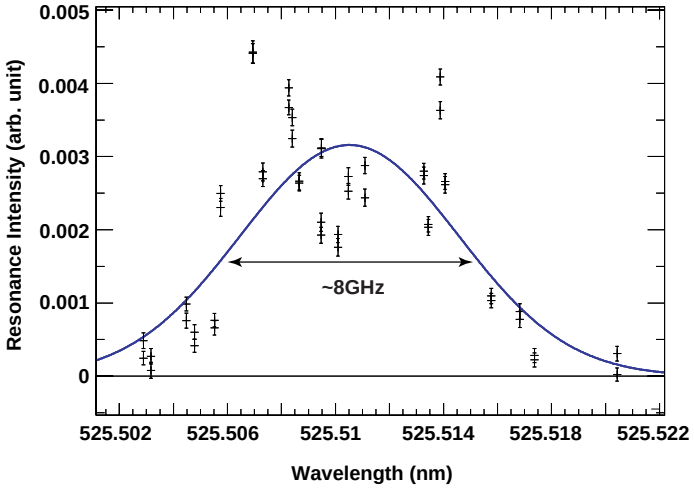

Figure 5.6: Resonance profile of the (34, 33)→(35, 32), scanned with a broadband mode laser. (cf. resonance profiles of the same transition scanned with the high-resolution laser, shown in Fig. 4.5.)

measurement of the wide resonances, the Rabi frequency Ω can be calculated with the following parameters,

- laser power density: 2 mJ/cm^2 (at maximum),
- laser pulse length: 5 ns,
- dipole moment: 0.03 debye (at maximum),

and we obtain Ω=0.5 GHz. For the natural widths of larger than 2 GHz, the power broadening ($\sim \frac{1}{2}\Omega^2/\gamma$) should be 0.1 GHz or smaller. The magnitude of collisional broadening for the (39, 35)→(38, 34) of $\overline{p}^4\mathrm{He}^+$, which has one of the largest collisional shifts,was measured at LEAR [27]. The density dependence of the collisional broadening $\frac{\partial\gamma_{\mathrm{coll}}}{\partial N}$ *1 was measured as 0.30±0.15 (10^{-21} GHz/cm^{-3}). Since our target condition was 2–3 $\times 10^{20}$ cm^{-3}, we expect no collisional broadening more than 0.1 GHz.

5.3.3 Baseline Correction

Although the fitting function for ADATS (the double-exponential function) is good for representing the curvature in a small time range, it does not fit the complex

[1] γ_{coll} is the half width of the collisional broadening.

shape of the ADATS perfectly. The calculated peak-to-total is known to have a small offset from zero, which amounts less than 0.5 % compared to the full height of a good-intensity resonance such as the (39, 35)→(38, 34) of $\overline{p}^4\mathrm{He}^+$. Such a small baseline offset does not matter for the wavelength measurement of intense resonances, but it is significant for the width measurements of some unfavored transitions with small dipole moments.

In order to correct the baseline, the peak-to-total was evaluated for various widths of the peak range (the time span excluded from the fitting). Then a linear relation between the offset and the peak-range width was assumed, and the baseline offset was derived.

5.3.4 Error Estimation

The treatment of the statistical error and the power fluctuation of the laser were the same as that of transition energy measurements. To evaluate the uncertainty coming from the laser width, the resonance profiles were fitted with the laser width fixed at center and edge-values in the possible range (e.g. 4, 7, 10 GHz for 4–10 GHz-wide lasers), and the differences in the resulting widths were taken as the error. For weak signal resonances, the error arising from the uncertainty of the baseline offset were evaluated. In addition, an error of 1 GHz was put for the collisional and power broadening effects, uncertainty of the hyperfine splittings, and deviation of the laser profile from a Gaussian. The estimated errors are summarized in Table 5.1.

State	Natural Width	Errors (GHz)					
	(GHz)	stat.	power	laser width	baseline	other	total
$\overline{p}^4\mathrm{He}^+$(38, 33)	61	1.9	3.8	0.7	-	1	4.1
(37, 33)	18	0.5	0.5	2.2	-	1	2.5
(36, 32)	101	7.5	7.2	0.3	0.6	1	10
(35, 32)	18	4.3	-	1.8	7.3	1	8.8
$\overline{p}^3\mathrm{He}^+$(37, 32)	198	30	26	0.25	8.9	1	41
(34, 31)	2.9	0.09	0.20	0.09	-	1	1.0

Table 5.1: Error estimation for the decay rates (in GHz). Some errors are not shown (marked as '-') as they were negligibly smaller than the other errors.

5.4 Deduction of Decay Rates - Slow Rates

5.4.1 Tails of the Laser Resonance Peaks

For the resonances such that the natural widths are much smaller than the instrumental widths, no influence can be observed in their line shapes. Their corresponding lifetimes are, however, long enough to produce tails in the ADATS laser resonance peaks. The time profile of the resonance peak intensity $I(t)$ can be represented as a convolution of $I_{\rm instr}(t)$, which is the instrumental time profile of the laser peak, and an exponential function $\exp(-\gamma t)$. The exponential function represents the decay of the daughter state with a rate γ. while $I_{\rm instr}(t)$ is determined by the time profile of the laser pulse (3–5 ns wide) and also has a tail mainly produced by the fall time (4.3 ns) of the PMT.

Fig. 5.7 shows the resonance peaks of five transitions. The topmost panel shows the resonance peak of the (37, 34)→(38, 33) transition (714 nm). This is included to show the instrumental shape $I_{\rm instr}(t)$, as its 2 ps lifetime is much smaller than the laser pulse width. In the other four cases, tails corresponding to daughter state lifetimes of order 10 ns are convoluted in the instrumental profile $I_{\rm instr}(t)$. For these four transitions, the decay rate of their daughter state were determined by an analysis of the tails.

5.4.2 Fitting Procedure

We deduced γ by fitting the convoluted function to the peaks in the small range indicated in the figure. In this range, we assumed $I_{\rm instr}(t)$ is approximately proportional to $\exp(-\gamma_{\rm instr} t)$, where $\gamma_{\rm instr} = (5-6\ {\rm ns})^{-1}$ was determined by fitting the laser peaks of very fast decaying states.

The fitting function was a convolution of two exponential functions,

$$F(t) = \frac{I_0}{\gamma_A - \gamma_{\rm instr}}[\exp\{-\gamma_A(t - \frac{\log(\gamma_{\rm instr}/\gamma_A)}{\gamma_{\rm instr} - \gamma_A})\} - \exp\{-\gamma_{\rm instr}(t - \frac{\log(\gamma_{\rm instr}/\gamma_A)}{\gamma_{\rm instr} - \gamma_A})\}], \tag{5.2}$$

where I_0 is a parameter, and $\log(\gamma_{\rm instr}/\gamma_A)/(\gamma_{\rm instr} - \gamma_A)$ is introduced to let F(0) be the highest point of the function. The instrumental rate $\gamma_{\rm instr}$ and the $t = 0$ position were fixed at the fitting, and I_0 and γ_A were obtained. Due to the width (5 ns) of the laser pulses, the $t = 0$ position is determined with a few nanoseconds of uncertainty.

The errors were calculated from the statistical errors obtained from the fitting procedure (2%), the uncertainty of $\gamma_{\rm instr}$ and the $t = 0$ position (5-9%), and the

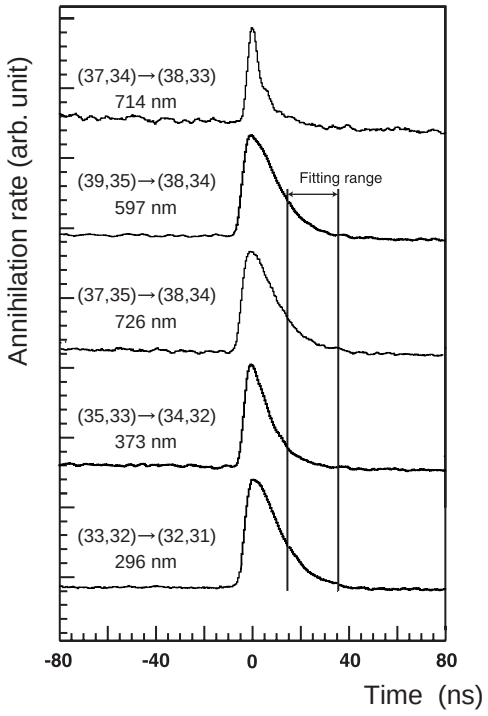

Figure 5.7: Comparison of the resonance peaks in ADATS. For each transition, typically spectra of about 100 AD shots were summed up. The peak heights were normalized to the same value.

deviation of the result by a shift of the fit range within ±5 ns (2-5%).

Measurements were done at three or four target densities for all the four transitions, and no significant change was observed for the decay rates. For the state (38, 34), we used the average of the results of two transitions, (39, 35)→(38, 34) (λ = 597 nm) and (37, 35)→(38, 34) (λ = 726 nm).

5.5 Deduction of Decay Rates - Intermediate Rates

For the states that do not show either wide resonances or prolongation of the spikes, we cannot measure their decay rates directly. The daughter states of an unfavored [the (35, 33)→(36, 32) of $\overline{p}^3\mathrm{He}^+$] and five favored resonances [to the (37, 33), (35, 32), (33, 31), and (31, 30) of $\overline{p}^3\mathrm{He}^+$, and the (39, 34) of $\overline{p}^4\mathrm{He}^+$from each $(n+1, l+1)$ state] come under this category. We can conclude that their decay rates are between two experimental limits. The lower limit (0.1 ns^{-1}) is determined mainly by the instrumental prolongation effect of the laser spike, as mentioned above. The upper limit is determined by the laser linewidth. It is 6 ns^{-1} (corresponding to 1

GHz width) for the high resolution scans, and 20 ns^{-1} for the broadband scan. The latter value was obtained by assuming the laser bandwidth in broadband mode is wider than 4 GHz.

5.6 Results

In Table 5.2 and Fig. 5.8 we summarize the deduced decay rates of the short-lived daughter states and compare them with the Auger values calculated by various authors [28, 29, 65, 66]. As the radiative rate is comparatively small, the Auger rate is here by far the largest component of the total decay rate. For comparison, we also include data at LEAR [33] on a few other states (including radiative-dominated states), together with their theoretical values.

Most of the experimental decay rates are roughly in agreement with the calculations and the approximation formula (Eq. (1.1)). However, we found exceptional states, which are the (37, 33), (35, 32) and (32, 31) of $\overline{p}^4He^+$, and the (34, 31) of $\overline{p}^3He^+$. Their observed rates far exceed those expected from Eq. (1.1) and most of the theoretical values, which are called anomalies, as defined in Sec. 5.2.

A noteworthy state is the (36, 32) of $\overline{p}^3He^+$. Although an *ab-initio* calculation [66] predicted a large anomaly, its decay rate was found to be non-anomalous. Another calculation [65] was done by introducing continuum-coupled wave functions explicitly in the equation of motion, and resulted in a non-anomalous value. After the experiment was performed, Korobov presented a new calculation result with the CCR method [28]. His new result seems to be in good agreement with our experiment, thus it proves that the coupling with continuum is well represented by his new method.

5.7 Discussions on Anomalies in the Decay Rates

5.7.1 Energy Level Diagram with Electron-excited States

Before discussing the anomalies, the electron-excited $\overline{p}He^+$states should be introduced. Fig. 5.9 and Fig. 5.10 shows the energy levels of $\overline{p}^4He^+$and $\overline{p}^3He^+$, respectively. The solid lines denotes metastable states and wavy lines denotes short-lived, or Auger-dominated ones. The metastable zone is shown on the right as in previous diagrams (e.g. Fig. 4.1), and includes energy levels corresponding to a 1s 'ground' electron ($n_e = 1$, $l_e = 0$) and an antiproton with $n_{\bar{p}}$ ($\sim l_{\bar{p}}$), of order 35. We now include on the left some of the electron-excited states ($n_e = 2, 3, \dots$) lying below

State	L	Experimental values	KB-S [66]	KRT [65]	KB [28]	KN [29]
$\overline{p}^4\mathrm{He}^+$						
(38, 33)	2	$(3.85 \pm 0.26)\times10^{11}$[63]	3.1×10^{11}	3×10^{11}	3.07×10^{11}	6.45×10^{11}
(36 ,32)*	2	$(6.35 \pm 0.65)\times10^{11}$	5.8×10^{11}	6.1×10^{11}	5.59×10^{11}	5.95×10^{11}
(39 ,34)	3	$(0.1\text{–}6)\times10^{9}$	7.7×10^{8}	1×10^{9}	8.21×10^{8}	
(38, 34)	3	$(1.11 \pm 0.07)\times10^{8}$ [63]	1.3×10^{8}	1.4×10^{8}	1.344×10^{8}	
(37, 33)	3	$(1.11 \pm 0.16)\times10^{11}$[63]	5.7×10^{9}	3×10^{10}	4.21×10^{10}	4.38×10^{10}
(36, 33)	3	$(2.2 \pm 0.8)\times10^{8}$ [33]	2.4×10^{8}		2.42×10^{8}	3.31×10^{8}
(35, 32)*	3	$(1.10 \pm 0.53)\times10^{11}$	3.7×10^{9}	7.5×10^{9}	5.76×10^{9}	6.04×10^{9}
(34, 32)	3	$(2.36 \pm 0.47)\times10^{8}$	2.2×10^{8}	2.3×10^{8}	2.260×10^{8}	2.5×10^{8}
(39, 35)	4(rad.)	$(6.5 \pm 0.2)\times10^{5}$ [33]	7.0×10^{4}	8×10^{4}		
(37, 34)	4(rad.)	$(6.7 \pm 0.5)\times10^{5}$ [33]	1.9×10^{5}			
(32, 31)	4	$(1.17 \pm 0.12)\times10^{8}$ [63]	6.1×10^{5}		4.2×10^{4}	
$\overline{p}^3\mathrm{He}^+$						
(37, 32)*	2	$(1.24 \pm 0.26)\times10^{12}$	6.6×10^{11}		6.71×10^{11}	6.74×10^{11}
(37, 33)	3	$(0.1\text{–}6)\times10^{9}$	3.3×10^{8}	3.8×10^{8}	3.52×10^{8}	
(36, 32)	3	$(0.1\text{–}20)\times10^{9}$	1.1×10^{12}	1.2×10^{8}	4.8×10^{8}	7.0×10^{8}
(35, 32)	3	$(0.1\text{–}6)\times10^{9}$	6.8×10^{8}	7×10^{8}	6.76×10^{8}	4.1×10^{8}
(34, 31)*	3	$(1.84 \pm 0.65)\times10^{10}$	3.5×10^{10}		6.7×10^{7}	1.09×10^{11}
(33, 31)	3	$(0.1\text{–}6)\times10^{9}$	6.9×10^{8}	6.9×10^{8}	6.85×10^{8}	7.4×10^{8}
(31, 30)	3	$(0.1\text{–}6)\times10^{9}$			2.76×10^{8}	2.5×10^{8}

Table 5.2: Experimental decay rates and theoretically calculated Auger decay rates [28, 29, 65, 66] in s^{-1} [64]. L is the lowest transition multipolarity of the Auger decay. All the data including the past measurements [33] are shown. For the (39, 35) and (37, 34) states of $\overline{p}^4\mathrm{He}^+$, the radiative decay is dominant and the experimental decay rates cannot directly be compared with theoretical Auger rates. Some of the experimental values are not directly determined and only the possible ranges are shown (see the case of Sec. 5.5). The states marked with stars (*) were measured at only the standard target condition (6 K, 20–30 kPa). The other states were measured at various density target conditions and the consistency was checked. For the (32, 31) of $\overline{p}^4\mathrm{He}^+$, the decay rate at standard target condition is plotted.

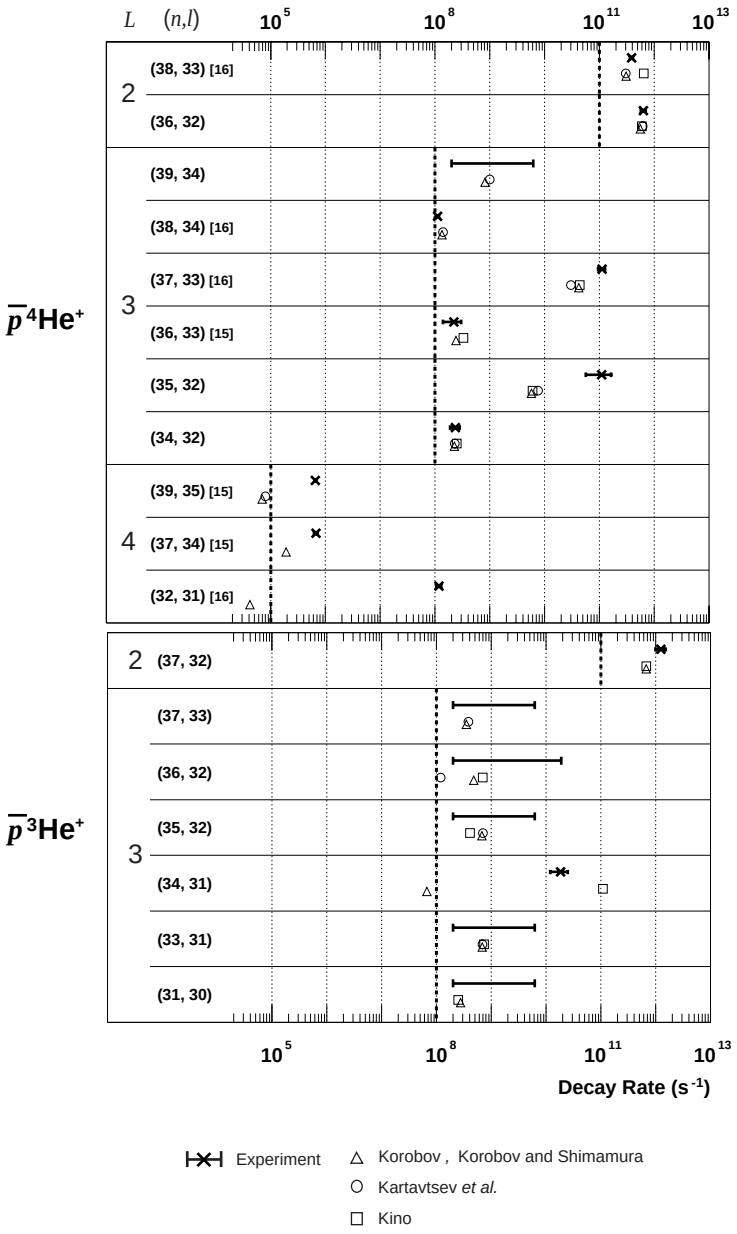

Figure 5.8: Experiment-theory comparison of the decay rate in logarithmic scale [64]. All the data including past measurements [33, 63] are shown. The bold vertical dotted lines show the typical Auger rates estimated by Eq. (1.1). The experimental points without crossed markers show that the rates are between two experimental limits, and not directly determined (see the case of Sec. 5.5). Some of the experimental error bars are too small to see.

the $n_e = \infty$ (*i.e.* $\bar{\mathrm{p}}\mathrm{He}^{++}$ ion) states. These electron-excited states are strongly coupled to the continuum, which usually means that precise energy level calculation is

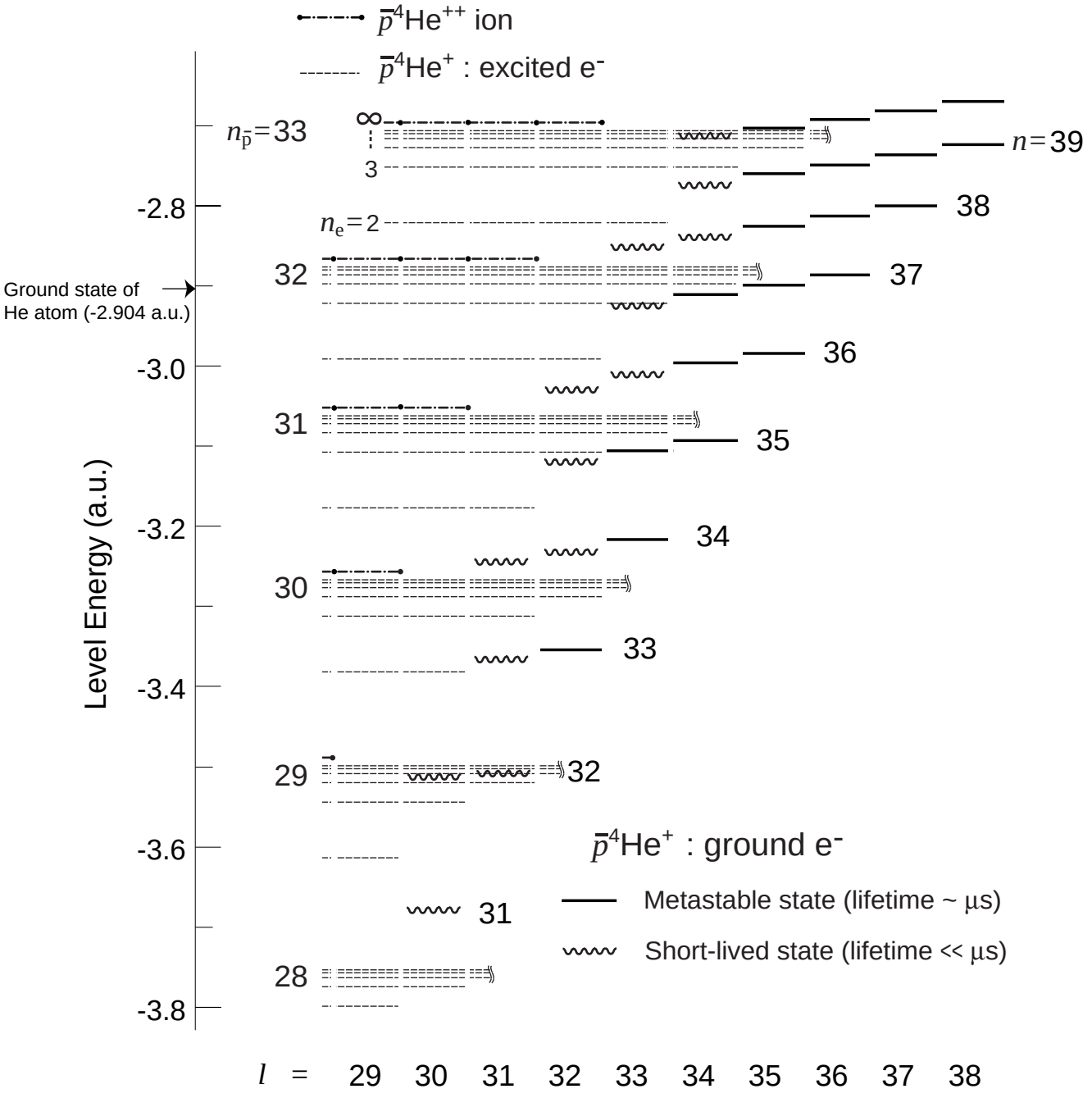

Figure 5.9: Energy diagram of $\overline{p}^4He^+$with its ionized and electron-excited states [63].

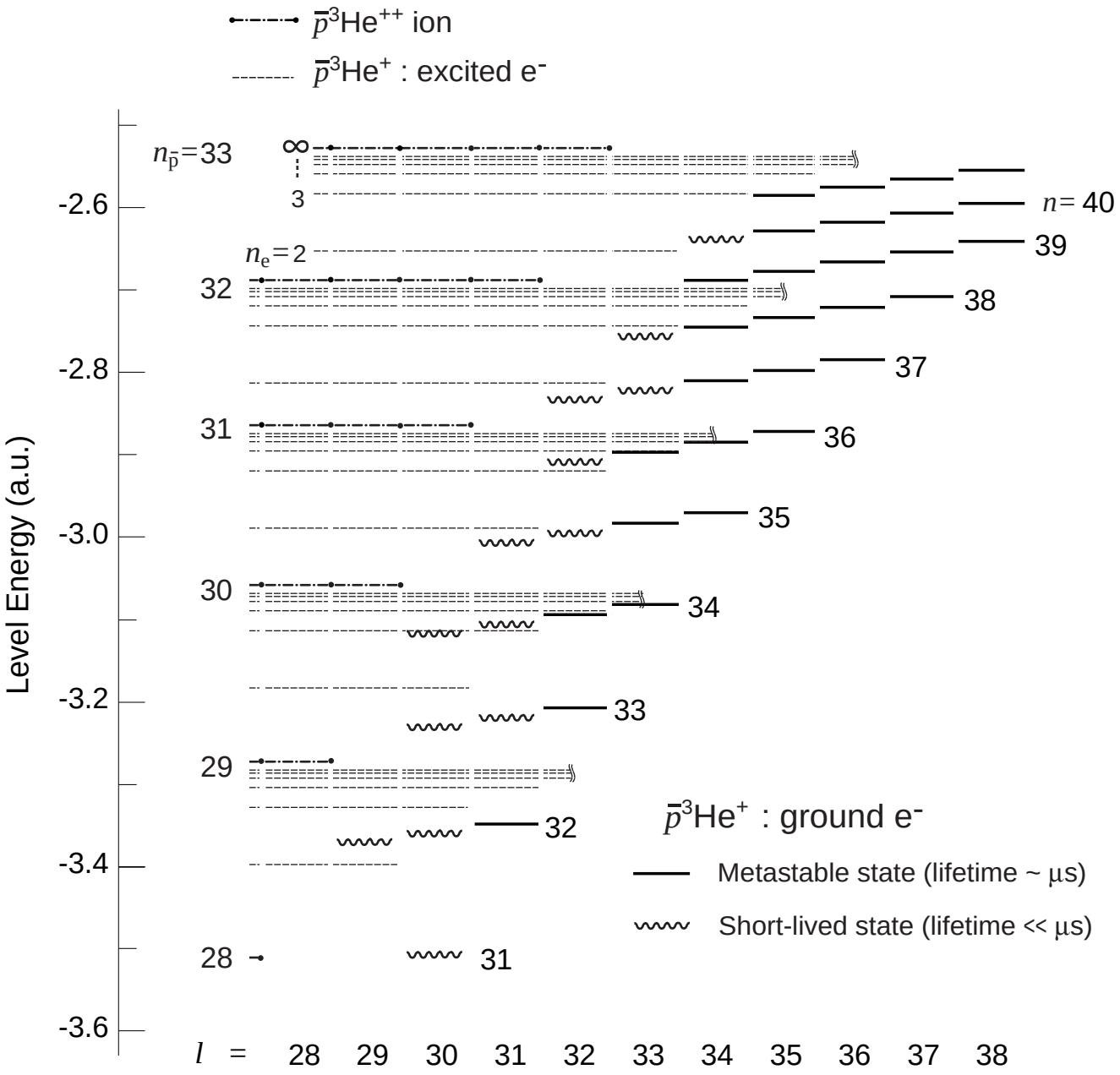

Figure 5.10: Energy diagram of $\overline{p}^3He^+$with its ionized and electron-excited states.

difficult. However, as the excited electron orbits are far from those of the antiproton for $n_{\bar{p}}$ smaller than about 40, their energies can be approximated [65] by:

$$E = -\frac{m_{\bar{p}} m_\alpha}{m_{\bar{p}} + m_\alpha} \frac{Z^2}{2n_{\bar{p}}^2} - \frac{1}{2n_e^2}, \tag{5.3}$$

in atomic units (App. A.1). Here Z (=2) is the atomic number of helium. The energies determined from Eq. (5.3) are shown in the figure (note however that the actual energies have a slight dependence on l_e and are not perfectly degenerate). The maximum $l_{\bar{p}}$ and l_e being $n_{\bar{p}} - 1$ and $n_e - 1$, the maximum l is $n_{\bar{p}} + n_e - 2$.

Since these electron-excited states have very short lifetimes, it is not normally necessary to pay any attention to them as they are not directly concerned with the metastability. This ceases to be the case when they has a close energy to a metastable state, as is explained in the next section.

5.7.2 State Mixing with Electron-excited States

It was pointed out by Kartavtsev *et al.* [65, 67] that the (37, 33) antiprotonic state with the electron in ground state is strongly coupled with an $l = 33$ three-body state of the configuration $(32, 31)_{\bar{p}} \otimes (3d)_e$, as they have nearly the same energy (cf. Fig. 5.11). This accidental degeneracy was expected to give the state (37, 33) an anomalously large decay rate. The admixture of the excited electronic configuration enhances the decay rate, while the dipole moment of the transition to this state may still be normal for $\Delta v = \Delta(n - l - 1) = 2$. The value predicted by Kartavtsev *et al.* is in fact fairly close to our observation. The variational calculations by Korobov and Kino, which include the above configuration mixing effects automatically, yield values which are also close to the experimental ones. Thus, the anomaly in the state (37, 33) is very well explained in terms of the mixing effect of the electron-excited configuration.

For the (35, 32) of $\overline{p}^4\mathrm{He}^+$and (34, 31) of $\overline{p}^3\mathrm{He}^+$, the situations resemble the case of the (37, 33) state of $\overline{p}^4\mathrm{He}^+$. Their lowest transition multipolarity L is 3, Theoretical Auger rates are also faster than the typical rates for the (35, 32) of $\overline{p}^4\mathrm{He}^+$, but there is a large discrepancy between the two CCR calculations for the (34, 31) of $\overline{p}^3\mathrm{He}^+$. Korobov obtained an anomalous value in the old calculation [66], but his latest result is [28] non-anomalous, while the value by Kino [29] is anomalous. As are illustrated in Fig. 5.11, the configurations $(31, 30)_{\bar{p}} \otimes (3d)_e$ for the (35, 32) state of $\overline{p}^4\mathrm{He}^+$, and $(30, 29)_{\bar{p}} \otimes (3d)_e$ for the (34, 31) state of $\overline{p}^3\mathrm{He}^+$can be the reason for the anomalies in the same way. For the latter case, the possibility of the influence by an electron-excited state was pointed out by Kartavtsev [65].

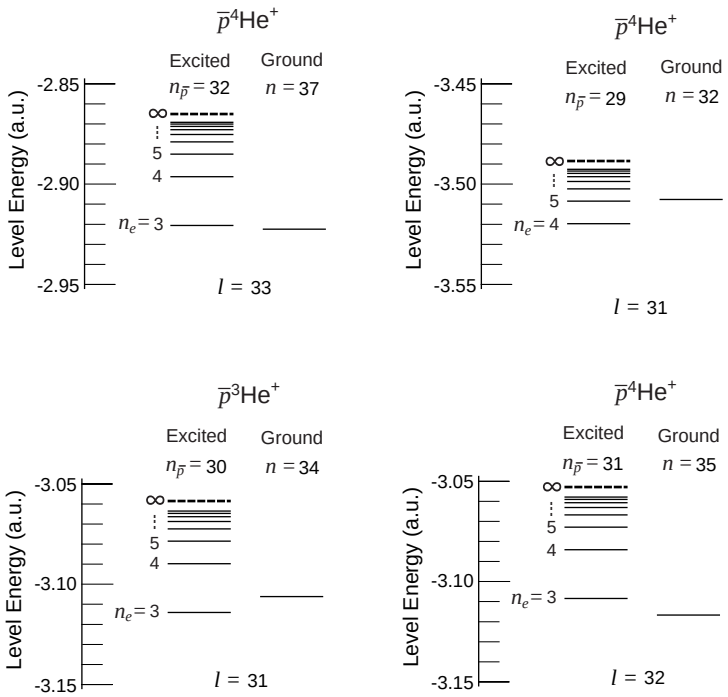

Figure 5.11: Energy diagrams of four states of normal $\overline{p}He^+$atom (ground electron configuration), and their neighbor electron-excited states [63, 64]. The energy values were obtained by Eq. (5.3) and [23].

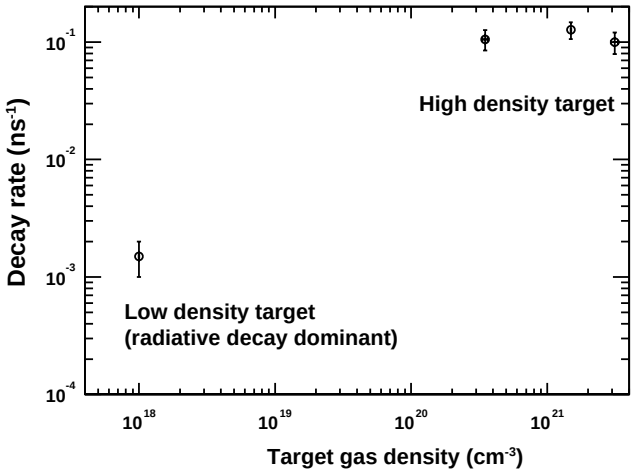

Figure 5.12: Nonlinear density dependence observed for the decay rate of the (32, 31) of $\overline{p}^4$He$^+$state. The decay rate was almost constant in the high-density region.

The anomaly observed for the state (32, 31) is an enhancement of the decay rate of about $10^2 - 10^3$ over $0.1 - 1$ μs^{-1}, which is expected for an $L = 4$ Auger transition. Unlike the other three rates, variational calculations by both Korobov and Kino resulted in non-anomalous lifetimes. Although it has nearby electron-excited states, the decay rate anomaly was not because of the configuration mixing effect. It was proved by a new result obtained one year after the measurement, which is presented in the next section.

5.7.3 Collisional Enhancement of the Decay rate

It was already known at LEAR that collisional effects may change the character of certain $\overline{p}$He$^+$states [33]. In the experiment at AD, decay rates of some states were measured only at the standard condition (states marked as '*' in Table 5.2), and the others were measured at various conditions (more than three density points in 5–6K, 20–200 kPa) but no significant difference was observed for all the states.

However, it was revealed in the low-density experiment that the (32, 31) is not short-lived at the low-density condition anymore, and the radiative rate is supposed to be dominant (Fig. 5.12). Although a configuration mixing effect had been suspected for this state [65], the anomaly of the decay rate was proved to be a density-dependent effect, similar to the lifetime shortening of the state (37, 34) observed at LEAR [33].

There are possibilities that the rate enhancements by collisions more or less exist

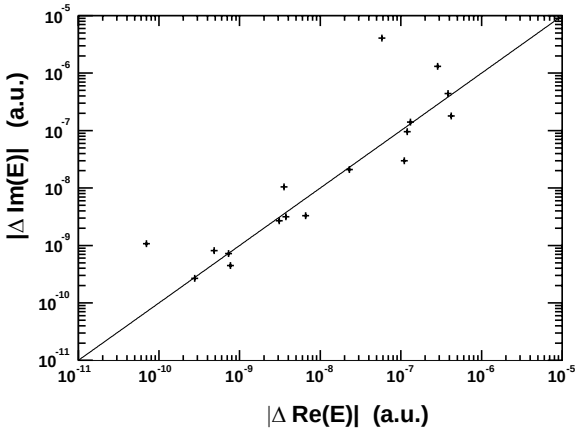

Figure 5.13: Comparison of the two theories in the complex plane (log-arithmetic scale). $|\Gamma_{\mathrm{Korobov}}/2 - \Gamma_{\mathrm{Kino}}/2|$ is plotted against $|E_{r\,\mathrm{Korobov}} - E_{r\,\mathrm{Kino}}|$ for the states calculated by the CCR method. On the line shown in the figure, the real part equals to the imaginary part. The unit is a.u. (10^{-9} a.u. = 41.5 MHz).

for the other states. Especially, the states which have much larger decay rates than theories are suspected, and it is desirable to perform low-density measurements for them.

5.8 Energy Comparison in the Complex Plane and Precise Measurements

The calculations by Korobov and Kino simultaneously yield the real and imaginary part of the complex energy,

$$E = E_r - i\frac{\gamma/2\pi}{2}. \tag{5.4}$$

They claim that the convergence of the imaginary part is as good as the real part.

The equality of the precision of the real and imaginary parts can be verified by comparing the two theories in the complex plane, as presented in Fig. 5.13. In this figure, the difference of the complex energy between the two calculations are plotted. Most of the points are distributed around the (Real part) = (Imaginary part) line. This result supports the view, in which the accuracy is the same order for both part of the complex energy, for a wide range of the magnitude (10^{-9}–10^{-6} a.u.). Two states have differences in the imaginary part 1–2 orders of magnitude larger than in the real part. It might be suggesting that the difference of the basis functions is crucial in their Auger rate calculations for some states.

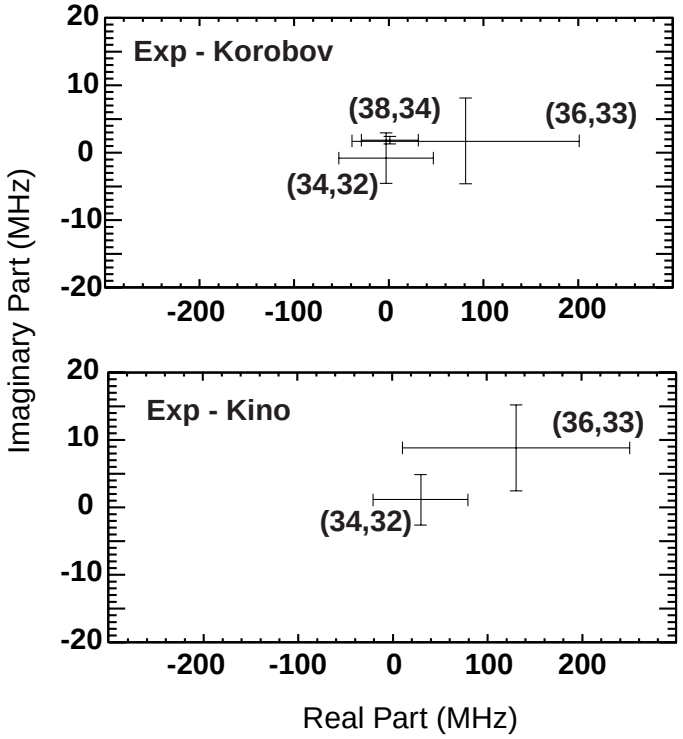

Figure 5.14: Precise comparison of the complex energies of three $\overline{p}^4$He$^+$states [64]. The difference of the experimental values from the two theories [28, 29] are plotted in MHz. The imaginary part plotted here is half Auger width with negative sign, $-\frac{1}{2}(\gamma_A/2\pi)$. The values used for the comparison of the real part are the transition energies from metastable states, where the theoretical uncertainty should be very small.

Therefore, basically we are able to treat the Auger rates in the same way as transition energies, and expand the CPT test to the complex plane. Among the measured Auger rates, three rates have comparable magnitude (100 MHz-order) with the uncertainty of the precisely-measured transition energies. In Fig. 5.14, the complex energy is compared between the experiment and two theories ([28] and [29]). For the imaginary part (half Auger width) of the three $\overline{p}^4$He$^+$states presented in Fig. 5.14, a very precise comparison of 10 MHz-order, which is even more precise than the the real part (transition energy), is achieved.

As discussed above, the decay rate measurements are expected to contribute to the improvement of the CPT limit, but we may need more consideration and measurements in order to have a satisfactory result. We have to use a low density target and check the density dependence carefully, to make sure that the decay rate is not enhanced by collisional effects. A fast-response PMT and a narrow-

linewidth laser are needed to perform direct measurements of the intermediate rates possible. They are also expected to improve the precision of the measurements. More theoretical works are needed as well. The large theoretical discrepancy for the (34, 31) of $\overline{p}^3\mathrm{He}^+$has to be explained in order to know the validity of the calculations, and the antiproton-mass dependence of the decay rates (the f value) must be evaluated. Then the CPT limit would be significantly reduced than to measure only the real part of the energy.

Chapter 6

Conclusion

We have measured the energies and lifetimes of the antiprotonic helium atoms ($\overline{p}^4\mathrm{He}^+$and $\overline{p}^3\mathrm{He}^+$) by performing a laser spectroscopy with a newly developed experimental system at CERN AD.

Energies of thirteen transitions of $\overline{p}\mathrm{He}^+$were measured with the precision of a few 100 ppb with the considerations of the density shift effect. Eleven of them were measured using very slow (100 keV) antiproton beams and a low-density (10^{17} cm^{-3}) gas target, and the other two were measured at various densities, and the results were extrapolated toward the zero-density point. All the transition energies were compared with latest theoretical three-body calculations by Korobov and by Kino. The agreement between the experiment and theories were extremely good, and we were able to put a limit of 10 ppb with a confidence level of 90%, for the proton-antiproton mass and charge differences.

Decay rates of fifteen short-lived states were newly studied. Six rates were measured by their large natural width, three were by the prolongation of the annihilation signals. The other six rates were not directly measured and only constrained to be in limited ranges. Most of them were in agreement with approximations by their transition multipolarities, however, a few exceptions were found. The decay rates of the (37, 33) and (35, 32) of $\overline{p}^4\mathrm{He}^+$, and the (34, 31) of $\overline{p}^3\mathrm{He}^+$are likely to be enhanced by the state mixing with near-lying short-lived states, as was pointed out by Kartavtsev. while the rate of the (32,31) of $\overline{p}^4\mathrm{He}^+$were increased by collisional effect.

By using the results of both energies and rates, we succeeded in testing the theoretical complex energies of the atom with a precision of the order of 10 MHz.

Appendix A

Atomic Units and Density

A.1 Atomic units

The atomic units, which often appear in this thesis, are summarized in the following list. For various dimensions, 1 a.u. are defined as:

- length (Bohr radius): $a_0 = \frac{4\pi\epsilon_0\hbar^2}{m_e e^2} = 5.291772 \times 10^{-11}\text{m}$
- mass (electron mass): $m_e = 9.109390 \times 10^{-31}\text{kg}$
- charge (elementary charge): $e = 1.602176 \times 10^{-19}C$
- angular momentum (Plank constant / 2π): $\hbar = 1.054573 \times 10^{-34}\text{J} \cdot \text{s}$
- energy (Hartree energy): $E_h = \frac{e^2}{4\pi\epsilon_0 a_0} = 4.359748 \times 10^{-18}\text{J}$
- speed: $\frac{e^2}{4\pi\epsilon_0\hbar} = 2.187691 \times 10^6\text{m/s}$
  (therefore, speed of light $c = \frac{1}{\alpha} = 137.0360$ a.u.)
- time: $\frac{4\pi\epsilon_0 a_0\hbar}{e^2} = 2.418884 \times 10^{-17}\text{s}$

The following are also defined as equal to unity in the atomic units:

- Vacuum dielectric constant: $4\pi\epsilon_0 = 4\pi \times 8.854188 \times 10^{-12}F/m$
- Boltzmann constant: $k = 1.380650 \times 10^{-23}J/K$

A.2 Atomic Density

The temperature and pressure of the target helium gas were measured in K and hPa (or Torr), respectively. We had to obtain the atomic density of helium gas N/V (the number of atoms divided by the volume) for the density extrapolation.

For ideal gases, their densities can be calculated by the equation of the state,

$$V/N = \frac{RT}{N_A P}, \tag{A.1}$$

where N_A, P, R and T are the Avogadro number, pressure, gas constant and temperature, respectively. However, a large deviation from the ideal gas approximation is expected for the low temperature and dense helium gas. So we used a computer program HEPAK (by Cryodata, http://www.cryodata.com/hepak.htm), and the gas density ρ in g/l was obtained.

By using the mass of helium atom and the Avogadro number,

$$M_{He} = 4.002 \text{ g/mol}, \tag{A.2}$$

$$N_A = 6.022 \times 10^{23}, \tag{A.3}$$

the atomic density is obtained as:

$$N/V[10^{21}\text{cm}^{-3}] = 10^{-24} N_A/M_{He} \times \rho[\text{g/l}]. \tag{A.4}$$

$$= 0.1505 \times \rho[\text{g/l}]. \tag{A.5}$$

In other words, atomic density of 10^{21} cm^{-3} is equivalent to ρ =6.646 g/l for helium gas.

Appendix B

Semi-classical theory of density shift and broadening

B.1 Collisional Broadening

Generally, atomic spectral line is shifted and broadened by collisions with surrounding atoms and molecules [68, 69]. Since 19th century, collisional effect on atomic spectral lines is studied by many people such as Michelson, Lorentz, and Lentz. The lineshape was known to be a center-shifted Lorentzian by 1940s. The reason could be explained as random shift of the phase of atomic wavefunction caused by elastic collisions.

$$I(\omega) = \frac{\gamma/\pi}{(\omega - \omega_0 - \sigma)^2 + \gamma^2}. \tag{B.1}$$

B.2 General Theory in the Semi-classical Model

B.2.1 Anderson Theory

With the following assumptions, the amount of the shift and the broadening can be calculated [69].

1. The collision interval is much longer than the duration time of a collision.
2. The collisions are elastic and binary (two-body).
3. The perturbers travel on a classical linear trajectory.

We take the interaction potential between an emitter and a perturber as $V(\boldsymbol{R})$
The explicit form of $V(R)$ is supposed to be, for example, van der Waals potential,

$$V_j(R) = -\frac{C}{R^6}. \tag{B.2}$$

The wave function of the atom can be written as:

$$f(t) = \exp\{i\omega_0 t + i\eta(t)\}, \tag{B.3}$$

where $\eta(t)$ is the phase shift caused by the interaction potential V

$$\eta(t) = \hbar^{-1} \int_{-\infty}^{t} V(\boldsymbol{R}(t))dt. \tag{B.4}$$

The autocorrelation function $\Phi(s)$ is defined as follows:

$$\begin{aligned} \Phi(s) &=< f^*(t)f(t+s) >_t \\ &= \lim_{\Delta t\to\infty} \frac{1}{\Delta t} \int_{-\Delta t/2}^{+\Delta t/2} f^*(t)f(t+s)dt \\ &\propto \exp(-i\omega_0 s) < \exp\{-i[\eta(t+s) - \eta(t)]\} >_t . \end{aligned} \tag{B.5}$$

Here t is the initial time and $<>_t$ means the average over initial time. If we take the central frequency as $\omega_0 = 0$, the autocorrelation function can be redefined as the following.

$$\Phi(s) =< \exp\{-i[\eta(t+s) - \eta(t)]\} >_t . \tag{B.6}$$

The Fourier transformation of $\Phi(s)$ corresponds to the resonance profile $I(\omega)$. This is called Wiener-Khintchine theorem. Therefore,

$$I(\omega) = \frac{1}{\pi} Re\{\int_0^{\infty} \Phi(s) \exp(-i\omega s)ds\}. \tag{B.7}$$

Here we decompose the interaction potential $V(t)$ into binary interaction potential $V_k[R_k(t)]$. If there are N perturbers, V(t) can be rewritten as:

$$V(t) = \sum_{k=1}^{N} V_k[R_k(t)]. \tag{B.8}$$

From Eq. (B.6) and Eq. (B.8),

$$\Phi(s) =< \exp\{-i[\sum_{k=1}^{N} \int_t^{t+s} \hbar^{-1} V_k[R_k(t')]dt']\} >_t . \tag{B.9}$$

If the ergodic hypothesis is valid here, the average over initial time is equivalent to the average over all collision geometries.

$$\Phi(s) =< \prod_{k=1}^{N} \exp\{-i \int_0^s \hbar^{-1} V_k[R_k(t')]dt'\} >_{collisions} . \tag{B.10}$$

Anderson assumed that the perturbers are independent of one another. Then, the mean and the product can be exchanged.

$$\Phi(s) = [< \exp\{-i \int_0^s \hbar^{-1} V[R(t')]dt'\} >_{collisions}]^N. \tag{B.11}$$

To calculate the mean, here we take the rectilinear trajectory Fig. B.1. b is the

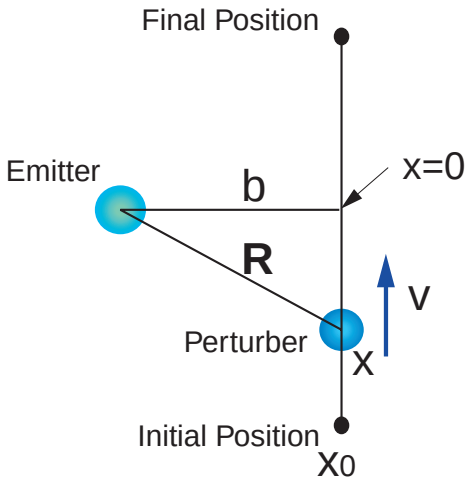

Figure B.1: Rectilinear trajectory

impact parameter, $x = x_0 + \bar{v}t'$ is the coordinate of the perturber. We integrate this function over all possible initial position in volume $\mathcal{V}$.

$$\begin{aligned} \Phi(s) &= [\frac{1}{\mathcal{V}} \int\int_{\mathcal{V}} 2\pi b\, db\, dx_0 \exp\{-i \int_0^s \hbar^{-1} V[(b^2 + x^2)^{1/2}]\}dt']^N \\ &= [1 - \frac{1}{\mathcal{V}} \int\int_{\mathcal{V}} 2\pi b\, db\, dx_0 [1 - \exp\{-i \int_0^s \hbar^{-1} V[(b^2 + x^2)^{1/2}]\}dt']]^N. \end{aligned} \tag{B.12}$$

We use approximation $(1-\alpha)^N \simeq \exp(-N\alpha)$, (for $\alpha \ll 1$ and $N \gg 1$) and define density as $n = N/\mathcal{V}$. If $\mathcal{V}$ is large enough,

$$\Phi(s) = \exp[-ng(s)] \tag{B.13}$$

$$g(s) = 2\pi \int_0^\infty b\,db \int_{-\infty}^\infty dx_0[1 - \exp(-i \int_0^s \hbar^{-1} V[(b^2 + x^2)^{1/2}]dt')]. \tag{B.14}$$

When $\bar{v}$ is small enough, $g(s)$ can be expanded as a linear function.

$$g(s) = (\alpha_0 + i\beta_0) + (\alpha_1 + i\beta_1)s. \tag{B.15}$$

Here α_0, β_0 are parameters which make asymmetry. Usually, they are very small and taken as zero. In this case, Fourier transformation of Eq. (B.13) becomes Lorentzian which have the width of $2n\alpha_1$ and the shift of $n\beta_1$. In this semi-classical model, the shift and the broadening are both proportional to the density and the magnitude can be calculated by the following integral.

$$\alpha_1 = 2\pi\bar{v} \int_0^\infty b\,db[1 - \cos(\int_{-\infty}^{+\infty} (\hbar\bar{v})^{-1} V[(b^2 + x^2)^{1/2}]dx)]. \tag{B.16}$$

$$\beta_1 = 2\pi\bar{v} \int_0^\infty b\,db \sin(\int_{-\infty}^{+\infty} (\hbar\bar{v})^{-1} V[(b^2 + x^2)^{1/2}]dx). \tag{B.17}$$

B.3 Calculation by Bakalov

Bakalov evaluated density shift and broadening effect for many transitions of the antiprotonic helium atom. Basically his calculation is based on the standard semi-classical model. The biggest difference is that he calculated interatomic potential $V(R, r, \theta)$ numerically and took nonlinear classical trajectory. His coordinate system and an example of potential curve $V(R, r = 0.65, \theta)$ are shown in Fig. B.2. $r = 0.65$ a.u. is the mean radius of 1s-electron in antiprotonic helium atoms. It is displaying whether interatomic potential near the antiprotonic helium atom is attractive or repulsive depends on θ.

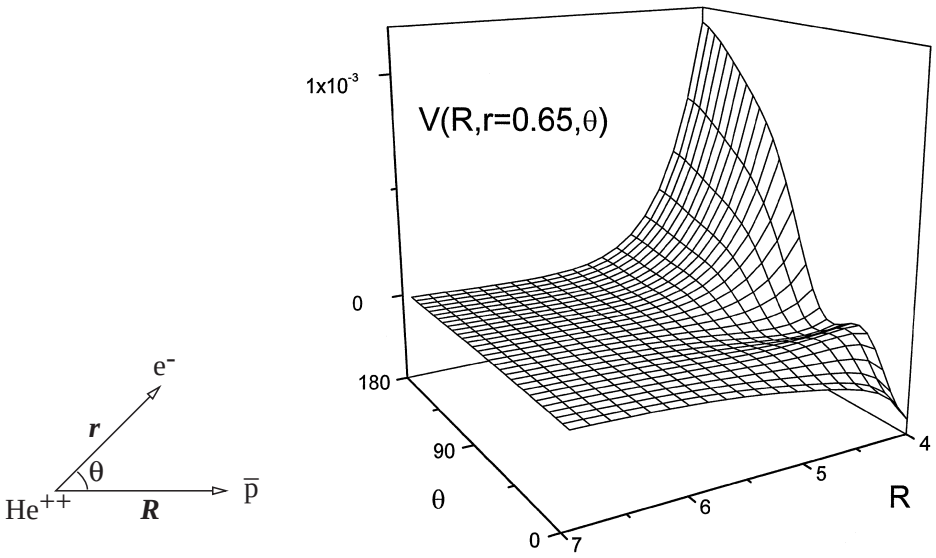

Figure B.2: Coordinate system of Korobov-Bakalov calculation [31] (left), and $\bar{p}\mathrm{He}^{+}$-He interaction energy surface $V(R, r, \theta)$ for r=0.65 a.u. (right). All quantities are in a.u.

Appendix C

Spectral Width of Resonances

Atomic spectral lines which we observe are broadened due to many reasons. Here I describe various sources of broadening, each of which broadens the line in the shape of a Gaussian or Lorentzian. The general lineshape including all of the broadening effects is discussed at last.

C.1 Laser Linewidth

Since we scanned the atomic lines with lasers having finite linewidths, the resulting resonance profile convoluted the lineshape of the laser.

The single longitudinal mode of our dye laser, defined by a 30 cm-long cavity, has a Lorentzian-like shape. The produced pulses has a collections of longitudinal modes, so the lineshape deforms to a Gaussian-like shape. For the broadband-mode lasers, the lineshape is almost an exact Gaussian.

As described in Sec.5.3.1, Our laser system have linewidth δ_l of 0.6–1 GHz with an intracavity etalon, and 4–10 GHz for the broadband mode. The laser linewidth was the first or second largest component of the total width in the spectroscopy.

C.2 Doppler Width

Thermal motion of the atom also can be an origin of the broadening of the spectral linewidth. Here we assume the velocity of the atom $\boldsymbol{v}$ follows the Maxwell-Boltzmann distribution.

$$f(\boldsymbol{v})d\boldsymbol{v} = (\frac{M}{2\pi kT})^{\frac{3}{2}} \exp(-\frac{M\boldsymbol{v}^2}{2kT})d\boldsymbol{v}. \tag{C.1}$$

where M is the mass of the atom and T is the temperature. The shape of the broadening is a Gaussian having a FWHM of

$$\delta_d = 2\sqrt{2\log 2} \times \nu \frac{\bar{v}}{c} = 2.35 \times \nu \sqrt{\frac{kT}{Mc^2}}, \tag{C.2}$$

where $\bar{v}$ is the average velocity of the atoms. For the wavelengths used in our experiment (264–726 nm) and the temperature ($\sim$ 6K), the Doppler widths (FWHM) become 0.3–0.9 GHz.

C.3 Natural Width

According to the principle of uncertainty, a level with the lifetime of τ (inverse of the decay rate γ) is observed as the Lorentzian with FWHM of

$$2\Gamma_{\rm nat} = \frac{\gamma}{2\pi} = \frac{1}{2\pi\tau}. \tag{C.3}$$

In our spectroscopy, the natural width has a drastic dependence on the lowest Auger transition multipolarity L, as approximated by Eq. (1.1). Typically, the natural width is 10 MHz for the states with the lowest Auger transition multipolarity $L = 3$, and 10 GHz or more for $L = 2$ states.

C.4 Power Broadening

When the electric field applied to the atom is low enough to fulfill the following condition, the transition probability is proportional to the electric field:

$$\Omega \ll t^{-1}, \tag{C.4}$$

where t is the duration time of the electric field, and Ω Rabi frequency . For one-photon dipole transitions,

$$\Omega = \frac{\mu E_0}{\hbar}, \tag{C.5}$$

where μ is the transition dipole moment, and E_0 the electric field.

However, the linearity breaks when above condition is not true. In such a case, the transition probability around the center of the resonance is saturated while the other part is not saturated. Therefore, the resonance profile is effectively broadened. This type of broadening is called power broadening.

The FWHM (2Γ) changes

$$2\Gamma \to 2(\Gamma^2 + \frac{1}{2}\Omega^2)^{1/2}. \tag{C.6}$$

Therefore, the additional width is

$$\Delta(2\Gamma) = \sqrt{2}\Omega^2 (\Omega \gg \Gamma) \tag{C.7}$$

$$= \frac{1}{2}\frac{\Omega^2}{\Gamma} (\Omega \ll \Gamma). \tag{C.8}$$

$$\tag{C.9}$$

In our experiment, the Rabi frequency can be up to several GHz for the favored transitions. So the power broadening is possible for favored and narrow (natural width is much smaller than 1 GHz) transitions, but we can hardly see the broadening for unfavored and wide transitions.

C.5 Collisional Broadening

As described in Section B, resonance linewidth is broadened by collisions with surrounding atoms. This gives Lorentzian width of Γ_c. According to the experimental result at LEAR [27] and Bakalov [31], Γ_c is expected to be less than 0.5 GHz for our cases.

C.6 General Lineshape

As a result, lineshape of the resonance should be a convolution of Gaussian and Lorentzian,

$$V(\omega) = \frac{\Gamma}{2^{1/2}\pi^{3/2}\delta} \int_{-\infty}^{\infty} \frac{\exp\{-(\omega-\nu)^2/2\delta^2\}}{(\omega_0-\nu)^2 + \Gamma^2} d\nu, \tag{C.10}$$

which is called Voigt function. Here ω_0 is the center of the resonance, and δ and Γ are Gaussian width (root-mean square width) and Lorentzian HWHM, respectively. δ can be written using δ_l and δ_d described above.

$$\delta^2 = \delta_l^2 + \delta_d^2. \tag{C.11}$$

Γ has more complex relationship because power broadening depends on the other effects. The general formula of the Lorenzian width including collisional broadening, power broadening and natural width is the following.

$$\Gamma = 2\{(\Gamma_n + \Gamma_c)^2 + \frac{1}{\sqrt{2}}(1 + \frac{\Gamma_c}{\Gamma_n})\Omega^2\}^{\frac{1}{2}}. \tag{C.12}$$

Bibliography

[1] E. Fermi and E. Teller, Phys. Rev. **72**, 399 (1947).

[2] A. S. Wightman, Phys. Rev. **77**, 521 (1950).

[3] G. T. Condo, Phys. Lett. **9**, 65 (1964).

[4] J. E. Russell, Phys. Rev. A **1**, 742 (1970).

[5] J. E. Russell, Phys. Rev. Lett. **23**, 63 (1969).

[6] R. S. Hayano, T. Ishikawa, M. Iwasaki, H. Outa, E. Takada, and H. Tamura, Phys. Lett. B **231**, 355 (1989).

[7] T. Yamazaki, M. Aoki, M. Iwasaki, R. S. Hayano, T. Ishikawa, H. Outa, E. Takada, H. Tamura, and A. Sakaguchi, Phys. Rev. Lett. **63**, 1590 (1989).

[8] S. N. Nakamura, M. Iwasaki, H. Outa, R. S. Hayano, Y. Watanabe, T. Nagae, T. Yamazaki, H. Tada, T. Numao, Y. Kuno, and R. Kadono, Phys. Rev. A **45**, 6202 (1992).

[9] M. Iwasaki, S. N. Nakamura, K. Shigaki, Y. Shimizu, H. Tamura, T. Ishikawa, R. S. Hayano, E. Takada, E. Widmann, H. Outa, M. Aoki, P. Kitching, and T. Yamazaki, Phys. Rev. Lett. **67**, 1246 (1991).

[10] T. Yamazaki, E. Widmann, R. S. Hayano, M. Iwasaki, S. N. Nakamura, K. Shigaki, F. J. Hartmann, H. Daniel, T. von Egidy, P. Hofmann, Y.-S. Kim, and J. Eades, Nature **361**, 238 (1993).

[11] N. Morita, K. Ohtsuki, and T. Yamazaki, Nucl. Instrum. Methods Phys. Res., Sect. A **330**, 439 (1993).

[12] R. S. Hayano, F. E. Maas, H. A. Torii, N. Morita, M. Kumakura, T. Yamazaki, H. Masuda, I. Sugai, F. J. Hartmann, H. Daniel, T. von Egidy, B. Ketzer,

W. Müller, W. Schmid, D. Horváth, J. Eades, and E. Widmann, Phys. Rev. Lett. **73**, 1485 (1994), errata **73**, 3181 (1994).

[13] F. E. Maas, R. S. Hayano, T. Ishikawa, H. Tamura, H. A. Torii, N. Morita, T. Yamazaki, I. Sugai, K. Nakayoshi, F. J. Hartmann, H. Daniel, T. von Egidy, B. Ketzer, A. Niestroj, S. Schmid, W. Schmid, D. Horváth, J. Eades, and E. Widmann, Phys. Rev. A **52**, 4266 (1995).

[14] H. A. Torii, M. Hori, T. Ishikawa, F. E. Maas, R. S. Hayano, N. Morita, M. Kumakura, I. Sugai, B. Ketzer, H. Daniel, F. J. Hartmann, R. Pohl, R. Schmidt, T. von Egidy, D. Horvath, J. Eades, E. Widmann, and T. Yamazaki, Phys. Rev. A **53**, R1931 (1996).

[15] T. Yamazaki, E. Widmann, J. Eades, M. Kumakura, N. Morita, H. A. Torii, M. Hori, T. Ishikawa, F. E. Maas, H. Tamura, R. S. Hayano, I. Sugai, Y. Fujita, B. Ketzer, H. Daniel, F. J. Hartmann, M. Hasinoff, R. Pohl, R. Schmidt, T. von Egidy, and D. Horváth, Phys. Rev. A **55**, R3295 (1997).

[16] B. Ketzer, F. J. Hartmann, T. von Egidy, C. Maierl, R. Pohl, J. Eades, E. Widmann, T. Yamazaki, M. Kumakura, N. Morita, R. S. Hayano, M. Hori, T. Ishikawa, H. A. Torii, I. Sugai, and D. Horváth, Phys. Rev. Lett. **78**, 1671 (1997).

[17] R. Pohl, F. J. Hartmann, B. Ketzer, T. von Egidy, C. Maierl, J. Eades, E. Widmann, T. Yamazaki, M. Kumakura, N. Morita, R. S. Hayano, M. Hori, T. Ishikawa, H. A. Torii, I. Sugai, and D. Horváth, Phys. Rev. A **58**, 4406 (1998).

[18] E. Widmann, J. Eades, T. Yamazaki, H. A. Torii, R. S. Hayano, M. Hori, T. Ishikawa, M. Kumakura, N. Morita, I. Sugai, F. Hartmann, T. von Egidy, B. Ketzer, C. Maierl, R. Pohl, and D. Horváth, Phys. Lett. B **404**, 15 (1997).

[19] E. Widmann, J. Eades, T. Ishikawa, J. Sakaguchi, T. Tasaki, H. Yamaguchi, R. S. Hayano, M. Hori, H. A. Torii, B. Juhász, D. Horváth, and T. Yamazaki, Phys. Rev. Lett. **89**, 243402 (2002).

[20] A. Adamo *et. al.*, Nucl. Phys. A **569**, 761 (1994).

[21] T. Yamazaki and K. Ohtsuki, Phys. Rev. A **45**, 7782 (1992), k. Ohtsuki, unpublished theoretical data (1992).

[22] I. Shimamura, Phys. Rev. A **46**, 3776 (1992).

[23] V. I. Korobov, Phys. Rev. A **54**, R1749 (1996).

[24] Y. Kino, M. Kamimura, and H. Kudo, Nucl. Phys. A **631**, 649c (1998).

[25] E. Yarevsky and N. Elander, Europhys. Lett **37**, 453 (1997).

[26] N. Elander and E. Yarevsky, Phys. Rev. A **56**, 1855 (1997), errata **57**, 2256 (1998).

[27] H. A. Torii, Ph.D. thesis, University of Tokyo (1997).

[28] V. I. Korobov, Phys. Rev. A **67**, 062501 (2003), errata **68**, 019902 (2003).

[29] Y. Kino, M. Kamimura, and H. Kudo, Nucl. Instrum. Methods Phys. Res., Sect. B (????), in press.

[30] G. Ya. Korenman, INP MSU Preprint 97-I/452, M. V. Lomonosov Moscow State University, D. V. Skobeltzyn Institute of Nuclear Physics, Moscow (1997).

[31] D. Bakalov, B. Jeziorski, T. Korona, K. Szalewicz, and E. Tchoukova, Phys. Rev. Lett. **84**, 2350 (2000).

[32] H. A. Torii, R. S. Hayano, M. Hori, T. Ishikawa, N. Morita, M. Kumakura, I. Sugai, T. Yamazaki, B. Ketzer, F. J. Hartmann, T. von Egidy, R. Pohl, C. Maierl, D. Horváth, J. Eades, and E. Widmann, Phys. Rev. A **59**, 223 (1999).

[33] M. Hori, H. A. Torii, R. S. Hayano, T. Ishikawa, F. E. Maas, H. Tamura, B. Ketzer, F. J. Hartmann, R. Pohl, C. Maierl, M. Hasinoff, T. von Egidy, M. Kumakura, N. Morita, I. Sugai, D. Horváth, E. Widmann, J. Eades, and T. Yamazaki, Phys. Rev. A **57**, 1698 (1998), errata **58**, 1612 (1998).

[34] T. Yamazaki, B. Ketzer, E. Widmann, J. Eades, H. Daniel, F. J. Hartmann, M. Hasinoff, R. Pohl, R. Schmidt, T. von Egidy, D. Horváth, M. Kumakura, N. Morita, I. Sugai, Y. Fujita, H. A. Torii, M. Hori, T. Ishikawa, F. E. Maas, H. Tamura, and R. S. Hayano, Chem. Phys. Lett. **265**, 137 (1997).

[35] V. I. Korobov, D. Bakalov, and H. J. Monkhorst, Phys. Rev. A **59**, R919 (1999).

[36] M. Kamimura, Phys. Rev. A **38**, 621 (1988).

[37] Y. Kino, N. Yamanaka, M. Kamimura, P. Froelich, and H. Kudo, Hyperfine Intractions **138**, 179 (2001).

[38] H. A. Bethe, Phys. Rev. **72**, 339 (1947).

[39] N. Moiseyev, Phys. Rep. **302**, 211 (1998).

[40] Y. Ho, Phys. Rep. **99**, 1 (1983).

[41] A. Niestroj, F. J. Hartmann, H. Daniel, B. Ketzer, T. von Egidy, F. E. Maas, R. S. Hayano, T. Ishikawa, H. Tamura, H. A. Torii, N. Morita, T. Yamazaki, I. Sugai, K. Nakayoshi, D. Horváth, J. Eades, and E. Widmann, Nucl. Instrum. Methods Phys. Res., Sect. A **373**, 411 (1996).

[42] P. Belochitskii, T. Eriksson, A. Findlay, B. Holzer, R. Maccaferri, S. Maury, S. Pasinelli, F. Pedersen, and G. Tranquille, in *TWO YEARS OF AD OPERATION: EXPERIENCE AND PROGRESS* (Proceedings of EPAC 2002, Paris, France, 2002).

[43] A. M. Lombardi, W. Pirkl, and Y. Bylinsky, in *Proceedings of the 2001 Particle Accelerator Conference, Chicago* (IEEE, Piscataway, NJ, 2001), pp. 585–587.

[44] Y. Bylinsky, A. Lombardi, and W. Pirkl, in *RFQD - A DECELERATING RADIO FREQUENCY QUADRUPOLE FOR THE CERN ANTIPROTON FACILITY* (Proceedings of XX International Linac Conference, Monterey, California, U.S., 2002).

[45] M. Hori, J. Eades, R. S. Hayano, T. Ishikawa, W. Pirkl, E. Widmann, H. Yamaguchi, H. A. Torii, B. Juhász, D. Horváth, and T. Yamazaki, Phys. Rev. Lett. **91**, 123401 (2003).

[46] E. Widmann, H. Daniel, J. Eades, T. von Egidy, F. J. Hartmann, R. S. Hayano, W. Higemoto, J. Hoffmann, T. M. Ito, Y. Ito, M. Iwasaki, A. Kawachi, N. Morita, S. N. Nakamura, N. Nishida, W. Schmid, I. Sugai, H. Tamura, and T. Yamazaki, Nucl. Phys. A **558**, 697c (1993).

[47] B. Ketzer, F. J. Hartmann, T. von Egidy, C. Maierl, R. Pohl, J. Eades, E. Widmann, T. Yamazaki, M. Kumakura, N. Morita, R. S. Hayano, M. Hori, T. Ishikawa, H. A. Torii, I. Sugai, and D. Horváth, J. Chem. Phys. **109**, 424 (1998).

[48] B. Juhász, J. Eades, R. S. Hayano, M. Hori, D. Horváth, T. Ishikawa, J. Sakaguchi, H. A. Torii, E. Widmann, H. Yamaguchi, and T. Yamazaki, Eur. Phys. J. D **18**, 261 (2002).

[49] H. A. Torii, R. S. Hayano, F. E. Maas, N. Morita, M. Kumakura, T. Yamazaki, H. Masuda, I. Sugai, B. Ketzer, F. J. Hartmann, H. Daniel, T. von Egidy, W. Müller, W. Schmid, D. Horváth, J. Eades, and E. Widmann, Nucl. Instrum. Methods Phys. Res., Sect. A **396**, 257 (1997).

[50] M. Hori, K. Yamashita, R. S. Hayano, and T. Yamazaki, Nucl. Instrum. Methods Phys. Res., Sect. A **496**, 102 (2002).

[51] M. Hori, R. S. Hayano, E. Widmann, and H. Torii, Opt. Lett. **28**, 2479 (2003).

[52] R. Loudon, *The quantum theory of light* (Oxford University Press, Oxford, 1995), 2nd ed.

[53] B. Bodermann, H. Knökel, and E. Tiemann, Europ. Phys. J. D **19**, 31 (2002).

[54] J. Cariou and P. Luc, *Atras du spectre d'absorption de la molecule de tellure* (Presses CNRS, Paris, 1980).

[55] E. Chang, W. Schoenfeld, E. Bie'mont, P. Quinet, and P. Palmeri, Phys. Scr. **49**, 26 (1994).

[56] W. Whaling *et al.*, J. Res. Natl. Inst. Stand.Technol. **107**, 149 (2002).

[57] D. Bakalov and V. I. Korobov, Phys. Rev. A **57**, 1662 (1998).

[58] Y. Kino, *private communication* (2002).

[59] G. Gabrielse, A. Khabbaz, D. S. Hall, C. Heimann, H. Kalinowsky, and W. Jhe, Phys. Rev. Lett. **82**, 3198 (1999).

[60] M. Hori, J. Eades, E. Widmann, H. Yamaguchi, J. Sakaguchi, T. Ishikawa, R. S. Hayano, H. A. Torii, B. Juhász, D. Horváth, and T. Yamazaki, Phys. Rev. Lett. **87**, 093401 (2001).

[61] K. Hagiwara *et al.*, Phys. Rev. D **66**, 010001 (2002).

[62] M. Hori, J. Eades, R. S. Hayano, T. Ishikawa, T. T. J. Sakaguchi, E. Widmann, H. Yamaguchi, H. A. Torii, B. Juhász, D. Horváth, and T. Yamazaki, Phys. Rev. Lett. **89**, 093401 (2002).

[63] H. Yamaguchi, T. Ishikawa, J. Sakaguchi, E. Widmann, J. Eades, R. S. Hayano, M. Hori, H. A. Torii, B. Juhász, D. Horváth, and T. Yamazaki, Phys. Rev. A **66**, 022504 (2002).

[64] H. Yamaguchi, R. S. Hayano, T. Ishikawa, J. Sakaguchi, E. Widmann, J. Eades, M. Hori, H. A. Torii, B. Juhász, D. Horváth, and T. Yamazaki, Phys. Rev. A (2004), to be submitted.

[65] O. Kartavtsev, D. Monakhov, and S. Fedotov, Phys. Rev. A **61**, 062507 (2000), errata **63**, 019901(E) (2000).

[66] V. I. Korobov and I. Shimamura, Phys. Rev. A **56**, 4587 (1997).

[67] O. I. Kartavtsev and S. I. Fedotov, in *Proceedings of μCF01 Conference, Shimoda* (2001).

[68] N. Allard and J. Kielkopf, Rev. Mod. Phys. **54**, 1103 (1982).

[69] P. W. Anderson, Phys. Rev. **86**, 809 (1952).